SCHOOL OF CHEMICAL ENGINEERING

NATIONAL TECHNICAL UNIVERSITY OF ATHENS

PhD Thesis Dissertation

CONTACT EDGE ROUGHNESS IN EUV LITHOGRAPHY: METROLOGY AND PROCESS EVALUATION

Vijayakumar Murugesan Kuppuswamy

MPhil. Scientific Instrumentation, MSc Electronics Science, BSc Physics

Marie Curie Early Stage Fellow at NCSR Demokritos

Athens, 2012

Thesis Research Supervisor at NCSR Demokritos:
Dr. E. Gogolides, Dr V. Constantoudis

Thesis Supervisor at NTUA: Prof. A. Boudouvis

Members of the Committee in-charge:

Dr. E. Gogolides, NCSR Demokritos

Prof. A. G. Boudouvis, NTUA

Prof. Th. Theodorou, NTUA

Examination Committee

Dr. P. Argitis, NCSR Demokritos

Prof. A. Boudouvis, NTUA

Prof. C. Charitidis, NTUA

Dr. E. Gogolides, NCSR Demokritos

Dr. I. Raptis, NCSR Demokritos

Prof. Th. Theodorou, NTUA

Prof. D. Tsoukalas, NTUA

This work was conducted at NCSR Demokritos, Institute of Microelectronics

This work has been funded by the European Initial Training Network “SPAM: A Supra-disciplinary approach to research and training in surface Physics for Advanced Manufacturing”.

ACKNOWLEDGEMENTS

First and foremost, I would like to thank Dr. E. Gogolides for giving me this opportunity. I would also like to thank my Co-supervisor Dr. V. Constantoudis, for his help, support, patience, enthusiasm, and immense knowledge. His guidance helped me all the time of research and writing of this thesis. Without working under his supervision, I would not have been able to conduct this research and successfully complete my thesis.

Besides my advisor, I would like to thank rest of the thesis advisors. Especially I would like to express my sincere gratitude to my advisor in National Technical University of Athens, Prof. A.G. Boudouvis for his great helpfulness in getting everything achieved in the University.

Besides this, I would like to thank all the colleagues and students from Demokritos. Especially, I would like to thank future doctorate Pavlos to whom I have discussed many things about my research and programming. I have to be really lucky to have such an intelligent guy as a friend.

I would also like to thank people in IMEC, Belgium. A.Vaglio Pret and R. Groheid. They provided support for our research by providing the SEM images.

Especially A. Vaglio Pret was very helpful during his discussion with me. I also like to thank Greg Gallatin for useful discussion that we had during this project.

The work on this thesis was supported by the European Initial Training Network “SPAM: A Supra-disciplinary approach to research and training in surface Physics for Advanced Manufacturing”. My dearest thanks to consortium people especially consortium coordinator A. Gerold for his excellent coordination of this project.

I have no words to express my gratitude to my wife, Deepa, for everything she has done for me during last six month of my PhD. I would also like to thank my friend Krithika for her help to correct my thesis along with my wife Deepa. I would also like to thank my brother Jagan for helping me out in sketching few diagrams.

I like to thank all my family members, who all encouraged me. Finally yet importantly, of course it is my mom Sulochana to whom I would like to express my thanks, who has done lot of sacrifices and enabled me to achieve this education right from my childhood. Moreover, I am sure that she would be happy to see me for reaching at these heights. I can dedicate my doctorate only to her.

SHORT ABSTRACT

The increased stochastic effects in the nanofabrication processes result in patterned features with deviations from the designed shape and size uniformity. In the top-down approach to nanotechnology (lithographic techniques), the process stochasticity is manifested in the roughness of the feature surfaces and the variability of their size. The roughness and variability issues become more evident in Extreme Ultra Violet Lithography, the strongest candidate for circuit manufacturing at critical dimensions <20nm. The fabrication of nanofeatures with controlled sidewall roughness and variability using EUVL requires the development of advanced metrological and modelling tools since the capabilities of the present methods are limited.

In this thesis, we developed metrology and modelling methodologies specialized in the measurement of the roughness and variability of contact holes and the simulation of their fabrication. The metrology approach is based on the analysis of top-down SEM images, while a simple modelling framework is used capable to include the effects of photon shot noise (PSN) acid diffusion and pattern parameters (CD and pitch). Then we applied these tools in the analysis and interpretation of experimental results concerning the effects of exposure dose and resist ingredients (PAG, sensitizer, quencher) on contact sidewall

roughness (Contact Edge Roughness, CER) and size variability (Critical Dimension Uniformity, CDU). We found that the dependencies of CDU on dose, sensitizer and quencher are dominated by photon shot noise (PSN) effects whereas a transition from PAG statistics dominated to PSN driven behavior is observed in the dependence of CDU on PAG concentration.

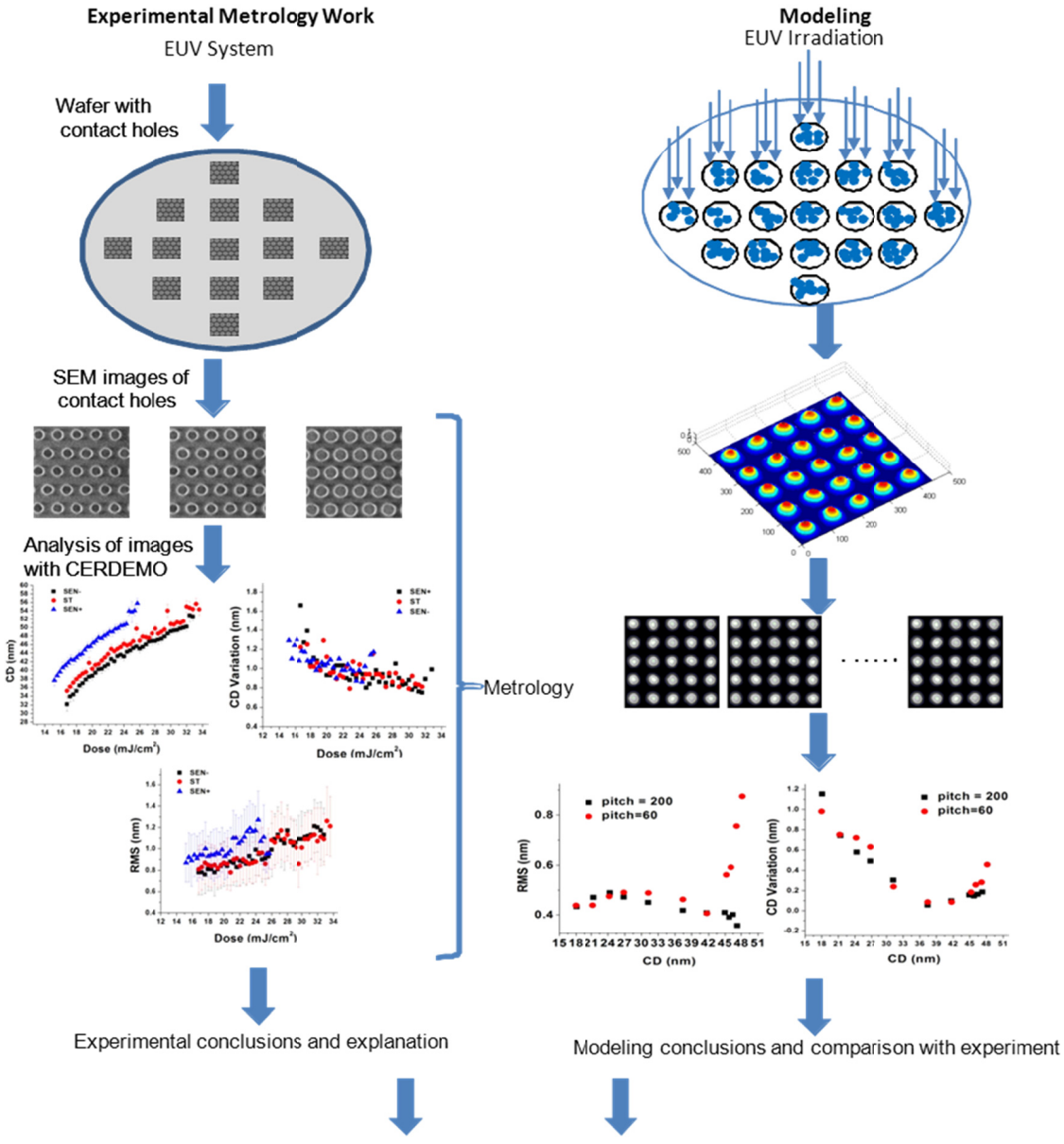

Figure 1 Summary of the aim and structure of the thesis.

The estimated CER parameters (root mean square (RMS) value and correlation length (ξ) exhibit a merging trend when are plotted against the final critical dimension (CD). In addition, RMS value increases with exposure dose and PAG loading contrary to shot noise and Line Edge Roughness expectations. Power spectrum analysis reveals the dominant contribution of low-frequency undulations to CER, which is attributed to the enhanced interaction along specific directions between the aerial image and / or acid kinetics of nearby contacts. This inter-contact effect is further intensified with CD for fixed pitch and may explain the observed CER behavior.

In summary, the results of this thesis show that in EUV lithography, besides PSN effects the roughness and variability of the printed features may also be affected by the chemical noise of PAG molecules and the pattern parameters CD and pitch.

EXTENDED ABSTRACT

In coming years, Extreme Ultra Violet Lithography (EUVL) is expected to play a vital role in the fabrication of integrated circuit features at <20nm scale. One of the main challenges for developing EUVL is to find the right photosensitive polymer materials (resists) and process conditions, which satisfy sidewall roughness and dimensional variability in fabricated features to allowable limit. The sidewall roughness is critical since it induces local deviations from designed dimension and consequently leads to degradation of device performance. Non-uniformity in feature size and dimensions leads to variability in device performance and increased yield losses. Up to date, the majority of works have been devoted to the sidewall roughness of resist lines, the so-called line edge (or width) roughness (LER/LWR) issue. However, recently, the variability of contact sizes on a wafer (most times called Critical Dimension Uniformity, CDU) as well as the sidewall roughness of contact holes (Contact Edge Roughness, CER) have been recognized as two main challenges in EUVL and have been the subject of many research projects and works in both industry and academia. To this end, the development of metrological and characterization methods of CER and CDU as well as the evaluation of the process and material factors contributing to their formation are needed.

The main aim of this thesis is a) to provide methodologies for measuring and characterizing CER and contact CD variability by means of CD-Scanning Electron Microscope (CD-SEM) images, b) to apply these methodologies in order to study various process and material effects, such as exposure dose, PhotoAcid Generator (PAG), sensitizer and quencher concentration in resist on CER and CD variability and c) to develop a numerical modeling of CER formation to provide better understanding of the experimental results and of the origins of the observed trends.

Firstly, we have proposed an improved methodology and developed the related code (CERDEMO) for the measurement and full characterization (including frequency and spatial aspects) of CER and CD variability. Schematic flow of this methodology is shown in Figure 2. CER characterization is carried out using appropriate parameters such as rms, correlation length and roughness exponent (fractal dimension). The frequency content of CER is evaluated by using a properly defined power spectrum while the spatial and scaling aspects are examined through the height-height correlation function (HHCF) of edge fluctuations. The methodology has been applied to study the effect of measurement process parameters, such as magnification of SEM image and noise smoothing filter parameter on CER and CDU. It was found that high magnification increases both RMS of CER and CDU, whereas reduces the measured correlation length. The noise-smoothing filter gradually decreases RMS and CDU but increases ξ. Finally, we compared the inside image CDU (local CDU) with the CD variability among images (global CDU) and we found that the most significant contribution to CDU is the local CDU.

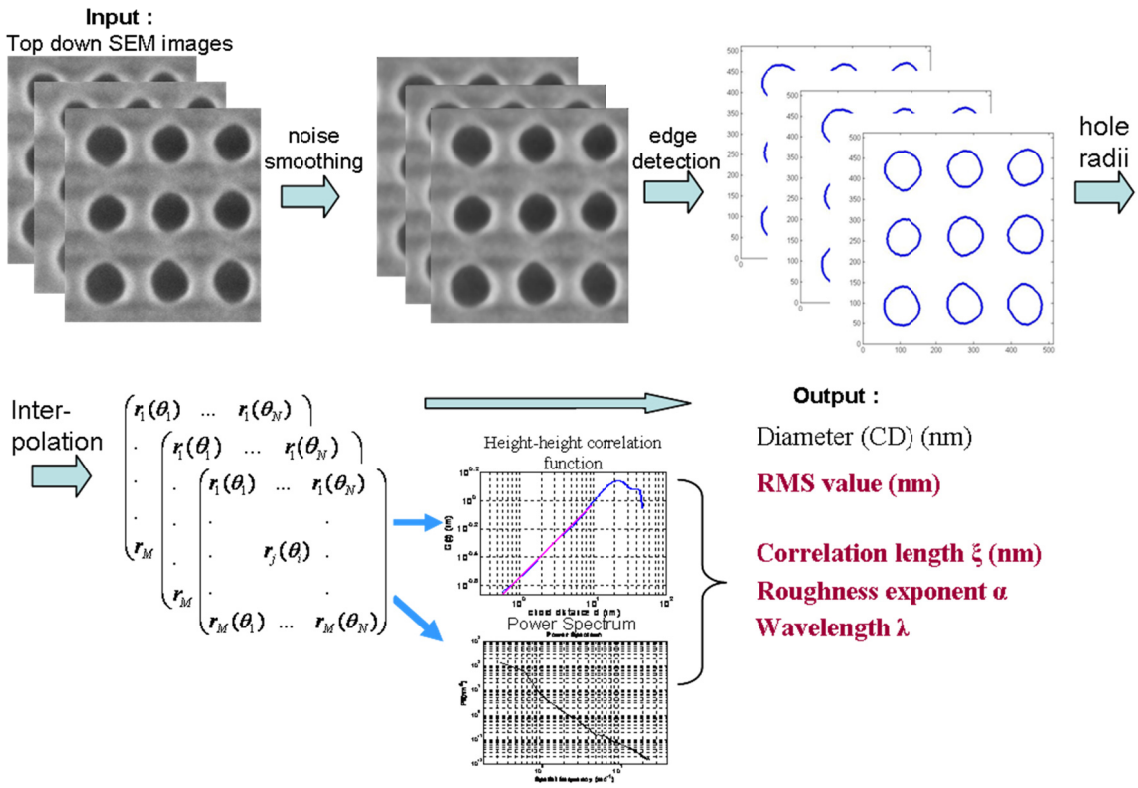

Figure 2 Schematic flow diagram of CER evaluation methodology

Also, we studied the relationship between CER and LER. The frequency and scaling analysis of CER with the developed methodology revealed the dominant role of low frequency undulations with respect to LER. In addition, the different 2D circular topology of contacts induces two new effects with potential impact on CER and CDU: a) variations of CD cause changes in the contact edge-length included in the measurement of CER/CDU and therefore may affect their values according to roughness theory (*contact edge-length effect*) (see Figure 3), b) in dense contact patterns, increase of CD for fixed pitch brings contact edges closer enhancing contact proximity and interaction (*contact proximity effect*) (see Figure 3).

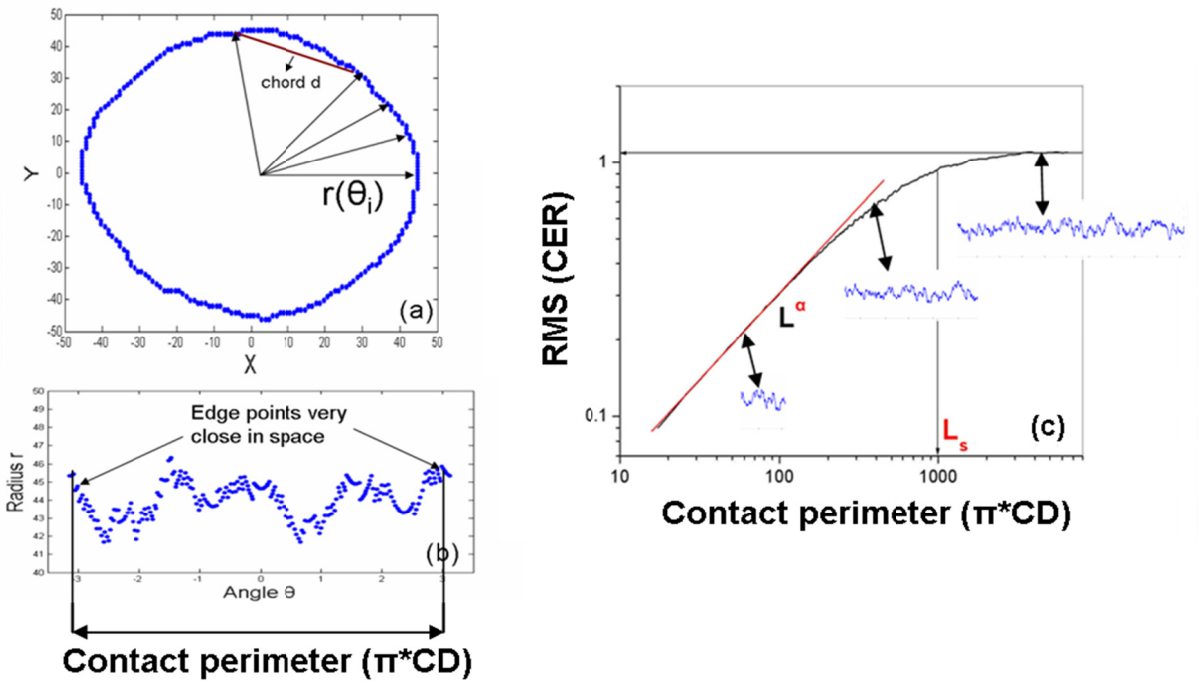

Figure 3 Schematic presentation of the contact edge length effect according to which RMS value of CER depends on the contact perimeter (c) and therefore contact CD (a,b)

Then this methodology has been applied to the analysis of experimental SEM images to examine the effects of exposure dose and resist additives (PAG, sensitizer and quencher) on CER and dimensional parameters and variability of contact holes. On the whole two resists have been studied and six different combinations of PAG, sensitizer and quencher concentrations in the second resist are used to study their effect on CER and CDU.

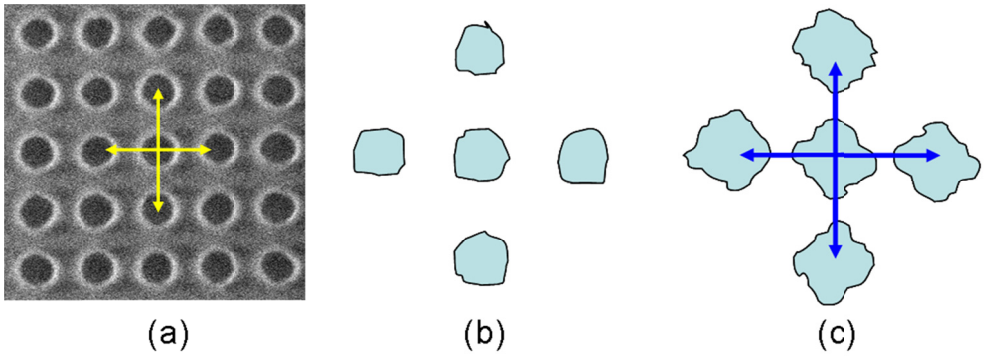

Figure 4 Schematic presentation of contact proximity effect. a) Directions in a real contact pattern of enhanced proximity of contacts, b) No effect of contact proximity on contact edge morphologies when they are distant and c) “stretching” of contact edges along the proximity directions causes low frequency undulations (“squareness”) in the contact shape and therefore increase of RMS value.

In all cases, CDU goes up at small CDs while it saturates and in some cases increases at large CD. RMS of CER presents totally different behavior with respect to dose than LER. Instead of going down with dose, it increases initially very slowly and then more abruptly. When data points for CER parameters from all experiments are plotted versus the final resist CD, they coalesce indicating the critical role of the contact diameter (CD value) in CER dependencies on resist ingredients. Both contact edge-length and contact proximity effects are determined by CD and for fixed pitch lead to increased RMS with CD. Frequency analysis of CER revealed the possible domination of the contact proximity effects and its principal role in the abrupt increase at large CD. In the same set of experiments but for fixed CD, the study of the impact of PAG loading on CER/CDU revealed a minimum at the middle (standard) PAG concentration. Recalling similar argumentation in LER dependencies, we showed that this minimum is associated with a transition from a regime where CDU/CER is dominated by PAG statistics to a regime driven by photon shot noise (PSN) effects (see Figure 5). Sensitizer and quencher effects are in accordance with LER expectations and can be explained based only on PSN effects.

To provide better understanding of the experimental results and the origins of their trends and behavior, we have also developed a modeling approach to contact hole formation. The modeling takes into account the photon shot noise effects, the acid diffusion blur of deprotection polymer statistics and a simplified threshold-based model for the dissolution. Due to its simplicity and easy implementation it can be applied to several contact holes and therefore it can consider the impact of pattern parameters such as CD and pitch. The model has been realized in the CERSIM software and a schematic flow diagram is shown in Figure 6.

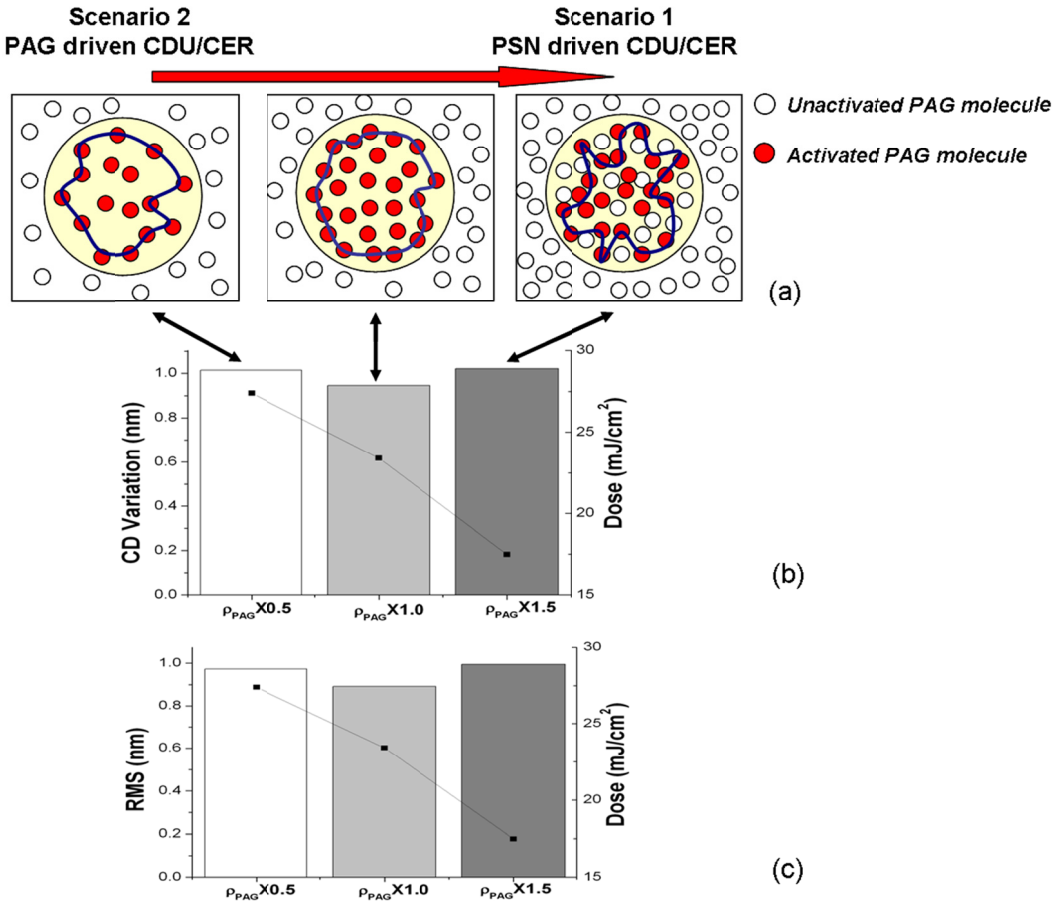

Figure 5 a) Schematic diagram of the transition from scenario 2 (PAG statistics driven CER/CDU) to scenario 1 (PSN driven CER/CDU), where the contact area is shown with yellow background, the unactivated PAG molecules with small hollow circles and the activated PAG molecules with red filled circles. Also, we show the bar diagrams for the CDU (b) and RMS (c) values at different PAG concentrations to facilitate the link to schematic diagram.

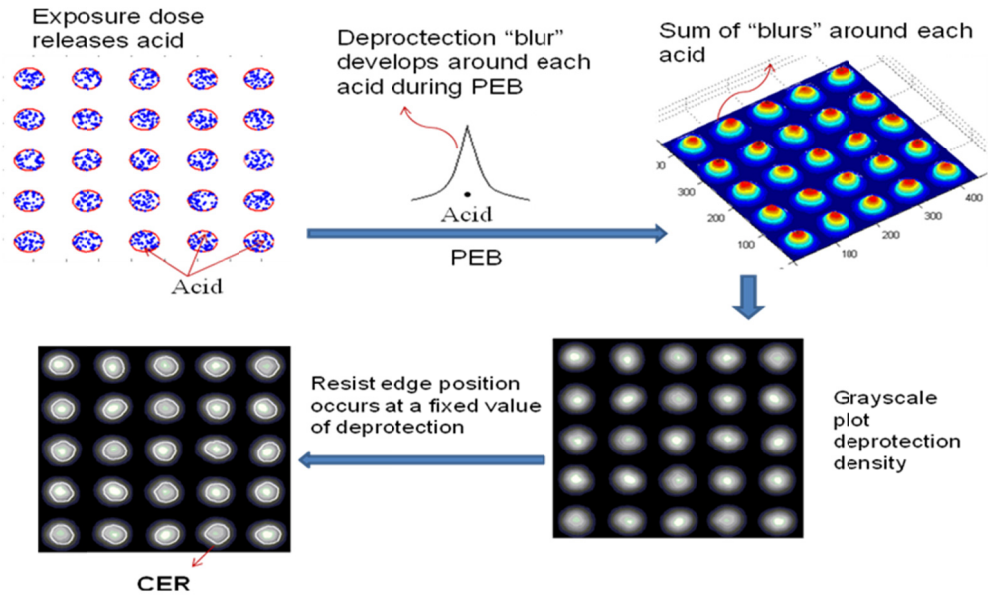

Figure 6 Schematic diagram of the flow for CER modeling

Application of the developed modeling approach confirmed the role of contact proximity effects on CER abrupt increase in large CD values and predicted the manifestation of contact edge-length effects on CER in small CDs. Finally, model showed that CDU is slightly affected by contact proximity effects especially at large CD values. PSN effects are manifested mostly in the middle CD values. Therefore, contrary to LER, dose dependence of CER and CDU is more complicated since it involves besides PSN the effects of the 2D circular topology of contacts (contact edge-length and contact proximity effects).The quantitative differences between model predictions and experimental results may be attributed to the overlooking of the effects of chemical resist in-homogeneities in our model.

Publications in Journals

1. Vijaya-Kumar Murugesan-Kuppuswamy, Vassilios Constantoudis, and Evangelos Gogolides, “Contact Contact Edge Roughness: Characterization and modeling.” Microelectron. Eng. Volume 88, issue 8 pages 2492-2495, 2011.
2. Vijaya-Kumar Murugesan-Kuppuswamy, Vassilios Constantoudis, Evangelos Gogolides, Alessandro Vaglio Pret and Roel Gronheid, “Contact edge roughness metrology in nanostructures: Frequency analysis and variations.” Microelectron. Eng. Doi 10. 1016/j.mee.2011.05.013, 2011.
3. Vassilios Constantoudis, Vijaya-Kumar Murugesan-Kuppuswamy Evangelos Gogolides, Alessandro Vaglio Pret and Roel Gronheid, “Measurement of contact edge roughness and critical dimension uniformity: Generation of synthesized SEM images and noise effects” The journal of Micro/Nanolithography, MEMS, and MOEMS (JM3) 2012. (Accepted).
4. Vijaya-Kumar Murugesan-Kuppuswamy, Vassilios Constantoudis, Evangelos Gogolides, Alessandro Vaglio Pret and Roel Gronheid, “Critical dimension uniformity and contact edge roughness in extreme ultraviolet lithography: Effect of photoacid generator” The journal of Micro/Nanolithography, MEMS, and MOEMS (JM3) 2012. (Accepted).

Conference Papers

1. Vijaya-Kumar Murugesan-Kuppuswamy, Vassilios Constantoudis and Evangelos Gogolides, “Contact Contact Edge Roughness: Characterization and modeling.” 36th International Conference "Micro and Nano Engineering 2010, Genoa, Italy, 19-22 September 2010.
2. Vijaya-Kumar Murugesan-Kuppuswamy, Vassilios Constantoudis, Evangelos Gogolides, Alessandro Vaglio Pret and Roel Gronheid, “Contact edge roughness metrology in nanostructures: Frequency

analysis and variations.” 4th International Conference "Micro&Nano2010" on Micro- Nanoelectronics, Nanotechnologies and MEMs, NCSR Demokritos, Athens, Greece, 12-15 December 2010.

3. Vijaya-Kumar Murugesan Kuppuswamy, Vassilios Constantoudis, Evangelos Gogolides, Alessandro Vaglio Pret and Roel Gronheid, “Contact edge roughness (CER) characterization and modeling: Effects of dose on CER and critical dimension (CD) variation.” Proc. of SPIE Vol.7971, 2011.
4. Vijaya-Kumar Murugesan Kuppuswamy, Vassilios Constantoudis, Evangelos Gogolides, Alessandro Vaglio Pret and Roel Gronheid, “Contact edge roughness (CER): Effect of Photo Acid Generator in a EUV resist.” Proc. of SPIE, 2012.
5. Vijaya-Kumar Murugesan Kuppuswamy, Vassilios Constantoudis, Evangelos Gogolides, Alessandro Vaglio Pret and Roel Gronheid, “Noise effects on Contact Edge Roughness measurement.” Proc. of SPIE, 2012.

LIST OF ABBREVIATIONS AND SYMBOLS

ADL: Acid Diffusion Length

AIC: Aerial Image Contrast

CAR: Chemically Amplified Resists

CD-AFM: Critical Dimension Atomic Force Microscope

CDSEM: Critical Dimension Scanning Electron Microscope

CDU: Critical Dimension Uniformity

CER: Contact Edge Roughness

CH: Contact Hole

CHR: Contact Hole Roughness

CMP: Chemical Mechanical Planarization

CVP: Chemical Vapor Deposition

DoF: Depth of Focus

DtS: Dose to Size

DUV: Deep Ultraviolet

EUV: Extreme Ultraviolet

FoV: Field of View

FT: Fourier Transform

GCDU: Global Critical Dimension Uniformity

HHCF: Height-Height Correlation Function

HM: High Magnification

IC: Integrated Circuits

ITRS: International Technology Roadmap of Semiconductors

LCDU: Local Critical Dimension Uniformity

LER: Line Edge Roughness

LM: Low Magnification

LST: Low Surface Tension

LWR: Line Width Roughness

MCP: Micro-channel Plates

Mo: Molybdenum

NA ：Numerical Aperture

NGL: Next-Generation Lithography

NILS: Normalized Image Log Slope

NMOS: N-type Metal-Oxide-Semiconductor

NTD: Negative Tone Development

PAG: Photo Acid Generator

PEB: Post Exposure Bake

PSN: Photon Shot Noise

PTD: Positive Tone Development

QY: Quantum Yield

RET: Resolution Enhancement Techniques

S/N: Signal-to-Noise

SAXS: Small Angle X-ray Spectroscopy

SD: Source Drain

SEB: Secondary Electron Blur

SEM: Scanning Electron Microscopy

Si: Silicon

TCAD: Technology Computer Aided Design

TDDB: Time Dependent Dielectric Breakdown

Tg: Glass Transition Temperature

TMAH: Tetra-Methyl Ammonium Hydroxide

CONTENTS

1. INTRODUCTION:

1.1. Motivation, aims and thesis layout:

In the past few decades there has been a significant growth and progress shown in the Microelectronics industry. In 1965, Gordon Moore observed that the density of transistors in a circuit tends to increase twice every 18-24 months [1]. This trend is now known as the famous Moore's law which is shown in the Figure 1.1. Amazingly, the semiconductor industry has maintained this pace for approximately 45 years [2]. Due to the advancement in the Optical lithography process and the method used for defining the circuit patterns on the surface of silicon wafers [3], the transistor size has decreased tremendously leading to enormous densities of packing them close together and reduced energy consumption.

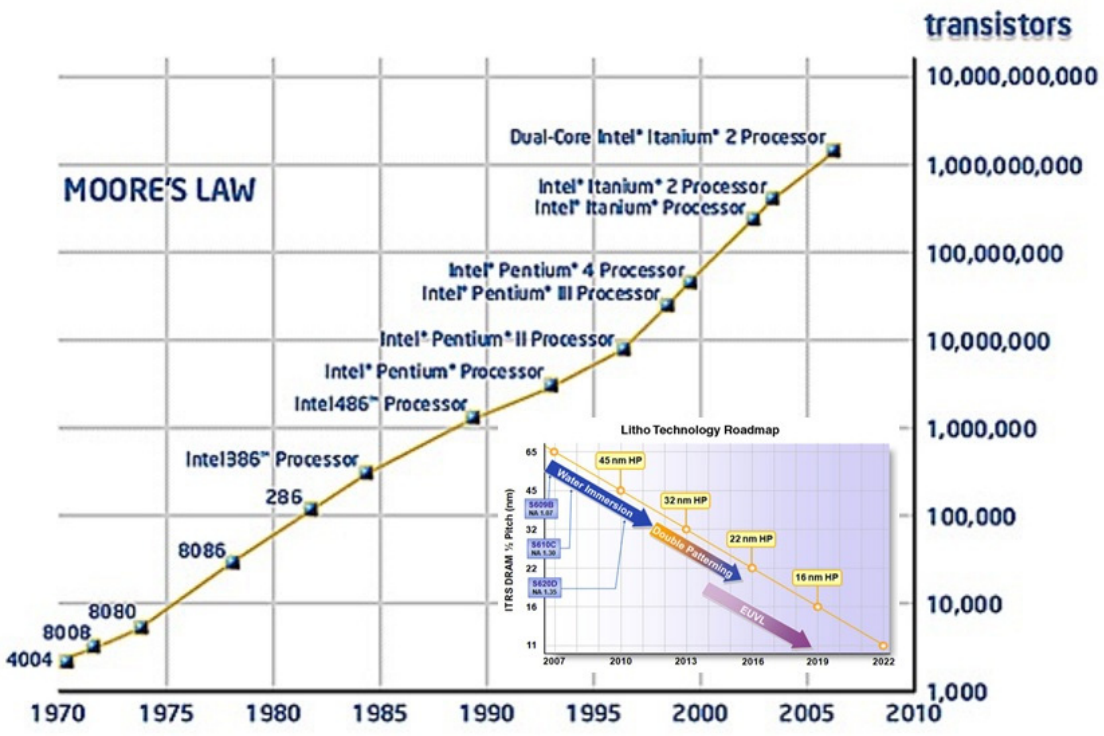

Figure 1.1 Plot of transistor counts in processor versus dates of introduction. Note the logarithmic vertical scale; the line corresponds to exponential growth with transistor count doubling every two years.

On the other hand, as feature sizes have reached below the sub-20nm regime, fundamental physical limits have begun to restrict the further development of optical lithography. It appears that an innovative technology is required if the industry is to continue the trend of Moore's Law. Several possible techniques are available which are currently under research. All of these techniques are collectively known as next-generation lithography (NGL) technologies. One of the strongest candidates which has attracted the interest and funding of chip manufacturers (for example Intel, Samsung...) is Extreme Ultraviolet (EUV) Lithography. In coming years, EUV is expected to play a vital role in the lithography world. For a high volume manufacturing of EUVL, there are three major challenges that need to be addressed simultaneously: a) source power and reliability, b) photomask readiness, and c) photoresist performance. Tin plasma is the source that is used to generate extreme ultra-violet photons. This has required new developments in materials for long lifetime and new optics for efficient collection of the clean in-band light. In addition, the requirement of such

sources in terms of power is extremely high due to their extremely low conversion efficiency during the generation of 13.5 nm photons. Secondly a major challenge is faced by the mask industry for developing a defect free multi-layer coated mask, with high degree of flatness, since any defect in reflective multilayer mask creates a mismatch in the phase of the reflected light towards the wafer. Finally, the third challenge is to develop a EUV resist enabling reliable and accurate patterning at <20nm with the high EUV photons. This resist must also exhibit high contrast for printing, in combination with sensitivity that will yield an acceptable throughput. Apart from this a successful resist must also possess excellent etch resistance. Given the increased energy of EUV photons and the ongoing shrinking of the features size, the stochastic effects emanating from the discrete nature of irradiation and matter start playing a fundamental role in the definition and uniformity of the features printed on the resist.

These enhanced stochastic effects arise two challenges in both intra-feature and inter-feature scale variation. In the intra-feature scale, the shape of the real feature deviates from the ideal one mainly due to the roughness of the feature sidewalls (see Figure 1.2 and Figure 1.3). In the inter feature scale, stochasticity contributes to the variability of the dimensions (size) of nearby similar features (Figure 1.4).

The most widely printed features on a wafer have the shape of lines or holes (circular or elliptical). Lines are printed when the gates or interconnects are fabricated while holes are opened either to form electrodes for transistors (contacts) or links between different circuit layers (vias). A single line feature fabricated will act as gate for many transistors and the sidewall roughness of this feature is known as Line Edge Roughness (LER) (Figure 1.1). Similarly, the roughness in the circular features (holes) is known as contact edge roughness (CER) (Figure 1.2). The variability of the size (Critical Dimension) of the contact holes printed on a wafer is known as contact Critical Dimension Uniformity (CDU) (Figure 1.4). When the concern is about the variability at local scale

between nearby contacts (contact inside a CD-SEM image), it is referred to as Local CDU (LCDU).

Sidewall roughness (LER and CER) and dimensional variability (LCDU) of lithographic features are transferred to the transistor components and affect its electrical characteristics and therefore the yield of their production. In particular, LER has shown to have impact on the threshold voltage V_{th} and off-line current I_{off} since it varies locally the channel length. CER can cause dielectric breakdown due to the reduction may induce to the distance between the contact and gate. In addition, CER and mainly LCDU affect transistor Source/Drain resistance and subsequently the propagation time of signals raising timing issues in circuit operation.

In order to acquire control of these degradation effects at nano-scale devices, it is important to develop methods for the measurement and characterization of the sidewall roughness and variability of the lithographic features as well as to pinpoint their material and process origins. To our knowledge, so far, the majority of works relevant to this aim have been devoted to the LER issue. However in recent years, CER and mainly LCDU attracted a lot of interest and related research programs from both academia and industry have initiated due to the inability of present lithographic techniques (including EUVL) to fabricate small contacts (CD<30-40nm) with low LCDU (3sigma<10%CD) (see Figure 1.5).

In Figure 1.6, we show schematically the “location” of the research area of this thesis with respect to the more general area of the research in microelectronics and lithography.

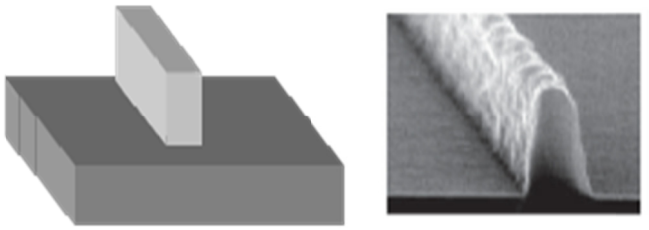

a) b)

Figure 1.2 a) Ideal line feature and b) Printed line with sidewall roughness (Line Edge Roughness, LER) (Intra-feature scale)

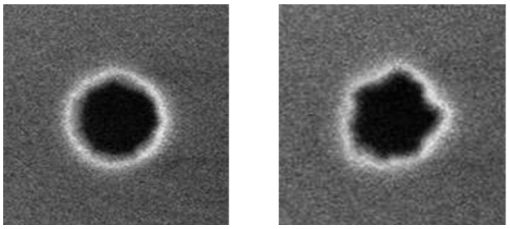

a) b)

Figure 1.3 a) Contact hole with low roughness and b) Contact hole with high roughness (Intra-feature scale)

a) b)

Figure 1.4 a) Printed contact holes with low dimensional variability and high Local Critical Dimension Uniformity and b) Printed contact holes with high variability (low LCDU)

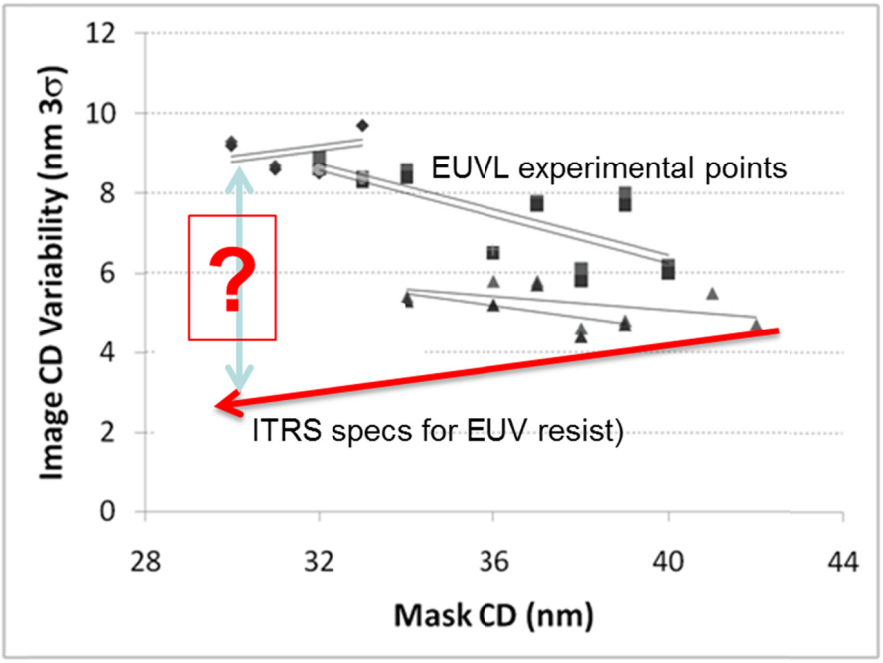

Figure 1.5 Recent results for the Local CDU (Image CD variability) of EUV resists versus mask CD. Notice the increasing trend of the CDU measurements at small CD which enhances the difference with the requirements of ITRS for keeping CDU<10%CD. At CD<30nm, the difference between where we are now with the best performed resists and where we should be according to ITRS is more than 4-5nm.

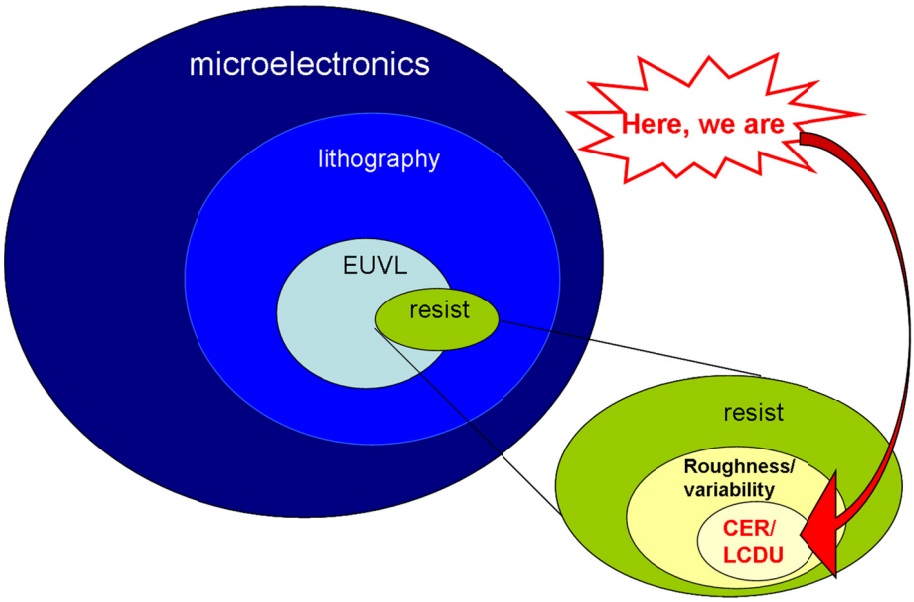

Figure 1.6 Definition of the research area of the thesis with respect to the broader region of microelectronics and its subsequent subsets lithography, EUVL, resist and roughness/variability.

The main goals and contributions of this dissertation are: a) to develop improved methodology for measurement and characterization of the CER and LCDU of contact holes, based on the analysis of SEM images and evaluation of the effects of the measurement process b) application of the methodology in the analysis of experimental data and evaluation of EUV lithography process and material effects on CER and LCDU of contact holes, and c) development of a numerical modeling for the formation of CER and comparison of the modeling predictions with experimental results.

Table 1 summarizes the flow of CER and LCDU issues from fabrication to device effects highlighting the aims and contributions of this dissertation.

Fabrication of contact holes	**Material properties**	**Process conditions**
	Resist structure *Resist components* *PhotoAcid Generator* *Quencher* *Sensitizer*	Illumination conditions Mask *Exposure dose* Post-Exposure Bake Development
Metrology of contact holes	**Techniques**	**Measured quantities**
	CD-SEM AFM Scatterometry	*Critical Dimension* Sidewall slope *Variability (LCDU)* *Sidewall roughness (CER)*
Performance of contacts in devices and circuits	**Issues**	**Degradation effects**
	CER LCDU	Dielectric Breakdown Change in transistor resistance Timing issues

Table 1 Summary of the "flow" of contact hole issues from fabrication to metrology and device effects. The topics this dissertation aims to have contribution are in italics.

Figure 1.7 explains the Thesis Layout flow diagram. Chapter 1 explains about the motivation and the aim to study the roughness and variability in the contact hole. And to continue with chapter 2 which provides a basic introduction to

lithography. This includes a brief description of principles and process flow of lithography. This chapter later continues with discussion of current challenges faced in EUV lithography. Continuing with the problem faced due to roughness in the features like line and contact holes.

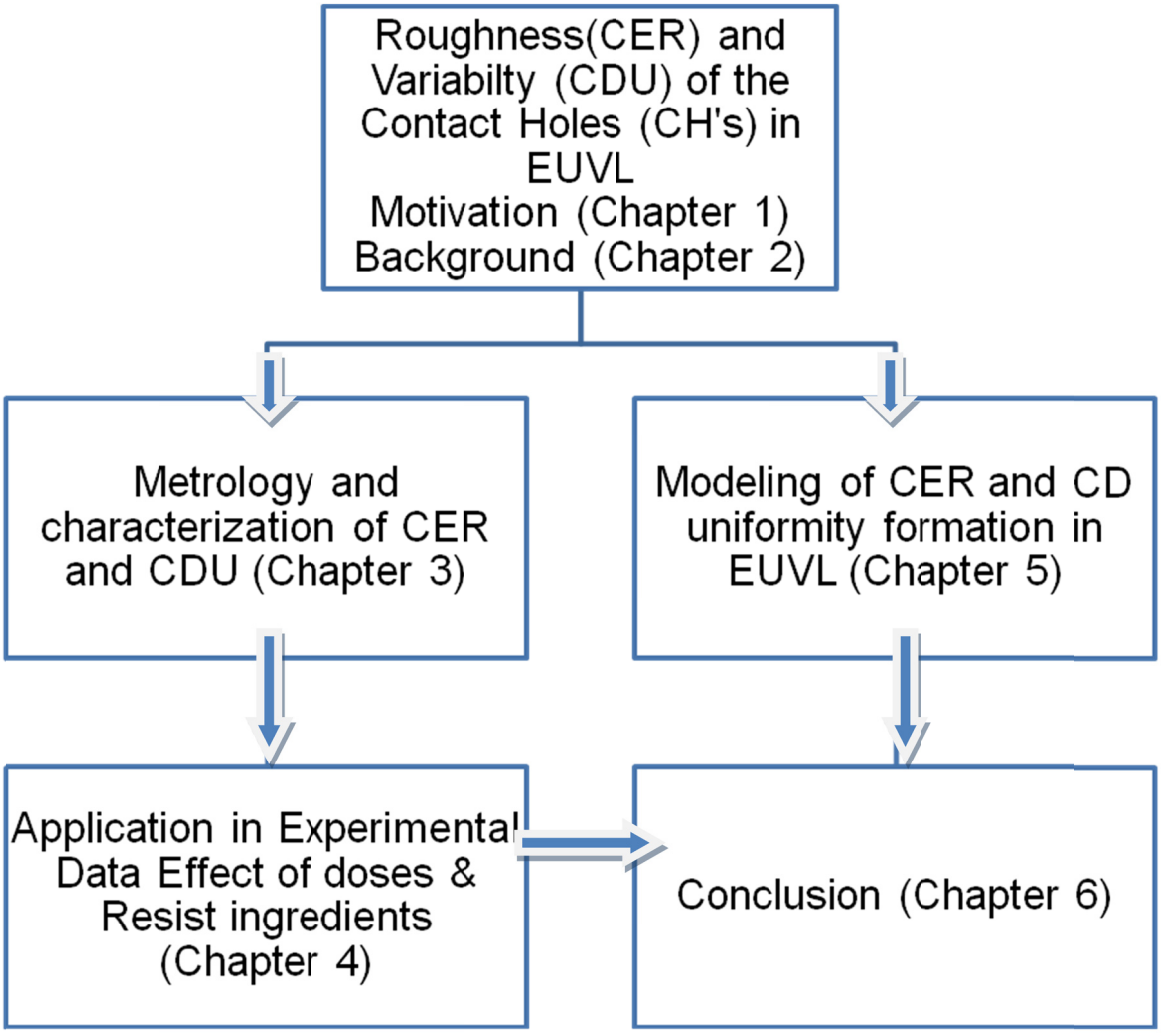

Figure 1.7 Flowchart of thesis's work and chapters

Chapter 3 is devoted to the explanation of CER and characterization methodology using SEM images. Also a brief literature survey of what has been done in characterization of Contact hole and its sidewall roughness using various techniques. This chapter later continues with our approach to the CER and dimension characterization of the contact hole. Effect of measurement

process parameters which is studied by our approach has been included in this chapter.

In Chapter 4 the characterization of EUV resist with EUV exposure dose and different concentration of PAG, quencher and sensitizer is studied. In depth, the difference between LER and CER in lithography process is also explained.

Numerical implementation of Gallatin's model for LER and CER is shown in Chapter 5. The effect of exposure dose and acid diffusion length is studied using model. Comparison with experimental and simulation results are done. The results from these chapters are combined together in Chapter 6.

Chapter 6 includes emphasis on the metrological implication of roughness in fabrication process effects at nano-scale.

2. BACKGROUND

This chapter starts with a brief introduction to the field of photolithography, with emphasis on the extreme ultraviolet lithography (EUVL). Then it focuses on the roughness issue in nano-scale feature patterning and presents some general information about its properties and more detailed account on the measurement and characterization of the sidewall roughness of line structures. Finally, the chapter ends with a reference to the importance and role of contact holes in the manufacturing of integrated IC.

2.1. Introduction to Photolithography and EUV lithography

2.1.1. Principles

Photolithography is the process in the IC that is used to produce different types of geometrical shapes and patterns onto a substrate. These patterns may be transistor gates, metal interconnect lines to connect devices, contacts or vias to connect layers, or a variety of other features. In the last few decades, photolithography has been the subject of intense research and development in order to achieve feature size below 22nm node. Though various categories of

Next Generation Lithography (NGL) are available, the basic principle and process flow are approximately the same.

2.1.2. Lithography Equipment

Figure 2.1 explains the schematic diagram of the main components of projection lithography. The main components of the projection lithography are Light source, condenser lens system, mask, reduction Lens system and finally the wafer on which the pattern will be printed.

2.1.2.1 Light Source

Currently the deep ultraviolet (DUV) lithography tool uses the light source in the range from an operating wavelength of 248 nm (KrF-excimer) or 193 nm (Arf-excimer). In case of EUVL, the light source and its operations are explained in the later sections.

2.1.2.2 Condenser and Reduction System - Lenses

Typically condenser is the one of the main component of any optical system. In optical lithography equipment, the condenser lens system is arranged in an arrangement known as K¨ohler illumination. The main advantage of this arrangement is that a pupil at the condenser may be used to control the numerical aperture of the illumination system. In the Figure 2.1 only two lenses are shown where as in practical, a numerous set of refractive and reflective lens are used in the condenser lens system.

Usually the reduction lens system is the one which projects the image obtained from the mask and passes it to the wafer. In reduction lens system, only two lenses are shown similar to that of condenser lens system, where as in practical, a numerous set of refractive and reflective lens are used.

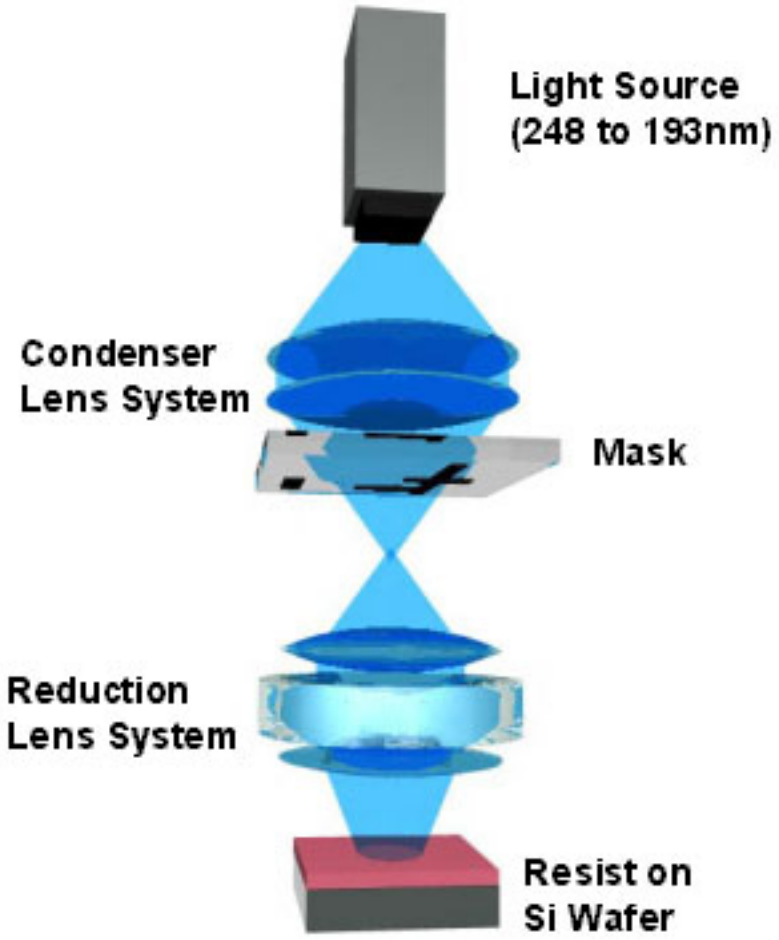

Figure 2.1 Schematic diagram of Projection Lithography

2.1.2.3 Mask

The photomask is usually made up of quartz crystal which is coated with chromium. The image for the photomask is originated from the computerized data file. With the help of this data file, the electron beam/laser techniques (writers) are used to etch the chromium present in the photomask to form the desired featured structures.

2.1.2.4 Wafer

Wafers are typically made up of silicon. This is chemically cleaned to remove any contamination and then spin coated by the photo-resist to be patterned during lithography.

In summary, during photolithography the light from the light source passes through the condenser lens system then on to the mask thus creating an image. This image passes through the Reduction lens system which reduces the actual image and then it is projected on to the Resist which is above the Si wafer. This is further sent for an etching process.

2.1.3. Process Flow

In photolithography process, light is illuminated from the source behind the mask creating a de-magnified image on the surface of the wafer along with the features present in the mask. The wafer which is already spin-coated with photoresist, undergoes chemical change when light falls on it. Then the post exposure bake (PEB) is applied on the resist to make it soluble during the development process. To increase sensitivity, modern photolithography uses the so-called Chemically Amplified Resists (CAR) in which the photons of the incident irradiation activate Photo Acid Generator (PAG) molecules specialized to generate acids. These acids during PEB diffuse and react with polymers to become soluble through a deprotection reaction. Commonly there are two types of photo-resists: Negative and Positive tone resists. In the former, the light exposed area is deprotected and becomes soluble, whereas in the latter, the irradiated part becomes insoluble by means of cross linking reactions. To remove the soluble areas, an appropriate dissolvent is used, which is known as developer. This pattern is further etched to transfer the resist pattern to the underlying film. This process is shown schematically in Figure 2.2.

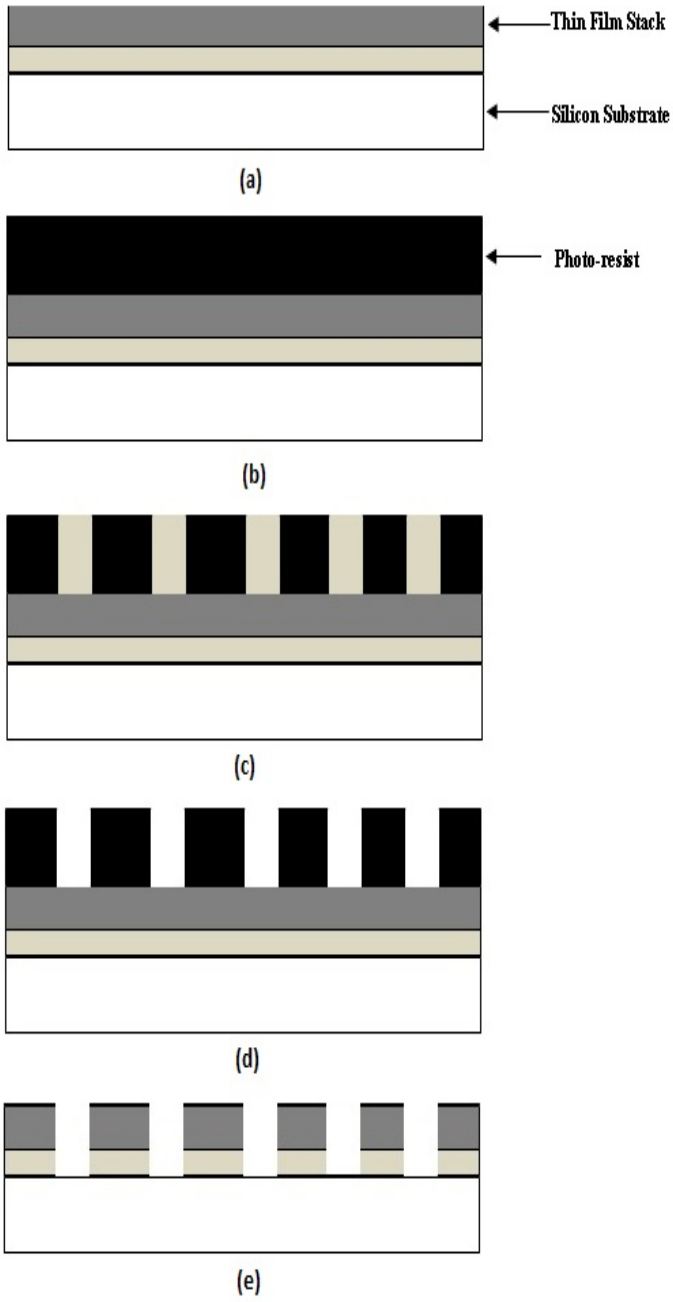

Figure 2.2 Photolithography Process flow (a) Thin film preparation, (b) photo-resist coating, (c) exposure and post-exposure bake, (d) development (e) etching and photo-resist removal.

2.1.4. Strategies for improving resolution

In the trend of miniaturization, resolution has become the important aspect for lithography process. The most commonly used definition in optical lithography is based upon the Rayleigh criterion [4][5][6]. According to Rayleigh criteria,

resolution (R) is determined by the wavelength of imaging light (λ) and Numerical Aperture (NA) of the projection lens. Thus resolution is given by the following equation.

$$R = k_1 \frac{\lambda}{NA}$$

Where k_1 is the process parameter which describes the complexity of the lithographic process i.e., as k_1 becomes smaller and smaller the process becomes difficult. This equation shows that the better resolution can be achieved by decreasing the value of λ and/or increasing the value of NA and/or decreasing k_1. The first strategy (reduction of λ) is realized by the Extreme Ultraviolet Lithography where λ=13.5nm, while the currently used immersion lithography has exploited the second possibility by increasing NA from 1 to 1.35 baptizing the whole lithographic process in water. Recently proposed and successfully implemented with success double and multiple patterning techniques increase R through increases of k_1 values. The k_1 values also increases through the Resolution Enhancement Techniques (RET) [7] such as off-axis illumination, optical proximity correction, phase shifted mask and advanced resist process techniques.

However, this design method has another challenging constraint since in modern optical systems one should also have concern about the Depth of Focus (DOF) [8] which is given by following equation.

$$DOF = k_2 \frac{\lambda}{NA^2}$$

where k_2 is another process parameter. Therefore, increasing the numerical aperture in an attempt to gain resolution has a dramatic effect on the DOF, making it much harder to obtain a stable process. The advantage of EUVL is that it combines the decrease of λ from 193nm to 13.5nm (~15 times) with a reduction of NA to ~0.25 achieving both decrease in R and increase of DOF. The DOF also restricts the thickness of the photo-resist and the depth of the

topography on the wafer. Chemical mechanical polishing is often employed to flatten topography before high-resolution lithographic steps.

2.2. Extreme Ultraviolet Lithography

The research on Next Generation Lithography (NGL) technology has been intensified due to the physical limitation occurred in conventional optical lithography. There are various contestants in the NGL; few of them are electron beam lithography, imprint lithography and EUV lithography. Each of this lithography has its own pros and cons. The work presented here is done in the context of EUV lithography, hence this section describes a brief introduction to EUV Lithography technology & differences from conventional optical lithography and the experimental setup used throughout the experiments described in the later chapters.

2.2.1. Motivation for EUV Lithography

In order to keep pace with Moore's law [1] i.e., to print features sized below 20 nm scale lithography, tool manufacturers have found it to be necessary to gradually reduce the wavelength used for imaging and to design imaging systems with ever larger numerical aperture which has been explained in the section 2.1.4. However, continued reduction of the wavelength is limited by material properties. Most materials are absorptive for wavelengths below 190 nm. Research's are done on lithography for a wavelength of 157nm (F2excimer) using the new lens material (CaF_2) instead of using current lens materials (quartz) because these are very absorptive for this wavelength. Additionally, oxygen available in the atmosphere is also absorptive; the tools are purged and replaced with nitrogen.

This technology is cost effective and the changes are difficult that may outweigh the potential benefits. However, the possibility for lithography at a wavelength

near approximately 13.5 nm exists because of the development of multilayer coatings which are reflective at this wavelength. Although this technology has many challenges, it also offers a large benefit in terms of resolution.

2.2.2. EUV Lithography Equipment

In respects, the look and feel of the EUV lithography is similar to that of optical lithography. In fact, almost all the materials including gases are highly absorptive in the extreme UV portion of the electromagnetic spectrum which requires major change in the optical lithography design [8]. Since the EUV is highly absorptive, EUV imaging must be carried out in near vacuum. In addition to this, the refractive optics can no longer be used because of the EUV absorptive nature. So instead of refractive optics, reflective optics consisting of multilayer mirrors is used. This makes the system very complex and more difficult to design than refractive system because all reflective systems have fewer degrees of freedom to vary than lens. Figure 2.3 shows the schematic diagram of the EUV lithography. Photo-masks must also be reflective, which leads to several difficulties, which are not encountered, with normal transmissive masks. EUV absorption in standard optical resist is high, and new resist and processing techniques are required in EUV lithography.

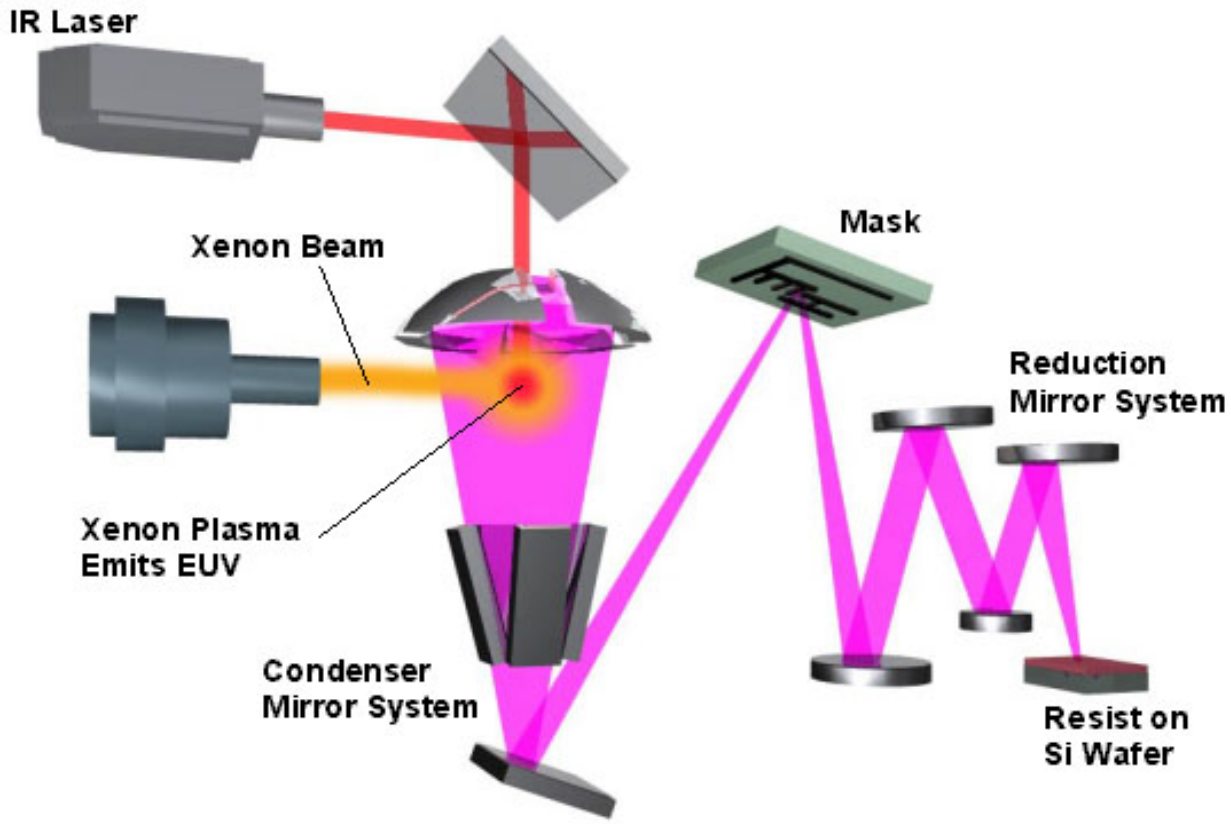

Figure 2.3 EUV lithographic systems composed by EUV source, reflective mask, reflective optics, and wafer with photo-resist spin-coated on top

2.2.2.1 Light Source

EUV radiations are obtained by the laser produced plasmas. The source must achieve a minimum of 60W of in-band EUV power to meet the throughput requirement [10]. The primary laser produced plasmas being developed for EUVL applications uses a cooled supersonic nozzle to produce a dense beam of xenon clusters which are the plasma source target. This cluster beam is then irradiated with a pulsed laser to produce a high-temperature plasma radiating efficiently in EUV spectral region [11][12][13].

2.2.2.2 Condenser and Reduction System - Multilayer Mirrors

All the materials are highly absorptive at EUV wavelengths, so the usage of refractive optical element is avoided which is stated earlier. Hence the EUVL should use reflective optical elements instead of refractive optical elements.

Since there is no single material with high enough reflectivity, the reflective surface in the EUVL system is coated with alternative multilayer thin films, which enables the high reflectivity this is also known as Multilayer mirrors.

Multilayer mirrors are formed by depositing alternating layers of two materials with different refractive indices and they provide a resonant reflectivity when the period of the layer is approximately λ/2. The materials chosen for deposition should form a long term stable interface and normally one of the materials should have a high atomic number while another having low atomic number in order to maximize the difference in electron density [14]. The multilayer materials are also generally amorphous or polycrystalline.

The most developed and best understood multilayer mirror candidate for EUV lithography uses alternating layer of silicon and molybdenum, which is first demonstrated by Barbee et al [15]. Figure 2.4 shows the reflectivity and phase change upon reflection for a Mo:Si multilayer mirror that has been optimized for peak reflectivity at 13.4nm at normal incidence [9]. Similar resonance behavior is seen as a function of angle of incidence for a fixed wavelength. In practice, peak reflectivities of the order of 65–70% are typical.

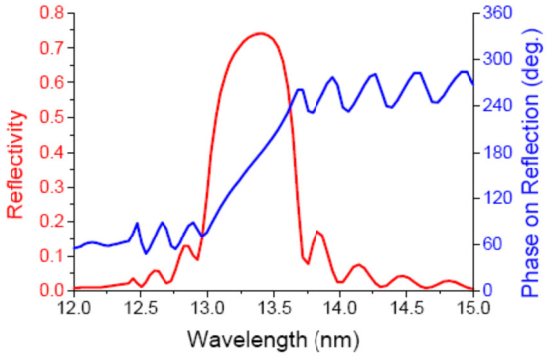

Figure 2.4 Curve showing the normal incidence reflectivity and phase upon reflection of a Mo:Si ML as a function of wavelength; the coating was designed to have peak reflectivity at 13.4 nm [9].

2.2.2.3 EUV Photomasks

The Photo-masks used in the EUVL acts as a reflector unlike as the transmitter mask that is used in the standard optical lithography. This photo-mask contains multiple layers of mirror which are arranged in such a way that they project to obtain high reflectivity of light for the desired wavelength with a patterned [16] absorbing material on the surface. EUVL masks are fabricated using processing techniques which is a standard procedure in optical lithography. Several challenges still remain with EUV masks; perhaps the most serious issue is the repair of mask defects [17] which is explained in the later section of this chapter.

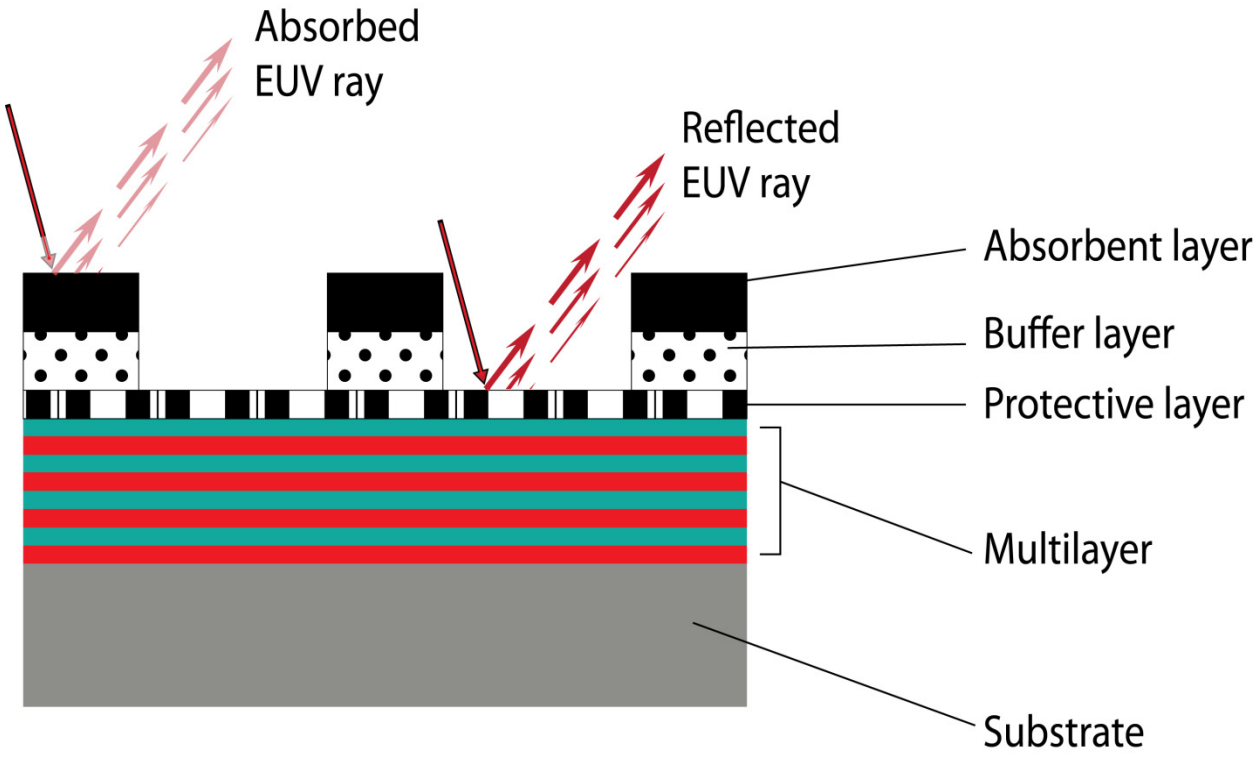

Figure 2.5 Diagram of a EUV mask

2.2.2.4 EUVL resists:

A resist is made up of a photosensitive material, as the light hits the resist there is absorption of light and it makes the material soluble. The resist materials are organic polymers and when the absorption of light (positive tone resists) occurs then they are soluble in Tetra-Methyl Ammonium Hydroxide (TMAH). Still there

are different EUV materials developed recently, to avoid acid diffusion issues that occur in conventional Chemically Amplified Resists (CARs [18]). In order to increase the improvement in Dose to Size (DtS), the PAG concentration is increased drastically. Meanwhile several approaches have been developed for acid-diffusion control to improve resolution (e.g. polymer-bound PAG[19]), the ultimate resist resolution may be provided by non CARs (including inorganic or metal-based materials[20][21][22]) but these materials typically show a penalty in terms of DtS. DtS plays an important role in the CH masks (negative resist tone) where the mask absorbs 80% of the light and only 20% of light passes through the resist [23][24]. The parallel optimization of all these aspects in a single material is quite challenging [18].

2.2.2.5 Process flow – Photoresist chemistry

In photolithography, the Photoresists are used to transfer the desired pattern from the mask to a substrate. The material needs to be photosensitive, as the aerial image modulation that is obtained from mask has to travel through the resist by making physical patterns on it using the soluble nature upon the threshold of the light intensity. Once the pattern is obtained in the resist, the subsequent processing step is to etch the pattern from resist to a dedicated substrate, material deposition, implant to dope different active area of the device, etc.

Usually resists are spin-coated onto a wafer, either directly on Silicon (Si) or on a dedicated layer stack that was previously deposited. In most of the cases, the EUV resists are directly deposited above an organic material called under-layer. This layer can be engineered for several reasons such as for the increase of resist adhesion, decrease of pattern collapse, or decrease of resist scumming and footing [25]. The under layer thickness can vary from 5 to 30nm, while the resist thickness is usually kept at a value close to the periodicity of the structures to be defined (nowadays 30-60nm), in order to have an aspect ratio of roughly 2.

Before sending the wafer to the exposure tool, the coated resist is heated to let the residual solvents to evaporate (soft bake). The solubility nature of the photosensitive resist switches depending on the light intensity (intensity threshold) that is created by the patterns of the mask and the optical system. The resist solubility does not change if the intensity is below a certain threshold. The solubility switch is highly non-linear with dose, allowing a good contrast of the printed features even for blurred aerial images. When dose is high enough, the resist thickness starts decreasing because of the dissolution switch. The dose at which the resist thickness goes to 0, and the dissolution is completed, is also called dose-to-clear.

In EUV lithography resist, the absorption of photon is generally higher compared to the DUV lithography materials resulting in resist profile degradation [26][27]. The resist absorbs the photon and generates the secondary electrons creating a relative Secondary Electron Blur (SEB). The secondary electrons with the existing energy induce further ionization and electronic excitation as shown in Figure 2.6. The inelastic mean free path of secondary electron generated by the EUV photon are less than 1nm. So the ionization and electronic excitation are distributed narrowly around the photo absorption point. This is one of the main reasons for higher resolution in EUV lithography compared to the E-Beam/X-ray lithography. These electrons can excite a Photo-Acid Generator (PAG) present in the resin, which can then generate an acid (H^+, Figure 2.6).

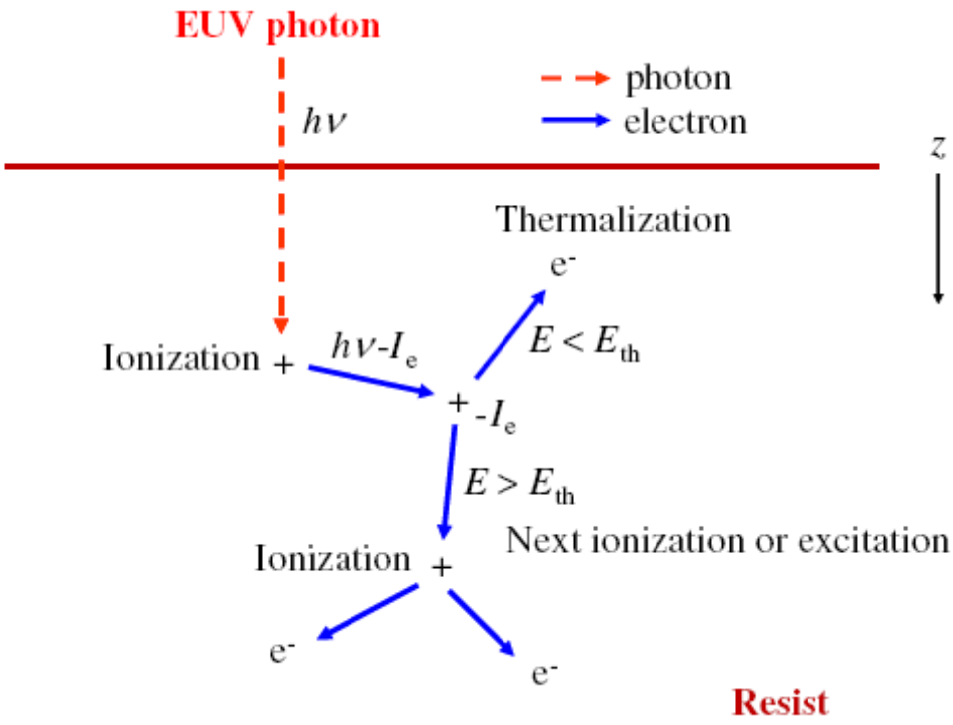

Figure 2.6 Schematic diagram of EUV resist impact

As explained by Kozawa, Biafore, Higgins and Han [28][29][30][31] there are many excitation processes which describe the acid creation in the resist: photolysis (when an EUV photon directly excites a PAG), excitation (the EUV photon dissipates energy indirectly exciting the PAG), and trapping (secondary electrons are trapped by the PAG following the Smoluchowski mechanism [32][33]). A significant difference between EUV and 193 nm DUV lithography stands in the different Quantum Yield (QY):

$$\mathrm{QY} = \frac{\#\ \text{generated}\ \mathrm{H^+}}{\#\ \text{absorbed photons}}$$

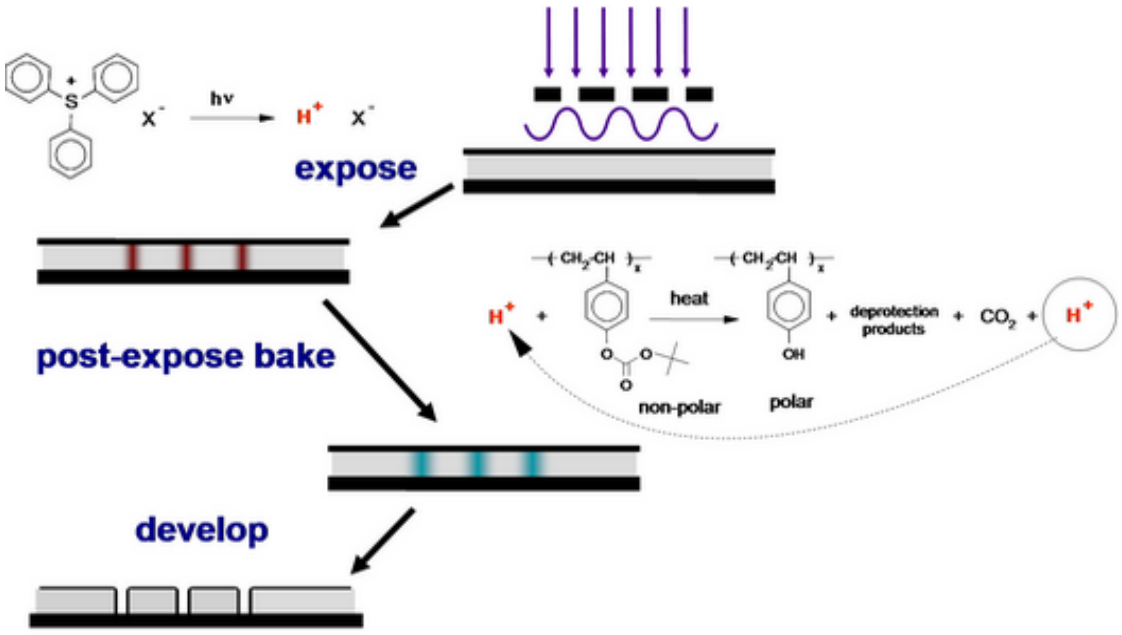

Figure 2.7 Process flow of chemically amplified resist (CAR).

In EUVL, photons are 15 times more energetic than in 193 nm DUV lithography, so that each absorbed photon can generate more than one acid [28][29][34][35] through the above mentioned excitation mechanisms. 193 nm photons have a much lower energy: they are directly absorbed by the PAGs s, and only a maximum of one acid per photon can be generated. Typical QY values are 3 or more for EUV, and 0.25 or less for ArF. This particular difference plays a fundamental role in the final resist variability [36].

Once the exposure is completed, the resist is again processed for the Post Exposure Bake (PEB). This step allows the resist to a thermally-induced acid-catalyzed deprotection of blocking groups from the polymer backbone. As a result carboxylic acid or phenolic groups are formed on the polymer backbone which renders the material soluble in aqueous base developer. In parallel to this deprotection process acid diffusion also occurs, which allows the acids to migrate to neighboring protecting groups and to repeat the catalytic cycle. In a CAR, this operating mechanism is very common for the positive tone state-of-

the-art. Once the PEB is complete, the deprotected chains of the resist are then developed with diluted TMAH (0.26N), and successively washed away with water rinse. As a result, the desired resist pattern is obtained on the wafer (Figure 2.7).

	Source	**Condenser – reduction system**	**Mask**	**Wafer (resist)**	**Process**
Conventional photolithography	248 nm (KrF excimer) – 193 nm (Arf excimer)	Large number of Refractive and reflective lens	Quartz crystals	Organic polymers Chemically Amplified Resist (CAR's)	Photo-induced acid generation and deprotection reactions during acid diffusion
EUVL	Laser activated Plasma Source	Multilayer mirrors using Molybendum and silicon	Multilayer crystals	Organic polymers Chemically Amplified Resist (CAR's) with bound PAG and/or sensitizers	Photo-induced electron production and acid generation from electron reactions with PAGs Quantum Yield 3 to 4 times higher than the Conventional photolithography

Table 2 Similarities and differences between the fundamental aspects of conventional (DUV) and EUV lithography's.

2.3. Challenges of EUVL

There are three main engineering challenges that are to be addressed simultaneously in the introduction of EUVL into high volume manufacturing.

They are a) source power and reliability, b) photomask readiness, and c) photoresist performance.

2.3.1. Source power

The chief challenge in getting EUV lithography ready for its debut has been the irradiation sources. The problem with the existing EUV source is that the light produced is not coherent. Tin plasma is the source that is used to generate extreme ultra-violet photons. This has required new developments in materials for long lifetime and new optics for efficient collection of the clean in-band light. In addition, the requirement of such sources in terms of power is extremely high due to their extremely low conversion efficiency during the generation of 13.5 nm photons [9].

2.3.2. Mask - defect detection and repair

Defects in the patterned absorber layer can be repaired using focused ion beam [36] or electron beam [38] methods. These photo-mask defects in EUVL are of two forms: a) Phase defects and b) Amplitude defects [39][9]. Phase defects are the defect that occurs due to the Mask Surface Roughness [40][41][42][43][44][45][46], which are caused by the mask fabrication process. This roughness on the photo-mask causes a mismatch in the phase of the reflected photon which leads to speckle pattern formation [47][48][49][50][51][52][53][54][55] causing intensity undulations on wafer. This leads to the roughness on the sidewalls (LER, LWR and CER) and variability of sizes in the printed features (CDU) [56]. Amplitude defects are the defect that occurs when some material on the surface of the multilayer coating causes unwanted absorption. In addition, mask feature properties such as side wall angle, corner radius, and absorber thickness have been shown to have important effects on the resulting aerial image [57].

Finally the EUV mask pattern is created by the electron beam lithography process and then followed by different types of etching processes. These two

processes generate roughness in the photo-mask pattern [58][59][60][61][62][63][64][65][66][67][68][69][70][71][72]. The roughness obtained gets transferred to the final printed features (lines and holes) on the resist.

2.3.3. Resist

In the conventional 193nm resists, one of the most well-established dependencies of LER is from exposure dose: it is inversely proportional to the square root of exposure dose, which means that less photon leads to larger sidewall roughness in printed features. There are two ways to overcome the inability of EUV sources to produce high power irradiation. The first is to increase the irradiation time (i.e., reduce the rate of the scanner system) but this is detrimental to wafer throughput and device yield. The second way is to use resist with high sensitivity to EUV light in order to obtain solubility with lower exposure dose. However, many works in literature has shown that small exposure doses lead to larger sidewall roughness in printed features due to the less number of photons used. In others words, there is a trade-off between resists exhibit higher sidewall roughness (LER/LWR) and resist with smooth sidewalls need higher dose to be developed. Therefore, the inability of EUV source suppliers to provide high powers is partially transferred to resist vendors, to synthesize the resists to meet simultaneously the requirements for increased resolution and sensitivity with that of low LER/LWR/LCDU.

Therefore, the LER/LWR and LCDU of resist patterns are a critical issue in EUVL and indeed have gained much interest during the recent years as one of the most important indices of resist and process evaluations. Other constraints which should be taken into account in parallel with LER/LWR are the thermal stability, shelf life [73], out-gassing [74], out-of-band response [75], pattern collapse [76], substrate compatibility [78], defectivity [78] and etch resistance [79] [80] .

2.4. Roughness

2.4.1. Inter-disciplinarity

Rough surfaces can be encountered almost everywhere in nature and laboratory: from the earth landscapes with the mountains, mounds and valleys at m/km scale and the soil surfaces at the scale of mm/cm to the nm/μm scale of the processed with planar techniques thin film and structured surfaces (see Figure 2.8). Therefore, their study brings together quite diverse research fields such as geology, geophysics, soil science, tribology and recently nano-science and nanotechnology. Besides applications, roughness raises theoretical issues regarding the characterization and modeling. Contributions from statistics, stochastic mathematics, fractal geometry, non-equilibrium statistical physics and even information science illuminate these aspects demonstrating the interdisciplinary character of roughness studies.

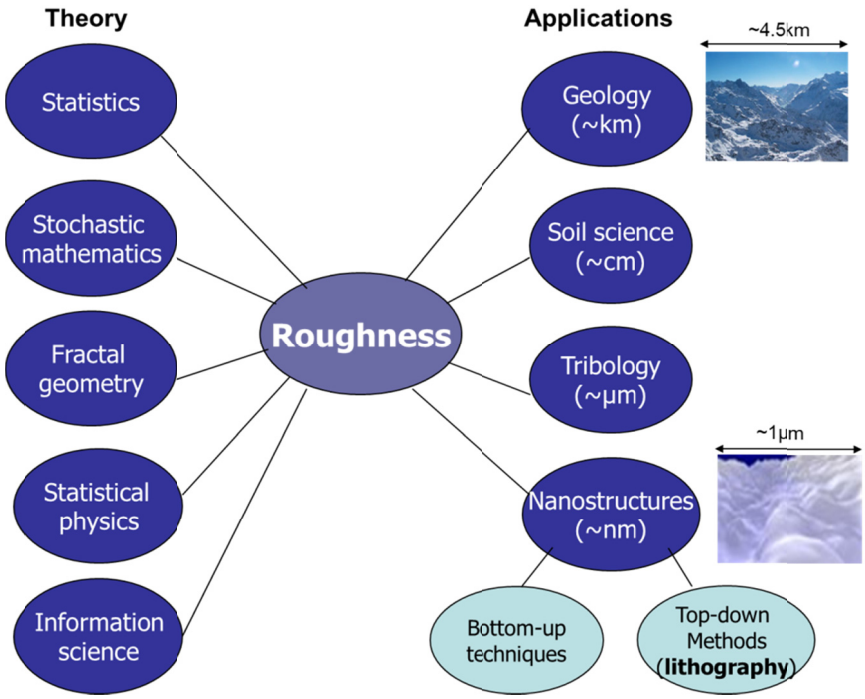

Figure 2.8 Schematic diagram of the interdisciplinary character of roughness indicating some of the research fields including roughness studies.

As usually happens in interdisciplinary topics, concepts and methods are developed independently and in parallel in different fields with similar goals but using their own terminology and mathematical tools. This offers the opportunity for transferring ideas and methods from one field to the others providing new insights and cross-fertilizing their grounds. In the next sections of this chapter, we will show how concepts and methods from fractal geometry and statistical physics have been transferred appropriately modified to the characterization of the nano-roughness of lithographic line structures. One of the contributions of this thesis is to extend these applications to the study of the sidewall roughness of nano-holes and will be described in the next chapter.

2.4.2. Definition and misconceptions

A surface (or line) is rough when their points deviate in a locally varied manner from a reference plane (or line). Usually, when we use the term roughness we mean that the deviations possess a random component. Otherwise, regularly arranged (deterministic) structures are described as topography. The term surface morphology is used in a broader sense and includes both roughness and topography.

What one should emphasize in the roughness definition is its relative nature since it depends on the choice of the reference plane or line. For example the roughness of a surface defined with respect to a flat reference plane differs than that obtained when we use as reference a curved surface.

A second misconception arises from the quantification and characterization of roughness. Quite widely and for the sake of simplicity, roughness is considered as a surface property quantified by a single number just like other properties. This number may be the standard deviation (or rms value) of the surface points from their mean value or the fractal dimension. However, roughness is more than a single number and is better characterized as a multifaceted phenomenon requiring more complex characterization schemes. Rms value or fractal

dimension captures just a single aspect of roughness phenomenon while other methods and parameters are required to provide a more holistic view.

2.4.3. Measurement and characterization

The measurement and characterization of roughness has a long history and several techniques and methodologies have been developed and applied in both academia and industry. The measurement is usually performed with either optical (non contact) or scanning probe (contact) techniques. The optical methods (scaterometry, angular spectroscopy, ellipsometry) are based on surface roughness models characterized with some statistical parameters which are defined by the comparison between measured and model predicted output signal (Figure 2.9a). On the other hand, in the scanning probe techniques (profilometer, AFM, STM), a probe scans the surface and detects its morphology giving a straightforward representation of the surface in the form of a 2D field z(x,y) (Figure 2.9b).

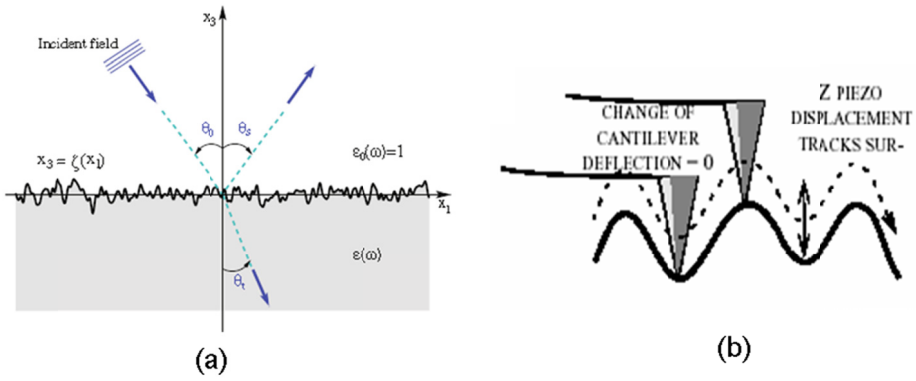

Figure 2.9 Optical (noncontact) (a) and scanning probe (contact) techniques for the measurement of rough surfaces.

Concerning the roughness characterization, one can find in literature two approaches. In the first approach, a large number of statistical parameters are estimated to provide characterization of the different aspects of surface roughness [81]. Figure 2.10 shows a selection with the most used roughness parameters categorized in height, spatial, hybrid and miscellaneous parameters. Most commercial AFM instruments have installed software which provides

several parameters for roughness characterization including those shown in Figure 2.10. The analytic formulae and detailed description of these parameters can be found in [82]. In the following section we will give more information about the parameters used more widely in the characterization of lithographic roughness.

This characterization approach suffers from two drawbacks: a) The defined parameters are not independent on each other and their meaning may overlap depending on the specific surface and b) it does not provide a concise description of surface morphology since it ignores possible hidden symmetries of surface morphology. This approach was accompanied by a random field modeling in which the surface was represented as a sum of harmonic fluctuations with wavelengths within a specific range and random phases.

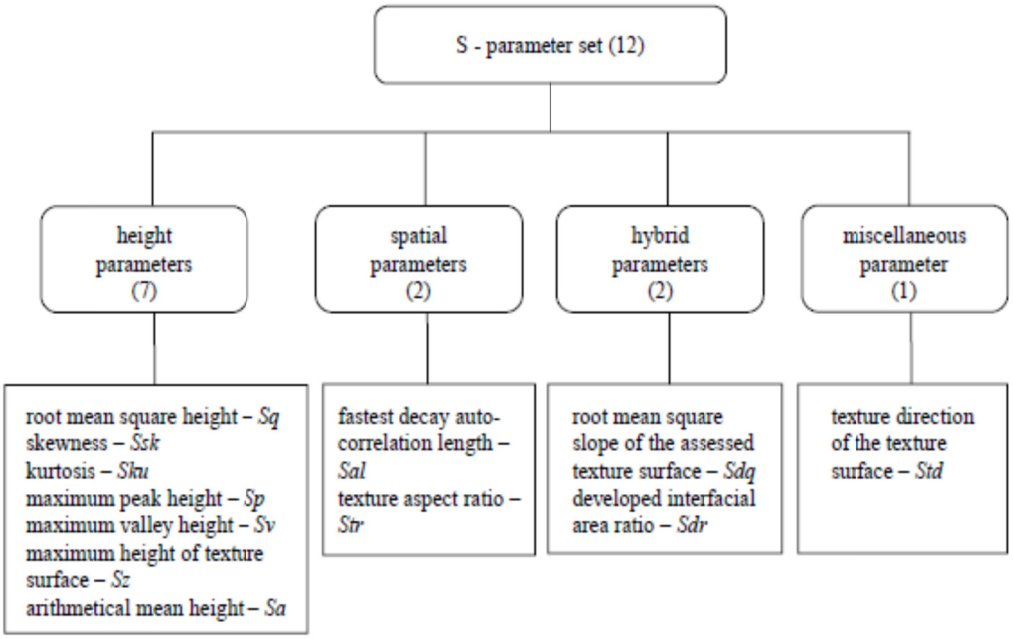

Figure 2.10 Systematic presentation of the parameters defined and applied to the characterization of various aspects of rough surfaces.[81]

The second approach was inspired by fractal geometry and based on the assumption that in most rough surfaces, the surface fluctuations obey fractal symmetry. More precisely, the assumption is that the surface morphology

remains statistically unaltered when we apply a scaling transformation to it with different factors of magnification or shrinking in the lateral and vertical to the surface directions. In mathematical terminology, this symmetry is called self-affine and actually is a generalization of the common self-similar symmetry. Both are aspects of the fractal geometry. The need for assuming anisotropic dilations is that in most surfaces height changes are much smaller than the horizontal (across wafer) width of fluctuations. This means that under isotropic transformations, the height of the fluctuations may vanish very quickly diminishing the notion of rough surface. (see Figure 2.11)

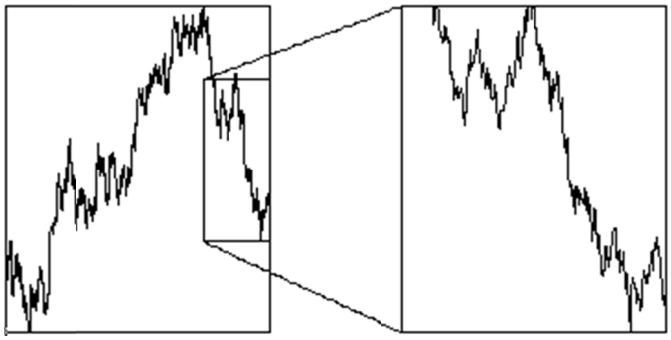

Figure 2.11 Demonstration of the self-affine symmetry: the anisotropic dilation of a part of a self-affine profile generates a profile statistically similar to the initial one.

The self-affine fractal symmetry of a surface is manifested in the power law behavior of functions characterizing the amount of surface fluctuations (differences of surface heights) at various spatial scales (or frequencies). The exponent of this power law quantifies the fractal self-affine symmetry of the surface and is related to the fractal dimension. Surfaces with high fractal dimension possess large amplitude fluctuations even at small scales (or high frequencies) with respect to those at large scales or low frequencies. Therefore, in such surfaces, high frequency fluctuations are more evident and the surface seems jagged. Extensive experimental measurements have shown that many real surfaces exhibit self-affine symmetry strengthening the assumption of self-

affinity. Therefore, according to this approach, the fractal dimension is the most fundamental parameter for roughness description.

However, in most cases the power law evidenced self-affinity is limited to a specific range of scales. At larger scales the surface heights become uncorrelated and the surface resembles white noise 2D signals.

Therefore, both approaches to roughness characterization exhibit drawbacks and a combination of these may be more reasonable and effective. A detailed description of a concise methodology for roughness characterization along with examples shown the meaning of the parameters will be given below, when we concentrate on the specific features of lithographic roughness.

2.4.4. Horizontal and vertical nano-roughness

Despite the similarity of the roughness studies in different disciplines, specific features of roughness emanated from the very nature of each field need special attention. In nano-electronics and the manufacturing of Integrated Circuits (IC), planar technology processes are used for the deposition and structuring of thin films to define the layers and components of IC. In deposited films, roughness may appear on the horizontal film surface alone, whereas in the structured films with the form of line/space grating or hole patterning the roughness of the sidewalls of the printed features should also be considered (see Figure 2.12).

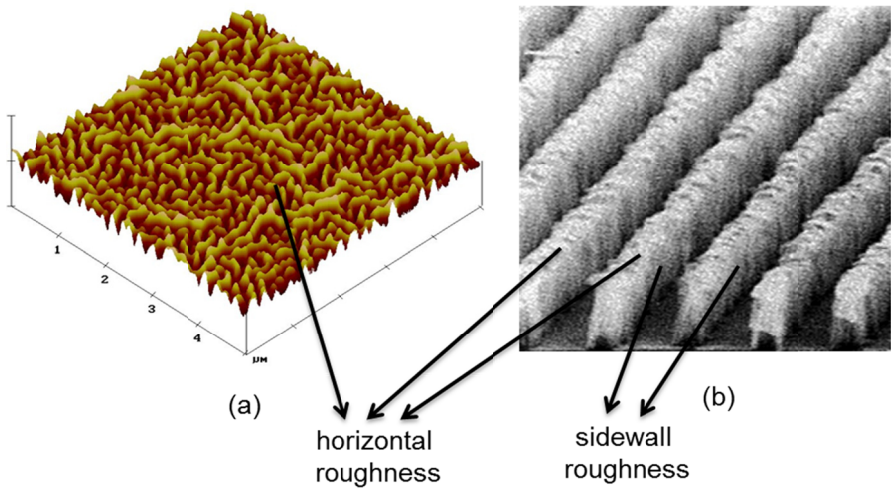

Figure 2.12 a) Film surface with horizontal roughness and b) line/space grating with both horizontal and sidewall roughness.

The horizontal roughness implies variation of the film thickness while the sidewall roughness leads to local variations in the width (critical dimension) of the printed feature (line or hole). In microelectronics, the performance of the IC components is sensitive to their dimensions and therefore the measurement and characterization of the sidewall roughness is critical towards a well-controlled IC manufacturing and performance.

The main challenge and differentiation of sidewall roughness is its metrology, since the conventional Scanning Probe Methods are more adapted to the measurement of horizontal surfaces. This challenge and the concomitant characterization issues have first been faced in LER. In the next section, we will give a brief account of the recent advances in the field of LER measurement and characterization. This work will be the basis for understanding the contribution of this thesis to CER metrology presented in the next chapter.

2.5. Roughness in lithographic features

In this section we will review the work has been done up to date on the measurement and characterization of the sidewall roughness of line/space structures, the so called Line Edge Roughness. LER attracted the interest of many researchers during the last decade since it was realized that it may be one of the strong obstacles against the on-going miniaturization of semiconductor devices. The rationale beyond this expectation is that LER causes local variations in the width (CD) of the fabricated lines (the so-call Line Width Roughness, LWR) which are transferred to the gate in the form of local variations of gate (channel) length. The latter can degrade the electrical performance of the transistor due to the sensitive dependence of electrical characteristics (threshold voltage, off-current) on the channel length.

2.5.1. Measurement techniques

The dimensional metrology of lithographic line-space structures has been usually performed with top-down CD-SEM images or scatterometry techniques [83]. Both are widely used in the measurements of the critical dimensions of lithographic features, the first being more suitable for evaluating CD variations across lines, dyes or chips. As we said above, LER/LWR is associated with local CD variations along a specific line and therefore CD-SEM (an SEM dedicated and adjusted to CD measurements on large wafers) has been the first choice for LER/LWR measurement and assessment. Scatterometry techniques and CD-AFM measurements have also been proposed and tested but CD-SEM remains to date the workhorse metrology tool for sidewall roughness measurements in lithography. Below we will give a brief account of all metrological approaches with more emphasis on CD-SEM and the subsequent characterization issues.

2.5.1.1 CD-SEM

Scanning electron Microscopy is a scientific instrument that use highly energetic electron to examine the very fine features at nano-scale. This examination can provide information about the morphology, composition and crystallographic information of the object examined. In semiconductor community, SEM is mainly used to detect the defects in the printed features and to study the size and shape of the features. Even though optical methods are very effective in measuring the CD of the printed features, the study of the variations of CD values from the designed ones as well as of the feature sidewall roughness are usually done by means of SEM. Due to the extensive use of SEM in semiconductor industry, the suppliers of SEMs have manufactured microscopes dedicated and adjusted to the measurement of the critical dimension and shape of lithographic feature which are usually called CD-SEMs (they work with low energy e-beams and accept large wafers for inspection).

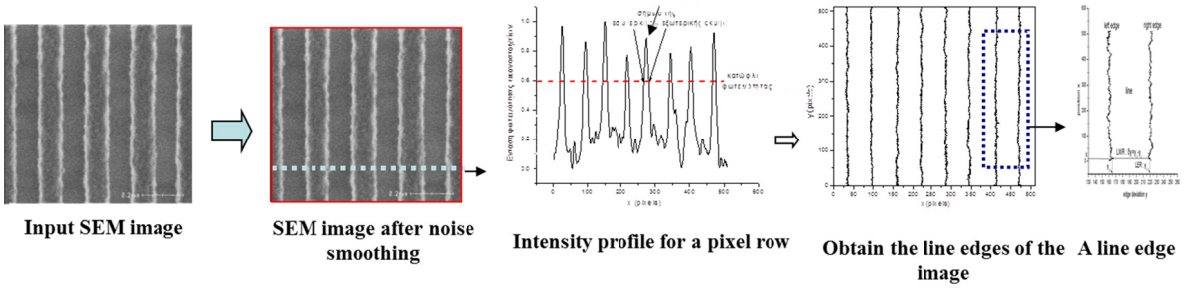

Figure 2.13 The steps followed for the extraction of line edges from an input top-down SEM image of line-space structure [84][85](Constantoudis, SPIE2003, JVSTB2004)

Figure 2.13 shows the flowchart of the measurement and characterization of LER/LWR by means of top-down CD-SEM images. First we acquire a CD-SEM image of the line-space resist structure we intend to evaluate. Attention should be paid on the parameters of SEM measurement (magnification, resolution, frame number, dwell time) so that the charging effects and the sample damage caused by SEM electrons are under control. Recent works have shown that these effects may influence the obtained LER results [86][87][88]. Then, an image noise filter is applied to reduce the noise induced in the image by the

measurement process. The choice of the filter parameters and type influence LER/LWR values and thus they should be kept fixed when comparisons are attempted [86]. The smoothed image is subsequently analyzed to detect the edges of lines. This can be done either by putting a threshold in pixel intensities or by fitting the SEM signal perpendicular to the edge with polynomial curves [89]. After the application of the edge detection algorithms, we get the coordinates of the pixels defining the detected edges of the lines included in the analyzed SEM image and the statistical analysis of their roughness can be initiated (see the next sub-section 2.5.2).

SEM has also its own pros and cons in the measurement of the dimensions and sidewall roughness of the features. The most important issues are:

a) The charging from the electrons of the SEM e-beam of the specimen structures during the measurement, which may lead to shrinking and possible damage of the structures. The shrinking effect is quite noticeable in photoresist structures and the studies for its mitigation have been primarily focused on the influence of probe current beam energy, acquisition time and measurement magnification on CD and LER/LWR values. Also models that determine the stability of CD performance, under SEM measurement have been developed and validated with experimental measurements [90]. Although shrinking has dramatic effects on CD-metrology, LER/LWR values seem to modify only slightly during the charging.
b) The noise of the measurement process coming from both instrument electronics and e-beam variations. The noise effects on LER/LWR has been discussed widely and at least three methods have been proposed for resolving it and providing noise-free LER/LWR measurements [91][92][93][94][95][96]. The first method is based on the use of multiple CD-SEM images of the same part of line-space structure and the exploitation of the independency of errors along the measured line and across multiple images [91][92][93]. The second is freed by the

requirement of using multiple images and employs the dependence of the measured LER/LWR on the image-processing parameter using for noise smoothing along edge direction, while in the third, a CD-SEM protocol has been developed based on the fitting by an analytical function of the power spectral distribution of the line roughness obtained experimentally by CD-SEM measurements. This protocol allows extraction of the equipment noise level from the output measurements and has the advantage of providing full spectral information for LER/LWR [97][98]. Also, the possibility of the first two methods to provide noise-free spatial information about LWR has also been investigated [95].

2.5.1.2 CD-AFM

Initial attempts of applying conventional AFM to LER measurement included the cleaving of the resist line space structure parallel to line direction and then the measurement of the sidewall roughness by the perpendicular to the sidewall oscillation of the AFM tip. Despite the useful results provided by this method, it is time-consuming, difficult to be performed and is limited to specific portion of the line sidewall. To overcome these shortcomings, Martin et al. [99] proposed and implemented a new AFM setup enabling the direct measurement of the surface topography of 3D structures. The key element of this setup was the use of a tip with T-shape and the ability to perform oscillations in the plane (x, z) (see Figure 2.13). These new developments along with the advanced electronics for servo control made this new AFM an appropriate tool for CD and LER/LWR measurements. First applications of the CD-AFM to LER metrology was limited by the large radius of the used tip (120 nm) [100]. More systematic measurements

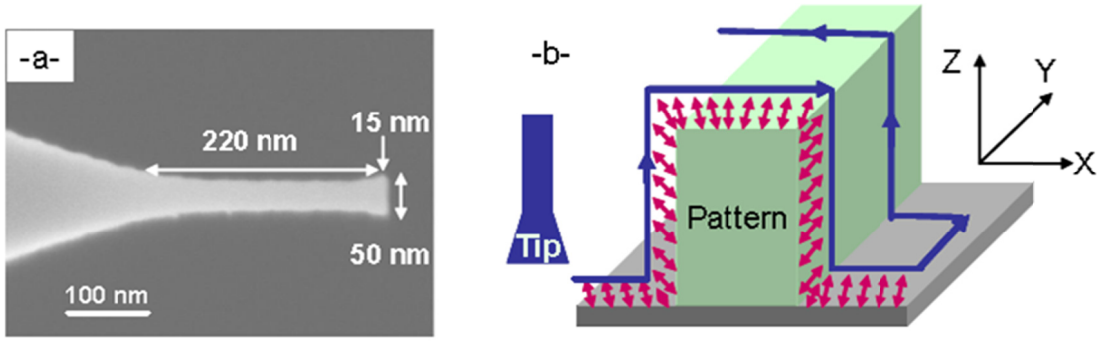

Figure 2.14 Basic principle of the 3D AFM measurement: a) The flared Si tip used for the measurements and b) the CD Mode scan principle [108]

with smaller tip radius (50nm) of the effects of acid diffusion length and etching steps on LER/LWR were also performed and partially compared with the results of the more mature CD-SEM measurements [101][102][103]. Similar trends versus CD were found when the sidewall slopes were larger than 89^{o}, however, systematically CD-AFM-measured-LER was larger than that obtained from CD-SEM. This difference was attributed to the unclear relationship between the 1D CD-SEM representation of LER with respect to the more complete 2D sidewall topography extracted by CD-AFM as well as to the tip size effects [104][105]. Furthermore, the different contribution of noise effects in two techniques may have an influence on the observed difference. Recent studies focused more on calibration with Transmission Electron Microscopy issues, extraction of high order tip effects and monitoring the effects of tip conditions on line profile measurement [106][107][108][109][110].

2.5.1.3 Scatterometry

Scatterometry techniques, are widely used for CD measurements due to their advantages (high throughput and non-destructive), but have not yet been established for LWR metrology. Several relevant works have been published recently: The more systematic approach was undertaken by NIST and was based on the use of Small Angle X-ray Spectroscopy (SAXS) [111][112][113]. It was found that random LER is related with the ratio of the scattering intensities along the equatorial line of the diffraction spectrum when LER is present to the

intensities of the ideal smooth (no LER) pattern. Comparisons with CDSEM results showed superior evaluation of LER with scatterometry. This was attributed to the global character of scatterometry measurements and the concomitant inclusion of very low frequency fluctuations. Other approaches employ dark-field scatterometry, ellipsometry, angular resolved scatterometry, etc. [114][115][116][117]. Modeling studies have been also performed testing new techniques in simulating the effects of LER on scattered light such as the field-stitching method [118].

2.5.2. Characterization of LER/LWR

Let us assume that the line to be analyzed is known (has been measured) at N positions x_i, $i=1,..,N$ on both edges and $y_{l,i} = y_l(x_i)$ ($y_{r,i} = y_r(x_i)$) are the distances of the left (right) edge points from a reference axis on the left side of the line which is considered parallel to line direction (see Figure 2.15). The LWR is the roughness of the differences (line widths) $\delta y_i = y_{r,i} - y_{l,i}$ while the LER is the roughness of the $y_{l,i}$ or $y_{r,i}$. The following definitions of spatial roughness functions are written for the edge points y_i ($y_{l,i}$ or $y_{r,i}$) and refer to LER, but they also hold for the line widths δy_i and for LWR.

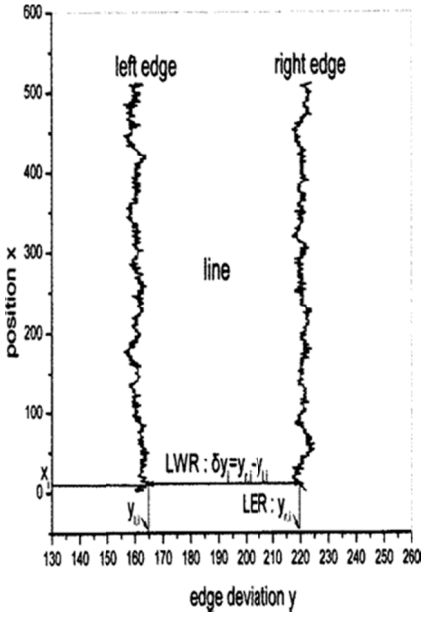

Figure 2.15 Detected edges of a typical resist line along with the definitions of LER and LWR.

The most widely used metric for the quantification of LER/LWR has been the standard deviation of the edge points from their mean value (rms value) σ_{LER}:

$$\sigma_{LER}^2 = \frac{1}{N}\sum_{i=1}^{N}(y_i - \langle y_i \rangle)^2 \quad (1)$$

where $\langle y_i \rangle$ is the average of all y_i, i=1,..,N. Despite the widespread use, rms value σ suffers from some related drawbacks. First it depends on the spacing between two nearby measurement positions d and the length L (=(N-1)d) of the edge included in the measurement process [84][91][119][120]. More critical is the dependence on L implying that actually rms is not a single value but an increasing function of line length L. The 2007 edition of ITRS recognized this dependence and dictated that lines with lengths larger than 2μm should be used in the estimation of rms based on the experimental observations that usually rms saturates above this critical length. Second, the dependence of rms is related to the spatial and/or frequency aspects of LER/LWR i.e. the spatial arrangement of the fluctuations of edge points or line widths along the line, which are overlooked in a single value of rms, but may be critical for the effects of LER/LWR on device performance [85][121]. These spatial fluctuations can be quantified by three ways:

2.5.2.1 Correlation functions

The most commonly used metric of the correlations is the autocorrelation function which for the case of edge points takes the form:

$$R(r = md) = \frac{1}{\sigma_{LER}^2}\frac{1}{N-m}\sum_{i=1}^{N-m}(y_{i+m} - \langle y_i \rangle)(y_i - \langle y_i \rangle) \quad (2)$$

where $d=|x_{i+1}-x_i|$ is the distance in the direction of the line between two neighboring measurements and $\langle y_i \rangle$ the mean edge position. Due to the normalization prefactors in (2) R(r=0)=1 while $R(r\rightarrow\infty)=0$, since the correlations are expected to tend to zero at long distances. Examples of autocorrelation functions of resist LER/LWR can be found in [121][125]. Another correlation function used in LER characterization is the height-height (or height difference) correlation function (HHCF) G(r) defined as [84][85]:

$$G(r=md)=\left[\frac{1}{N-m}\sum_{i=1}^{N-m}(y_{i+m}-y_i)^2\right]^{1/2} \quad (3)$$

The HHCF is related by definition with R(r) through

$$G^2(r)=2\sigma_{LER}^2[1-R(r)] \quad (4)$$

and it is used to reveal the scaling properties of the analyzed data. Obviously G(r=0)=0 and G(r→∞)=√2σ$_{LER}$. A typical G(r) of resist LER is shown in Figure 2.16 a.

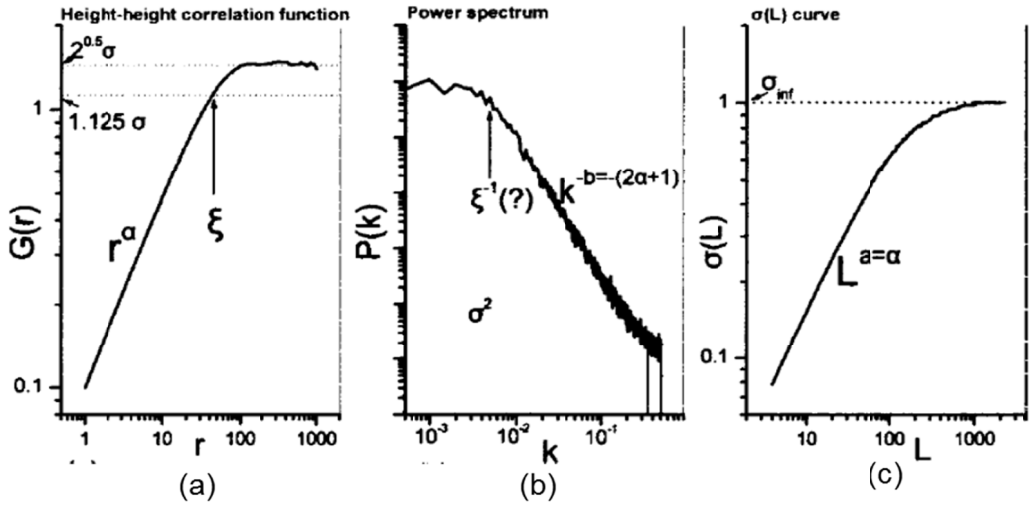

Figure 2.16 Typical behaviors of the HHCF (b) the Power Spectrum (c) and the σ(L) curve (d) of the LER/LWR [85].

At small r, G(r) increases following a power law which reveals the presence of fractality (or more accurately self-affinity) in LER. The exponent of the power law is usually called roughness exponent α and is related to the fractal dimension d of the edge through d=2-α (0<α<1). Low (high) values of α correspond to edges or lines with enhanced (reduced) contribution of high frequency fluctuations to LER. As we can see in Figure 2.16 a, the power law behavior has an upper boundary above which the HHCF saturates or oscillates randomly around the value √2σ$_{LER}$. The upper boundary of fractality is defined by the correlation length ξ which quantifies the average width of edge asperities. ξ may be defined

by R(ξ)=1/e (or equivalently $G^2(\xi)=(1-1/e)2\sigma_{LER}^2$) or by fitting R(r) or G(r) with an exponential or other suitable function to the neighborhood around r=0. For r>ξ the edge point correlations can be considered negligible. Therefore, the analysis of a typical HHCF of LER leads us to a three parameter model for LER characterization consisting of the parameters σ_{LER}, ξ, α. The prerequisite for the validity and application of this model is the limited scale fractality of LER. In case of the presence of some periodicity, the wavelength of the periodic repetitions should be added. In most real experimental lines the correlation length is estimated in the range 20-50 μm, while the roughness exponent lies between 0.5 and 0.7.

2.5.2.2 Power spectrum.

Fourier transform (FT) analysis is one of the most powerful tools in signal analysis for revealing the frequency content of a signal. Given that a line edge is actually a spatial signal, Fourier analysis can also be applied to the characterization of the spatial/frequency aspects of LER. The discrete Fourier transform of LER is defined as:

$$F(f_k) = \sum_{m=0}^{N-1} y_m e^{-2\pi i\, k\, m/N} \qquad (5)$$

and the more widely cited Power Spectrum (PS) as the square of FT amplitude:

$$P(f_k) = \frac{2d}{N^2}\left|F(f_k)\right|^2 \qquad (6)$$

Where $f_k=k/(Nd)$ is the frequency corresponding to the k-th component of the Fourier transform, and $d=|x_{i+1} - x_i|$.

A typical PS in log-log scale is shown in Figure 2.16 b. A plateau at low frequencies is followed by a power law decrease at high frequencies. Not surprisingly, the behavior is the inverse of that exhibited by HHCF (see Figure 2.16 a). The power law decrease is an indicator of the presence of fractal self-affine symmetry at high frequencies corresponding to the short distance behavior of HHCF. The fractality is limited to high frequencies, whereas at low frequencies there is a uniform contribution from all frequencies resembling the

white noise behavior of uncorrelated data. The exponent of the power law b is related to the roughness exponent α since b=-(2α+1), whereas the correlation length ξ is related to the inverse knee frequency marking the passage from the plateau to the power law behavior. The amplitudes of PS are related to rms value σ_{LER} through the Parseval's theorem, which for the discrete data of LER/LWR takes the form:

$$\sigma_{LER}^2 = \frac{1}{(N-1)Nd} \sum_{k=0}^{N/2} P(f_k) \qquad (6)$$

which means that σ_{LER}^2 is equal to the area under the $P(f_k)$ curve.

In conclusion, the three parameter model suffices to characterize the PS of LER obeying the fractal self-affine symmetry and exhibiting the form of Figure 2.16.

2.5.2.3 The σ(L) curve

In statistical theory, it is well known that the standard deviation of correlated data depends on the size of the data and this dependence is indicative of the nature and extension of correlations. Therefore, the estimation of the dependence of rms on the line length of the measured sample (the σ(L) curve) may be considered the third method for the description of the spatial characteristics of LER. For LER exhibiting fractal self-affine behavior, the σ(L) curve has a form similar to that of HHCF, but with different scales (see Figure 2.16 c). A power law growth degrades gradually as line length L increases and at large L (>2μm) saturates to its final (length-independent) value. It can be shown that the exponent of the power law at low L is the same with that of the HHCF (i.e. the roughness exponent), while the knee value at which saturation starts is called rms-correlation length L_C. Numerical calculations with model edges and experimental results have shown that L_C is about 10ξ. The meaning of the σ(L) curve is that the intrinsic to an edge rms roughness decreases when the length of the edge is reduced below the rms-correlation length (~100-500 nm) and that this reduction is controlled by the spatial LER parameters ξ and α. Consequently, the form of the σ(L) curve can be fully characterized by the three-parameter model obtained from the study of the HHCF and PS. We will come

back to this curve and its importance when we discuss the LER effects on transistor performance.

2.5.2.4 LER and LWR

The above spatial and scaling analysis of LER along with the related definitions and formulas can be transferred to LWR replacing y_i by δy_i. For uncorrelated left and right edges exhibiting similar scaling behavior, it can be shown that $\sigma_{LWR}=\sqrt{2}\sigma_{LER}$ while the correlation length and roughness exponent remain almost unaltered. More information about the relationship of LER and LWR can be found in [84] and [89].

2.5.2.5 Experimental validation of the three-parameter model

The three-parameter model introduced in the previous sub-sections is based on the assumption that LER/LWR exhibit fractal self-affinity symmetry, i.e. the edges and lines remain invariant under anisotropic scaling transformations, in a limited range of scales. This assumption was verified by thorough experimental measurements [122][123], which showed that indeed experimental LER/LWR from many resists exhibit scale-limited fractal self-affinity demonstrated by the power law parts in HHCF, PS and σ(L) curve. Scale-limited power laws, especially in PS, have also been observed in the LER/LWR analysis from other researchers and therefore can be considered a generic property of the conventional 193 and 248nm resists as well as EUV resists [89][96][124][125][126]. Furthermore, the potential of the three-parameter model has been recognized by the litho-metrology community and the correlation length of LER/LWR has been added to the specifications for resist evaluation in the last editions of the International Technology Roadmap for Semiconductors (ITRS) 2011[127].

The majority of LER/LWR measurements come from top-down SEM images after application of in-line or off-line algorithms to extract the edge points and/or line widths. Following edge detection they usually calculate the rms value of the

edge points or line widths, and if they aim at a more thorough study they proceed to the estimation of the PS. More rarely the HHCF or σ(L) curve is calculated. Through these functions the correlation lengths and roughness exponent are extracted by applying appropriate thresholds and estimating the exponents of the power laws respectively. Also, model HHCF and PS including the CER parameters have been used to fit experimental data and obtain the values of the parameters while recently a bootstrap approach along with a modified variogram model has also been proposed [128].

2.6. Contacts in devices: The impact of CER and CD variation

In a semiconductor device, the design of the layers contains various numbers of features in different types of dimensions and shapes. In most cases, these features are lines and holes. Lines are fabricated when the gates and interconnects are fabricated, and holes are fabricated to form the link between different layers of the device (vias) or the electrodes of a transistor (contacts). A 3D schematic view of the position of contacts in a transistor is shown in Figure 2.17.

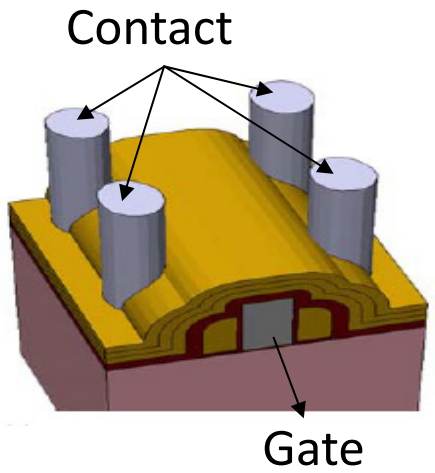

Figure 2.17 3D structural views of the contacts of a transistor

The variation in the gate length of transistor gates induces variations in the performance of the devices. Similar kind of variation effects occurs in the CD of a contact hole too. In the following sub sections, we detail more the degradation effects of CER and CDU on transistor performance.

2.6.1. CER and CDU effects on device

There are two possible variations that can occur in the size of contact hole, that is, oversize and undersize contact holes. An oversized contact hole may cause an electrical short circuit, since it can overshoot the edge of the pattern below to which it is in contact. Similarly for an undersized contact hole, the electrical contact resistance will increase since the contact resistance is inversely proportional to the area of the contact and thus to the square of the contact diameter. A 10 % decrease in contact CD causes a roughly 20% increase in contact resistance. If the contact/via resistance gets too high, signals propagating through that contact will slow down raising timing issues in the circuit performance. For voltage-sensitive parts of the circuit (such as the source/drain contacts), variations of contact area cause also changes in the voltage drop across the contact and therefore degradation of the electrical characteristics of the device [129].

Ban et al. used a commercial HSPICE simulator to estimate the effects of contact CD on the S/D resistance and saturation current [130]. The results in NMOS devices for nominal CD=40nm show that contact resistance dramatically increases at small CD whereas the current drops down (see Figure 2.18). In both cases, the sensitivity to contact CD (slope of the curve) goes up as CD scales down indicating that CD variability becomes more effective in yield losses at small scales.

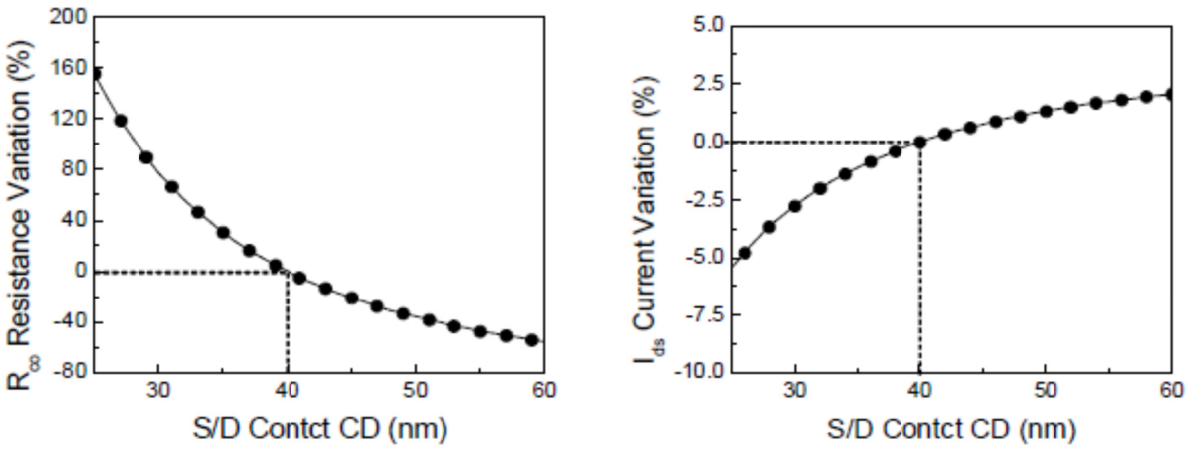

a) b)

Figure 2.18 The impact of contact CD on S/D (a) resistance and (b) saturation current [130][131]

Furthermore, CER may be accompanied with the presence of spokes on contact edges in which the electrical field can be significantly enhanced and cause time-dependent dielectric breakdown and consequently loss of yield (see Figure 2.19 for a definition of a contact edge spoke).

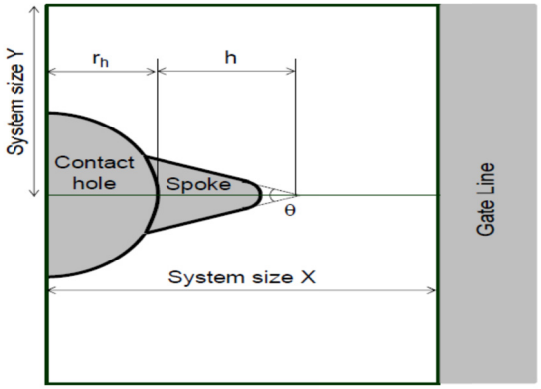

Figure 2.19 Schematic representation of a spoke in a contact edge along with its characteristics: height *h* and angle *θ*.[132]

Momonoi et al., [132] using 2D FEM to solve the Poisson equation, have calculated the electric field enhancement for various contact spoke heights and angles and the results for the normalized electric field E_{max}/E_o, where E_{max} is the electric field at the tip of the spoke and E_o is the maximum electric field strength at the point of circumference when the contact has no roughness, are shown in Figure 2.20. Based on similar interconnect LER evaluation results, it was argued

that the threshold for time dependent dielectric breakdown TDDB acceleration is ~2. Therefore, the process yield will be defined by the amount of contact holes with spokes characterized by height and angle leading to normalized electric field <2 (black line in Figure 2.20).

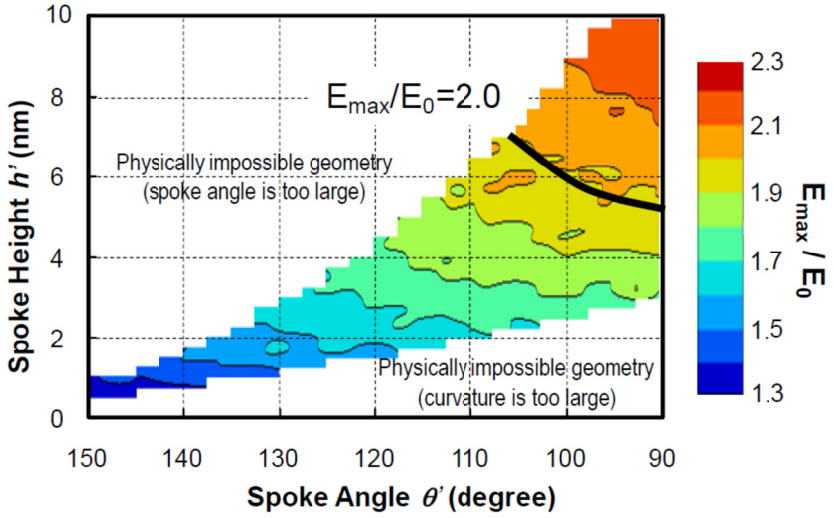

Figure 2.20 Simulation result E_{max}/E_o as functions of spoke angle and height

2.6.2. CER and CD variability in stress-induced devices

In devices which use the stress enhancement technique, the mobility of carriers in the substrate depends on the space of contact hole to gate poly line since the proximity of contact hole may locally relax the actual strain in channel and decrease mobility and saturation current. Therefore, in stress-induced devices, besides spokes and contact area effects, CER and CD variability impacts transistor performance through changes in the contact to gate space and contact shape. Indeed, simulations by Ban et al. showed that saturation current drops down when contact to gate distance (Figure 2.21) and contact height are decreased (Figure 2.22).

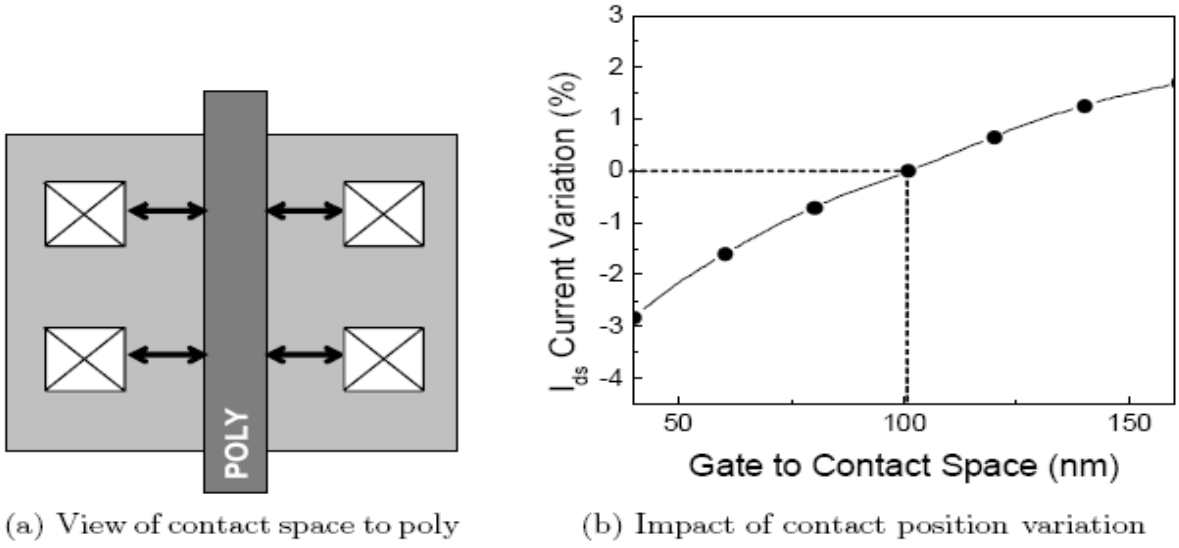

(a) View of contact space to poly (b) Impact of contact position variation

a) b)

Figure 2.21 a) View of Contact space to poly. b) Impact of contact position variation.[130]

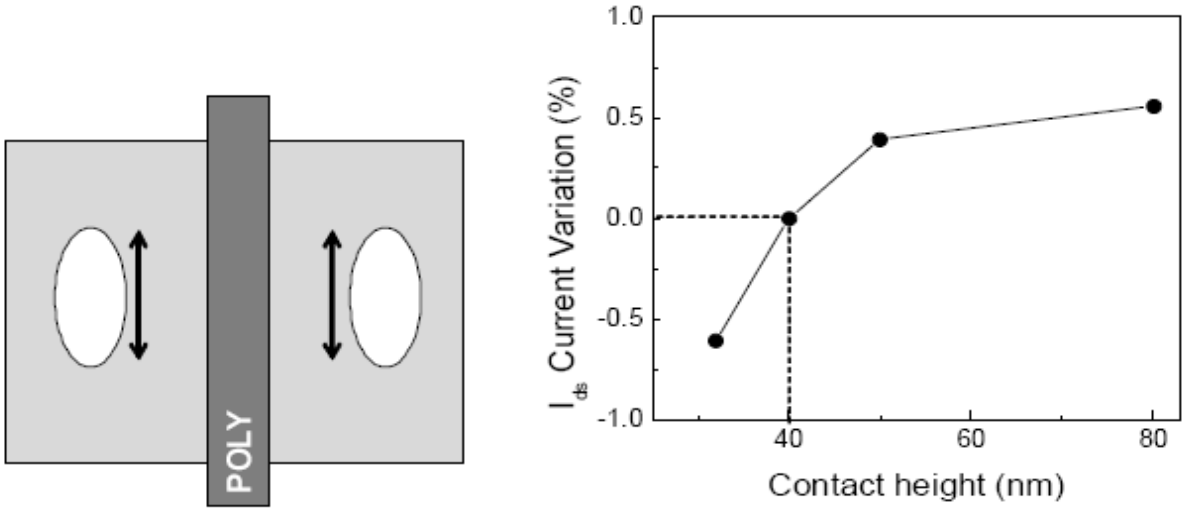

a) b)

Figure 2.22 a) View of Contact space to poly. b) Impact of the compact shape.[130]

To relate these findings with CER present in real contacts, Ban et al. have proposed a new compact model.

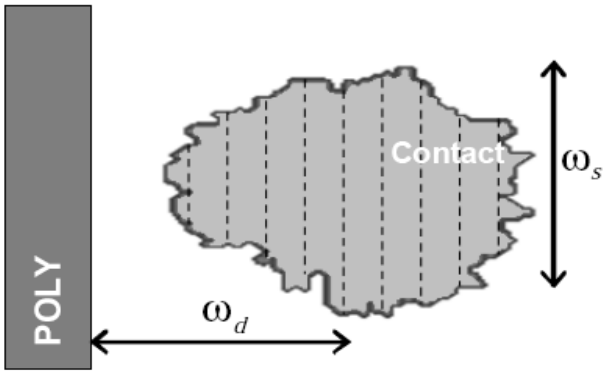

Figure 2.23 Compact model of S/D Contact [130]

The main idea of this model is to slice down the contacts vertically in a set of equal-width polygons keeping the original contact edge as shown in Figure 2.23. Then, the sliced polygon area, the shape weighting factor (ω_s) and the distance weighting factor (ω_d) are calculated. The weighting factors can be directly related to the saturation current. Then, the resistance R_i of the i_{th} polygonal slice can be calculated through the formula

$$R_i = \frac{\rho}{\omega_{s,i}\omega_{d,i}A_i},$$

where ρ is the resistivity, A_i is the i_{th} slice area and $\omega_{s,I}$ and $\omega_{d,i}$ are the shape and distance weighting factors of the i_{th} slice.

Summing the contributions from all slices to the S/D saturation current, the following formula is obtained:

$$I_{\mathrm{ds,sat}} \propto \sum_i \frac{1}{R_i} = \frac{1}{\rho_i}\sum_i (\omega_{\mathrm{d},i}\omega_{\mathrm{s},i}A_i).$$

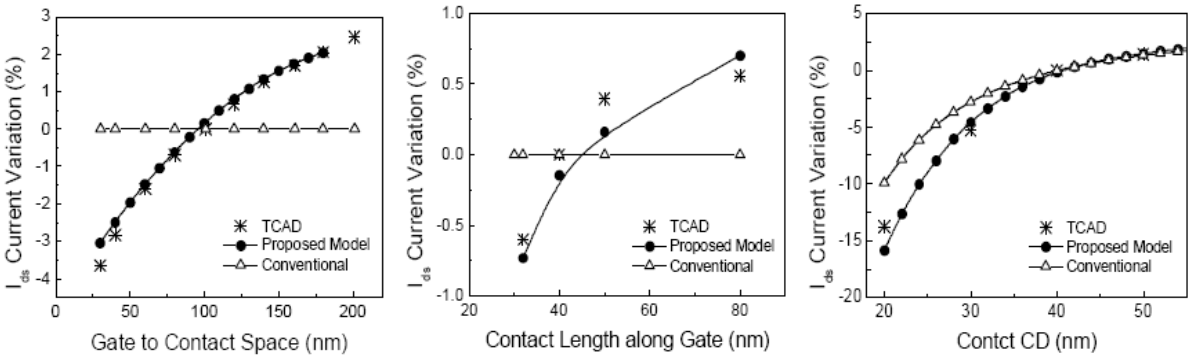

a) Contact Displacement b) Contact Space c) Contact area

Figure 2.24 Validation of our compact S/D contact extraction model. (a) Contact displacement, (b) contact shape, and (c) contact area.[130]

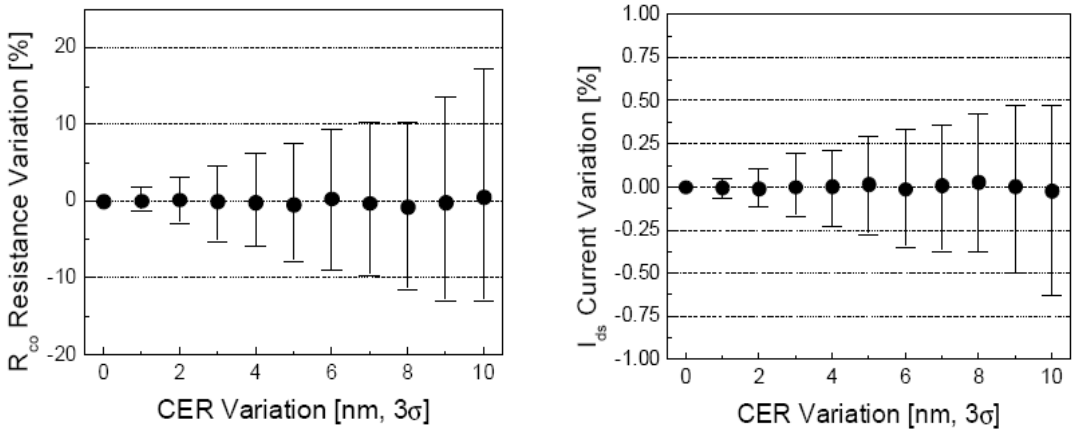

a) b)

Figure 2.25 The impact of CER on the contact resistance and the saturation current when the area variation of the S/D contact is the only factor of the contact model in a conventional NMOS cell. (a) Variation of the S/D contact resistance. (b) Variation of the device saturation current.[130]

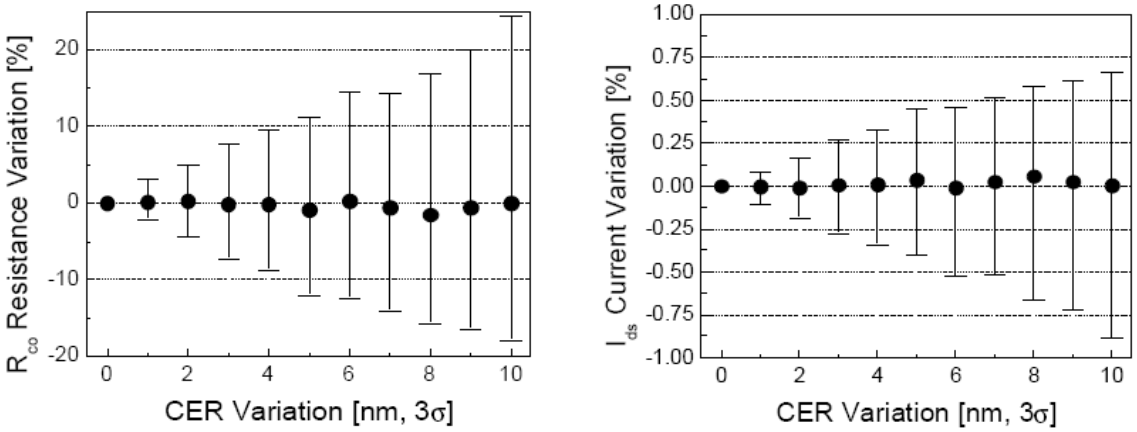

a) b)

Figure 2.26 The impact of CER on the contact resistance and the saturation current when the position, shape, and area weighting factors are considered in a stress-enhanced NMOS cell. (a) Variation of the S/D contact resistance. (b) Variation of the device saturation current.

Ban et al. validated the model by comparing the results with rigorous process/device simulation Technology Computer Aided Design (TCAD) and HSPICE simulation (conventional) [130]. In a conventional circuit simulation, the contact area is considered which is directly related to the contact resistance by dividing the contact resistivity by the contact area. Effects due to the device stress relaxation; it is limited to analyze the contact shape and distance. Figure 2.24 proves that the model proposed by Ban et al. matches very well with the TCAD results.

Figures 2.25 and 2.26 shows the results of the model for the conventional and stress enhanced NMOS cells. Thousands of CER patterns for a given rms value of CER are generated, and the mean values and the variations of the distribution of the calculated contact resistances and currents are calculated. The obtained mean value does not show significant differences but the variations are affected by the increase of rms value. For a stress-induced cell, the enhancement of variations is larger due to the more factors contributing to degradation. In the conventional NMOS cell, the variation of the S/D contact resistance and the saturation current reach up to 17.3% and 0.64%, respectively, when $3\sigma_{CER}$=10nm.

3. METROLOGY AND CHARACTERIZATION OF CONTACT EDGE ROUGHNESS AND CRITICAL DIMENSION UNIFORMITY

3.1. SEM metrology of contact holes

The metrology of contact holes has become very important in recent years in Lithography process. It is important that the contact holes should be inspected first, to see if they are properly etched and cleaned out and that they are fabricated in the proper dimensions. Apart from this, there is another growing concern in the lithography community over the Local Critical Dimension Uniformity (LCDU) of contact holes [133]. This is currently observed in the EUV lithography which is caused by the discrete nature of light and matter that is used to fabricate.

Characterization of Contact hole is also broadly used to evaluate the process to a given exposure. More over roughness on the side wall of the contact hole is a problem, which was reported by several groups earlier [130][132][135].

Initially, the metrology of the contact hole presented great difficulty to SEM. Because the electrons entering the contact holes had great difficulty while returning and achieving as signal. Researchers have attempted to develop methods for looking up into the contact holes. Using simulation, Babin et al [136] demonstrated the imaging of contact holes with high aspect ratio. The simulation involved high aspect ratio contact holes with and without defects. This contact holes with defects are of two types: a) under-etched layer at the bottom, and b) a particle defect at the bottom. At specific condition of pre-charge and imaging, the bottom of the contact hole is visible. These simulations are in good agreement with the experiment, and are used to optimize the SEM set up parameters for both the pre-charge and imaging. Postek et al [137] demonstrated that by applying a positive or negative bias to a sample or wafer, the collection of secondary electrons can be enhanced or reduced from contact holes. Sample biasing cannot be easily achieved where the large samples or wafer transfer instrumentation is concerned. Field control is the technique implemented to influence the collection of the electrons leaving the contact hole (see Figure 3.1). Mizuno et al. [138] used high accelerating voltage to reach the Secondary electron detector in order to view the holes and avoid absorption at the photo-resist level. Alternatively, Monahan et al. [139] used the technique where the backscattered electron signal can be used to image the bottom of the contact holes (see Figure 3.2). This was accomplished by using two Micro-Channel Plates (MCP), one with wide angle and another with narrow angle of collection. The one with wide angle is used to collect the electron from the top of the specimen and the one with the narrow angle is used to collect the electron from the bottom of the specimen.

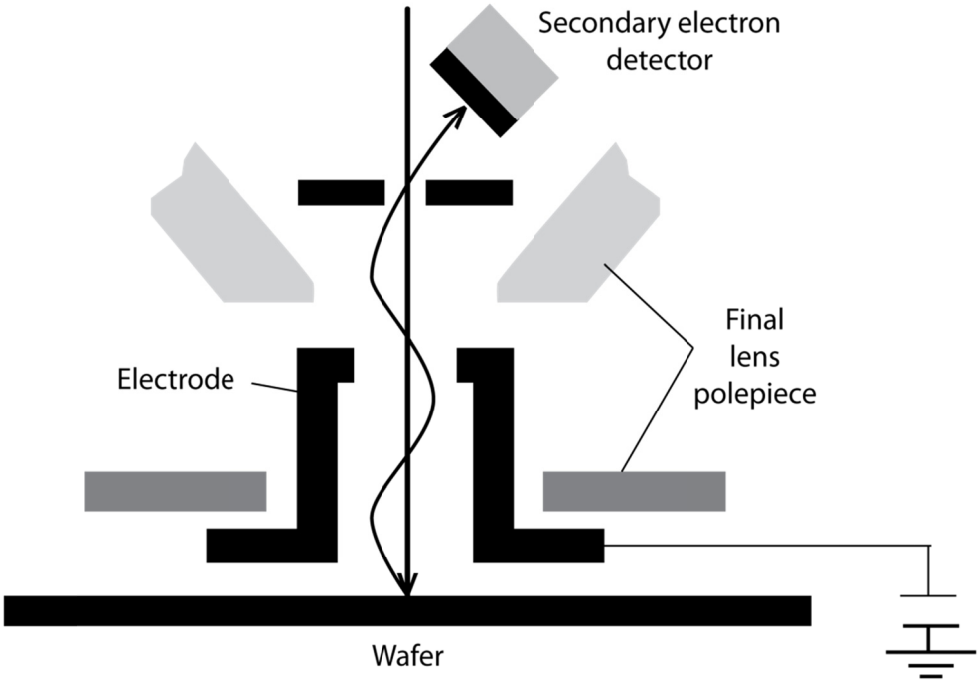

Figure 3.1 Drawing describing the field control concept

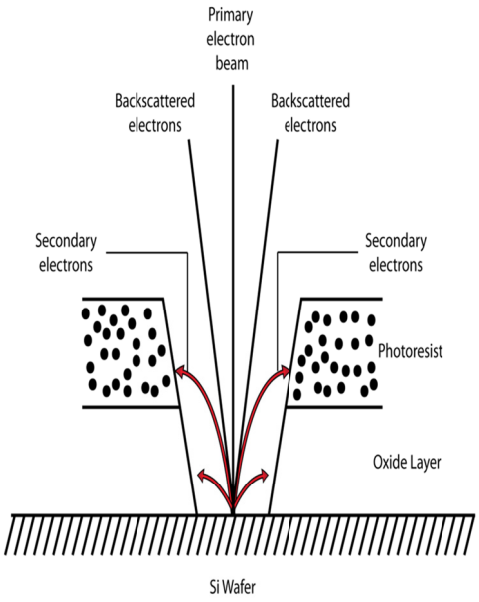

Figure 3.2 Drawing showing a contact hole and the problem with electron collection

3.2. Measurement and characterization of CER and LCDU with CD-SEM

3.2.1. Previous works

3.2.1.1 CER

As we show in the previous chapter, CER can cause a) time dependent dielectric breakdown (TDDB) due to the reduction of the space between contact and gate in the transistor and b) variation in the source drain (S/D) contact resistance and saturation current which is enhanced in strain-induced devices. In literature, depending on the degradation effect, two metrological approaches have been proposed. Both are based on the analysis of high resolution top down CD-SEM images like LER characterization.

TDDB is caused by the enhanced electric field concentration at the protrusions of the contact edge and their reduced distance with the transistor gate. The concentration increases with the sharpness and height of the protrusions (usually called spokes) and thus a proper CER characterization scheme should take into account these parameters. In the first works on CER, the intensity of these protrusions was characterized by the rms value and the correlation length. Recently, Momonoi et al. [132] proposed a characterization methodology which takes these into account expressively. This methodology consists of the following steps:

1 Find the maximum of the radiuses $r(\theta_i)$, $r_{max}(\theta_i)$, in each contact edge and define the corresponding spoke.

2 Calculate the height and the sharpness of the spoke (see Figure 3.3). The height is given by the difference $\Delta r_{max}=r_{max}-R$ and the sharpness is defined by the angle θ_m defined as:

$$\tan(\theta_m/2)=\frac{R\sin(\varphi_{ac})}{R(1-\cos(\varphi_{ac}))+\Delta r_{\max}}$$

where R is the radius of the best fitted circle and φ_{ac} the half of the epicentric angle measuring the opening of the spoke. Thus, in this approach the CER of each hole is actually characterized by the parameters Δr_{max}, θ_m.

3 Based on these CER spoke parameters, the electric field Emax at the tip of the spoke can be calculated through a modeling proposed by Momonoi et al. and compared with the maximum electric field strength at the point on the circumference when the hole has no roughness. According to the interconnect LER evaluation results (see PART 1 in this chapter), TDDB occurs when the ratio E_{max}/E_o becomes larger than 2. Therefore, the holes whose height and sharpness lead to $E_{max}/E_o>2$ can be considered "at risk".

Following the above methodology, through top-down SEM images of the contact holes on a wafer, one can determine the number of holes with risk spikes on the wafer and evaluate the used lithographic conditions with respect to this feature. Indeed, Momonoi et al[132]. have tested the sensitivity of these metrics to process variation by measuring the number of holes "at risk" for various focus conditions. They showed that for circular hole patterns the spoke metrics exhibited more sensitivity to the deviations from the optimal focus than the traditional $3\sigma_{CER}$ value. In elliptical patterns, both metrics showed sensitivity and this result was attributed by the authors to the fact that elliptical patterns are more sensitive to lithographic processes than circular ones.

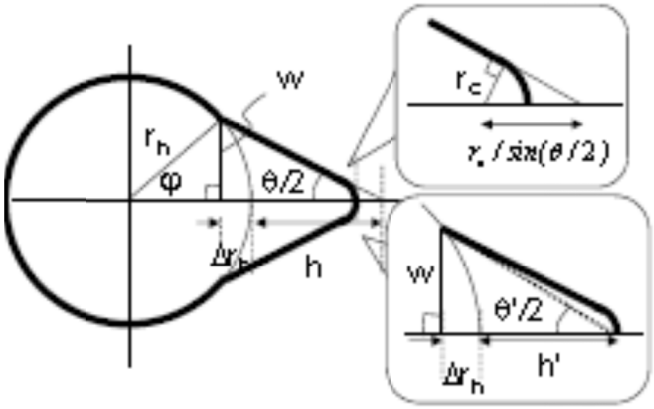

Figure 3.3 Spoke parameters used in CER modeling for TDDB effects [132]

The second method for characterizing CER, applied to S/D saturation current effects, is by using three parameters method which earlier used for characterization of the LER. The parameters used to characterize the CER in this method are RMS, correlation length and Roughness exponent. The spatial frequency of CER is studied by Power spectrum and HHCF [140]. Details of this characterization technique explained in section 3.6.

3.2.1.2 LCDU

There are various scales of variability of contact features we can consider in the fabrication process. First, we can study the variability of the diameters (CD) of the contacts included in a single CD-SEM image. At gradually larger scales there is the variability of the images taken within a die, then of the dies in a wafer, between the wafers of a lot and finally between the lots in a factory. In this chapter we focus on the variability of contacts included in a CD-SEM image (Local Critical Dimension non-Uniformity)0 while for the sake of comparison we will also calculate the variability at die level.

LCDU is usually quantified and calculated by the CD variation i.e. the standard deviation σ (sigma or rms value) of the CD values (mean diameters) of the contacts included in a single CD-SEM image. Some authors prefer to calculate and show the 3*sigma value to quantify CDU, while usually averages over a number of images are presented. Despite the simplicity of the definition, no well-established and widely accepted protocol for CDU measurement is in use. Thus there is no consensus about the number of contacts which should be included in an image or how many images should be acquired to provide a precise LCDU measurement. Therefore confusion and misleading results may be obtained when different experiments with different metrological decisions are compared.

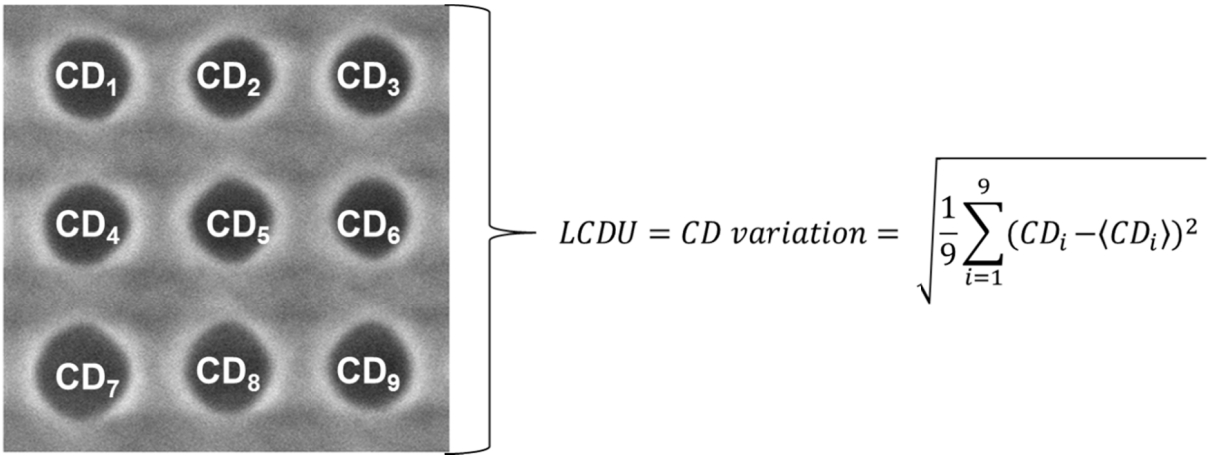

Figure 3.4 Example of a top-down CD-SEM image with 9 contact holes and the formula used for LCDU estimation (1 sigma value)

3.2.2. Our approach: CERDEMO software with emphasis on frequency and scaling analysis

Our approach follows the current trend according to which the evaluation of CER is based on the analysis of top-down SEM images of the contact pattern under inspection similarly to the main trend in LER metrology (see section 2.3) [130][132][135]0[142][143][144]. The schematic diagram shown in Figure 3.5 elaborates the steps followed in this advance methodology. Initially, the wafers are captured with required top-down SEM images, which contain more than one contact holes with respect to the applied magnification. In this image, noise smoothing filter is applied in order to remove the image noise present in it. After that using the Otsu's method [145]0, threshold is obtained and then the inner edges of the contact holes are detected. The output of that step is the Cartesian coordinates of the edge points of each contact hole. The best fitted circle to these points is defined and the coordinates of the center and the radius are obtained. Based on these, we transform the Cartesian to polar coordinates and we obtain the radii $r(\theta_j)$ of all contact edges of all images. However, these radii are not equally spaced in angle, i.e. the angle increment $\delta\theta_j=\theta_j+1-\theta_j$ depends on j, and this prevents the straightforward calculation of PS since the definition of Fourier Transform requires uniformly spaced data [147]. A simple way to

overcome this issue is to apply interpolation techniques to generate new radii defined at equally spaced angles [148] whose number can be fixed for all contact holes. The radii of all contact holes included in the k-th image can be stored in a 2D matrix A(k) whose rows contain the radii of each contact hole in the image, i.e. $A_{ij}(k)= r_i(\theta_j)$ with i=1,..,M and j=1,..,N , where M is the number of contact holes in the k-th image and N the number of equally spaced edge points after interpolation. This representation is similar to that used in LER[149]. The final step of the evaluation methodology is the calculation of CER metrics from the matrices A(k) of all images. This is made at three levels. In the first level, we calculate the CD, RMS, HHCF and PS of each contact edge with the following formulae:

$$CD_i^{(k)} = 2R_i^{(k)}$$

$$RMS_i^{(k)} = \sqrt{\frac{1}{N}\sum_{j=1}^{N}\left(r_i^{(k)}(\theta_j) - R_i^{(k)}\right)^2}$$

$$G_i^{(k)}(d_m) = \sqrt{\frac{1}{N-m}\sum_{j=1}^{N-m}\left(r\left(\theta_j\right) - r\left(\theta_{j+m}\right)\right)^2}$$

$$PS_i^{(k)}(f) = \frac{1}{\frac{N}{2}}\left|\sum_{j=1}^{\frac{N}{2}} r(\theta_i)e^{-jf\left(\frac{2\pi i}{N}\right)}\right|^2$$

where Ri(k) is the radius of the circle fitted to the i-th contact of k-th image and dm is the chord distance between the angles θj and θj+m defined by $d_j = 2R * \sin\left(\frac{\left|\theta_{i+j} - \theta_i\right|}{2}\right)$. Notice that due to the cyclic character of angle, the chord distance d has been proposed as independent variable in the definition of HHCF [74] [80].

From the slope of HHCF at small d, we estimate the roughness exponent $\alpha_i^{(k)}$ while the correlation length $\xi_i^{(k)}$ is given by

$$G_i^{(k)}\left(\xi_i^{(k)}\right) = \sqrt{2\left(1-\frac{1}{e}\right)}RMS_i^{(k)}$$

In the second level, we calculate the averages of the above quantities over all contact edges included in the specific image and finally we average the outputs over all available images and get the final values for the CER parameters and functions

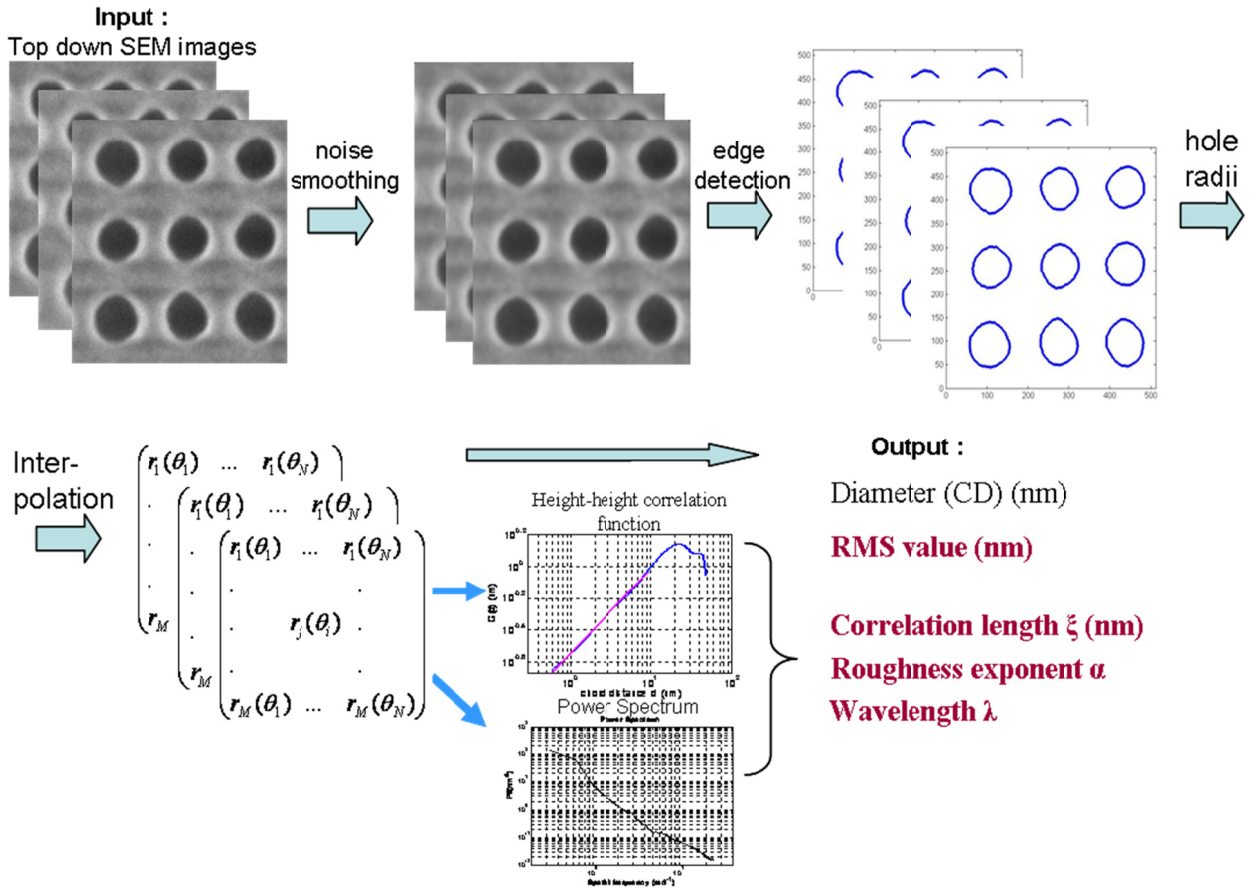

Figure 3.5.Schematic flow diagram of CER evaluation methodology as implemented in software "CERDEMO" which has been developed by our group. It starts with top-down SEM images and outputs CER and dimensional parameters and functions taking into account the circular form of contact edges and its implications

Attention should be paid on the estimation of the CD variation which quantifies the CD uniformity. In this paper, this is quantified as the average over all images of the standard deviations of the CDs of the contacts in each image, i.e. we consider the local CD variations averaged over all available images:

$$CD\ Variation = \frac{1}{K}\sum_{k=1}^{K}\left(\sqrt{\frac{1}{M}\sum_{i=1}^{M}\left(CD_i^{(k)} - CD^{(k)}\right)^2}\right)$$

with $CD_i^{(k)}$ the average of $CD_i^{(k)}$ over all contact edges in k-th image. The above methodology has been implemented in the home-made software CERDEMO.

3.3. METROLOGICAL APPLICATIONS

We have applied this evaluation methodology to the estimation of the CER of real contact holes fabricated on a 193 nm resist with EUV lithography. The nominal CD of the holes was 50 nm. We analyzed 25 CD-SEM images from the same sample with 9 holes per image acquired by a Hitachi CG4000 CD-SEM. The resolution of this CD-SEM is 1.8 nm. Both fabrication of the images and acquisition of the images were done in IMEC, Belgium. The obtained SEM images were analysed with CERDEMO software. The standard noise smoothing filter of the images was a median filter with window size S = 4 nm.

3.3.1. Frequency/scaling analysis and comparison with LER

Typical PS and HHCF of CER estimated by the above evaluation method are shown in Figure. 3.6.a and 3.6.b respectively. For the sake of comparison, Figure 3.6.c and 3.6.d illustrate typical examples of the PS and HHCF of LER. Although at middle and high frequencies, a power law decrease is observed in the PS of both CER and LER, a striking difference can be noticed at low frequencies. Instead of the saturation exhibited in the PS of LER, the PS of CER continues to elevate to higher values indicating the dominant contribution of low frequency fluctuations to CER. In HHCF, this contribution is manifested in the decrease and oscillations at high chord distances. On the contrary, the HHCF of LER saturates to a fixed value at high distances (see Figure. 3.6 d). This difference reflects the presence of low frequency fluctuations of the edge around the perfect circle and their minima give the dominant wavelengths. When the minimum lies at the largest d (the contact hole diameter), the contact edge fluctuations exhibit an almost periodicity with a period equal to the diameter.

This means that the edge is elongated and closer to an ellipse (see curve 1 and the corresponding edge in Figure 3.7). If it lies at smaller d, the hole may have a strong triangular or rhomb-like component in its shape (curve 2 in Figure 3.7). Otherwise, the edge may not have low frequency undulations and the HHCF saturates to the value $\sqrt{CER}$ (curve 3 in Figure 3.7). Thus, in CER, HHCF should be defined vs. the chord distance d and its behaviour at high d carries information about the overall shape of the hole.

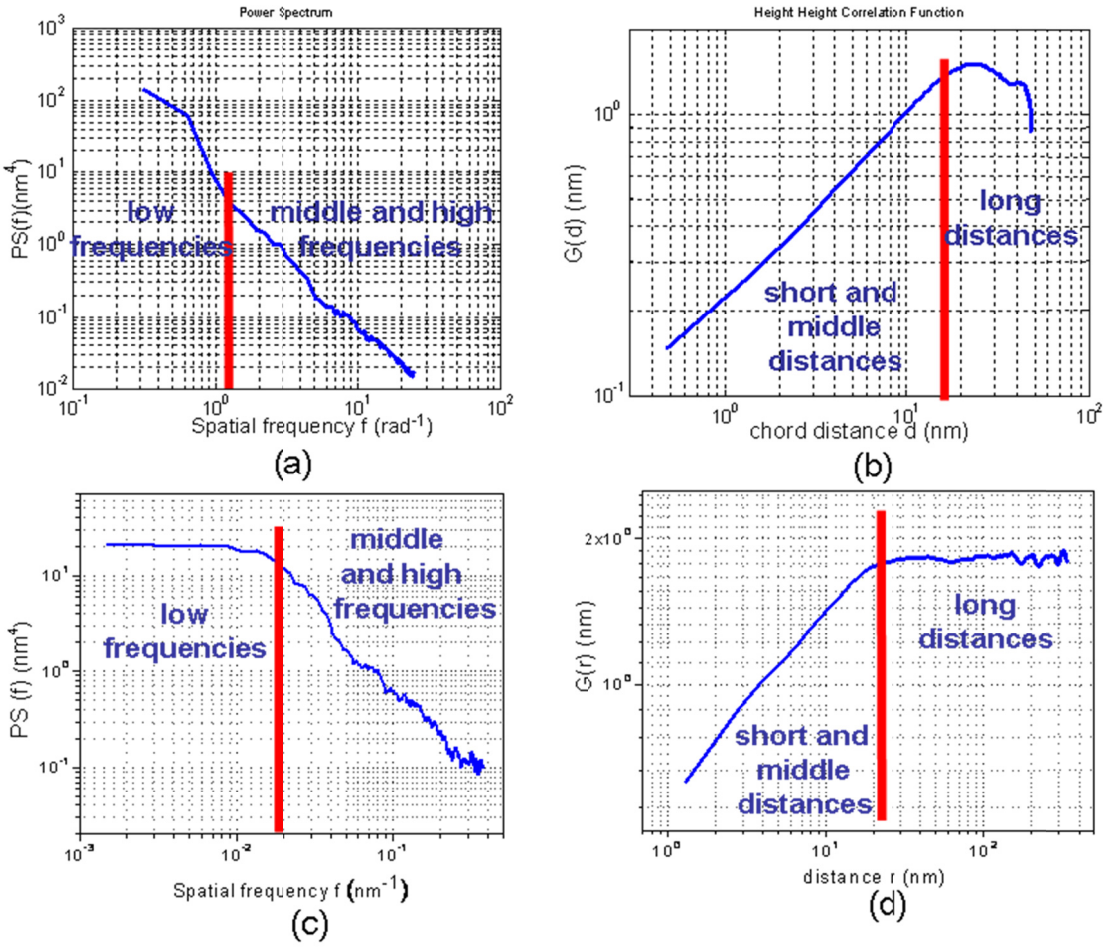

Figure 3.6.Power spectrum PS (a) and height-height correlation function G(d) (b) of the CER averaged over the 25 analyzed images (see text for details). Notice the dominant contribution of low frequency undulations of contact edges. For comparison, we show typical examples of PS and HHCF of LER calculated from CD-SEM images of 193nm resist lines with nominal CD=50nm (c and d respectively) where a saturation at low frequencies and long distances can be noticed respectively.

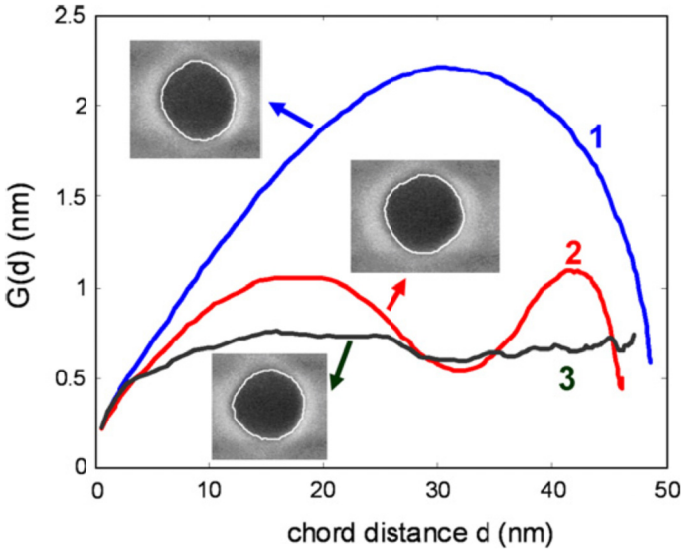

Figure 3.7 The height-height correlation function G(d) of three contact edges which are shown as insets. Notice the effects of the low-frequency deformations of the circular shape of the holes on the behavior of HHCF at large d.

In addition to the above described difference between CER and LER regarding their frequency and scaling behavior, one can refer to two further differences coming from the difference in the reference smooth line used in the definitions of LER and CER. In LER/LWR, the reference is a straight line whereas in CER it is a circle or an ellipse. This difference in the reference line has some effects on CER vs. LER/LWR metrology and characterization:

a) The first effect concerns the impact of the circular form of contact edges on the characterization of the spatial aspects of CER. In the literature, a contact edge is usually described by the radii $r(\theta_i)$ measured at the angles θ_i, i=1,N. However, the angle is not a well-defined variable for the characterization of the spatial aspects of CER since edge points with large angle differences may be close in space (see Figure 3.8).

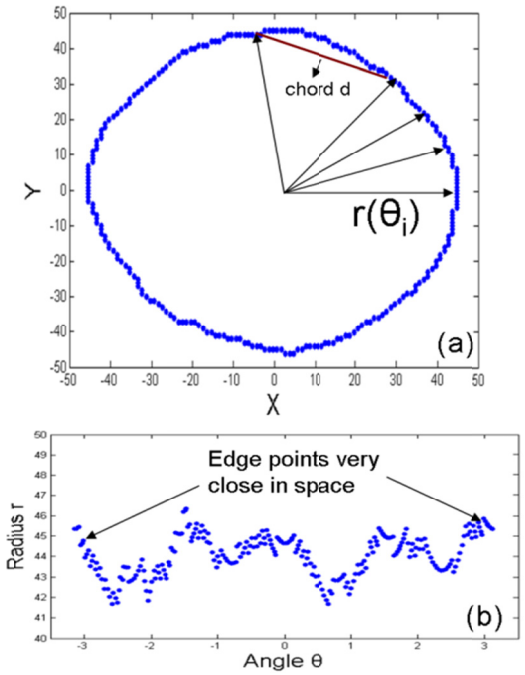

Figure 3.8 The edge points of a contact hole in Cartesian (a) and polar (b) coordinates. Notice that two edge points may have large angle differences but be close in space.

b) Second, in the measurement and characterization of LWR, the width of the resist line (CD value) and the line length included in the measurement process are independent quantities. On the contrary, in CER the largest distance of the contact edge points used in the measurement equals to the diameter of the contact hole, i.e. the CD value. This means that the shrinking of contact hole dimensions leads inevitably to measurement of CER using edge points which lie closer and consequently are more correlated.

3.3.2. Effects of measurement process parameters on CER and Contact hole CD variation

The acquisition of top-down SEM images involves the tuning of several SEM parameters like FoV, Symmetric Image, noise smoothing filter, number of frames per image, pixels etc as explained in section 3.3. One of the most important parameter is the size of the FoV, which defines the magnification of the sample shown in the image along with its pixel size. Furthermore, as shown

in the description of CER characterization process section 3.6, after getting the images, we apply a noise filter to smooth out the noise and enable to detect the contact edges. The size of the image area on which this filter applies is expected to affect the CER parameters. The aim of this sub-section is to examine the effects of both image magnification and noise smoothing on CER parameters and frequency spectrum. To this end, two sets of 25 SEM images taken from the same wafer with different FoV sizes are analyzed. The wafer contains contact holes fabricated on a 193nm resist with nominal CD=50nm. In the first set in Figure 3.9a, each image contains 25 holes and the image field is 450nm. The second set has images with 9 contact holes and field size 270nm shown in Figure 3.9b. Since all images have 512x512 pixels, the pixel size is 0.89nm (low magnification) and 0.53nm (high magnification) respectively. Both sets have been analyzed with a median noise filter applying to square window with variable side S.

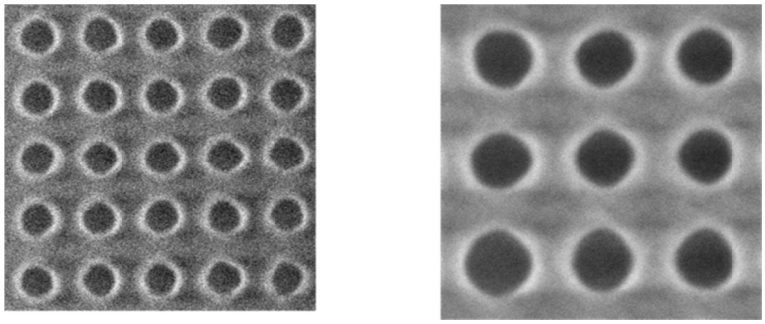

a) b)

Figure 3.9 Examples of low (a) and high (b) magnification top-down SEM images used in the CER evaluation methodologies.

For each magnification and noise smoothing parameter S the values of CD, rms and correlation length ξ are obtained after averaging over all holes and images. The roughness exponent α is not well-defined since the power law increase of G(r) is violated for many choices of noise parameter S in both magnifications.

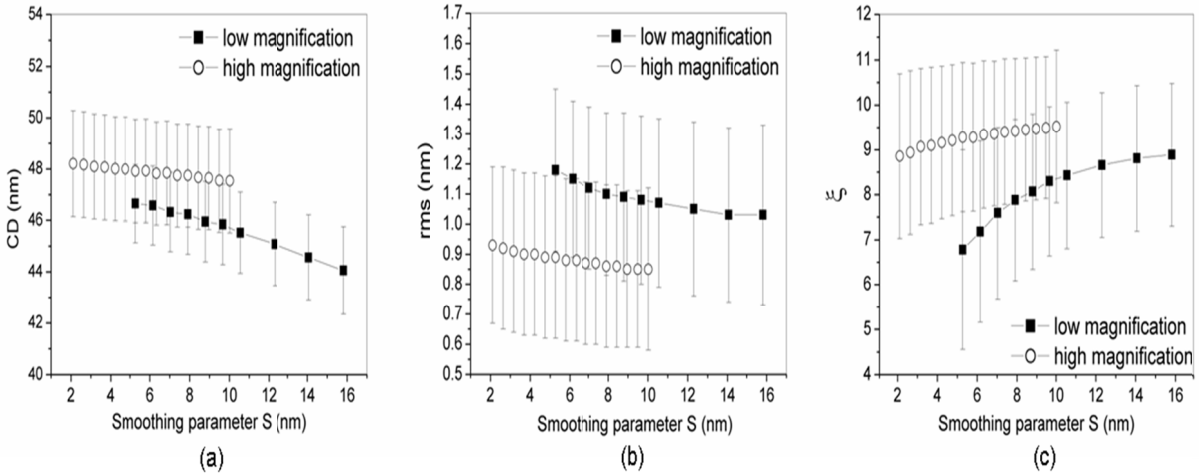

Figure 3.10.Average contact diameter (CD) (a), rms value σ_{CER} (b) and correlation length ξ (c) versus noise smoothing parameter S for the sets of images with low (full squares) and high (open circles) magnification. The error bars show the local (image-scale) standard deviations averaged over all images.

The results are illustrated in Figure 3.10 The shown error bars correspond to the mean of local standard deviations of CD and CER parameters calculated within images. The first output is that the images with high magnification (HM) have higher CD and correlation length ξ and lower rms value σCER for all noise smoothing parameters. In order to understand better these results, we analyze the frequency content of CER in both magnifications. Figure 3.11 shows the average PS of the low and high magnification images when the noise smoothing parameter S=8nm. Not surprisingly, the contribution of HM images is stronger at high frequencies. However, in a wide range of middle frequencies the order is inversed and the frequency content of low magnification (LM) images gets higher values. This inverse and superiority of the PS of LM versus HM images seems to explain the increased rms of LM images. At very low frequency, the HM spectrum crosses again the LM one and becomes higher than it. This increase may be responsible for the larger correlation length found in HM CER. Figure 3.10 shows also the effects of noise smoothing parameter S on CER metrics. For both magnifications the results are in agreement with expectations: enlarged noise smoothing causes decrease of CD and σCER and increase of ξ.

Furthermore, the HM images are found to be less sensitive to noise smoothing than LM ones.

Finally, we compare the effects of image magnification and noise smoothing with the error bars in Figure 3.10 coming from the local variations of CER parameters. The comparison is quantified in Table 3, where the third row includes the differences between the CD and CER parameters of two magnifications for S=8nm and the fourth difference of the minimum from the maximum value of parameters of the HM images for the whole range of noise filter parameter S. For the analyzed images in this work, it seems that the local variations have marginally stronger contribution to the uncertainty of CD and CER parameters than image magnification, while noise smoothing process is much less effective.

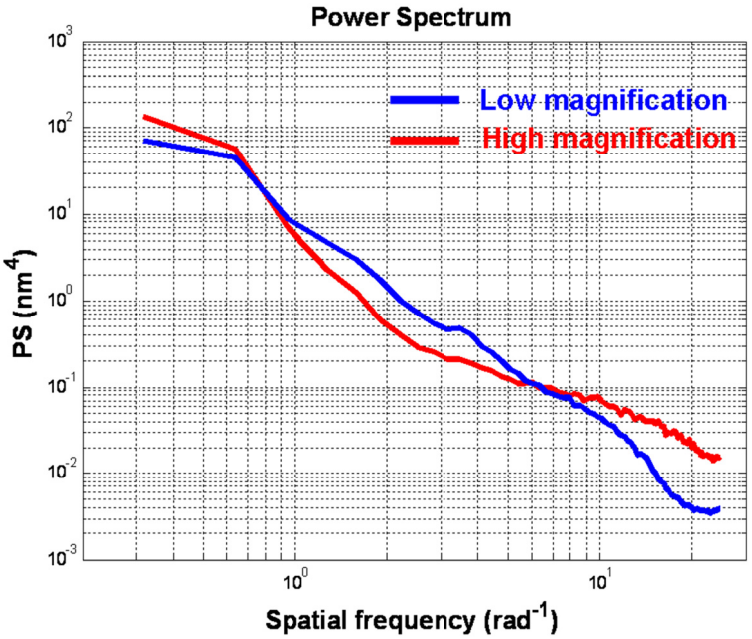

Figure 3.11.Average power spectrum of the low and high magnification sets of SEM images for smoothing parameter S=8nm. Notice the frequency dependent relation between two magnification spectra.

3.3.3. Local vs. Global (die) level uncertainties of CD and CER parameters

In the evaluation of the CER induced by a process on a film, the input CD-SEM images are usually taken from different positions on the wafer under inspection. Also, each image may contain several holes. Thus, we can define two variability levels of CER parameters. The first refers to the standard deviation of CER parameters among the holes in a single image (image-scale or local uncertainty) and the second is the uncertainty among the mean CER parameters of different images (wafer-scale or global uncertainty). We can assess the contribution of these two scales of uncertainties by using the results of the CER evaluation of the 25 SEM images described in the previous section. Table 3 contains the local (image-scale) and global (wafer-scale) uncertainties of the hole diameter (CD), rms value σ_{CER} and correlation length ξ. The local uncertainties are the mean value of the standard deviations of CER parameters calculated over the holes of each image, while the global ones are the standard deviations of the mean CER parameters of images.

Quite surprisingly, the results of this CER evaluation methodology show that the local variations have stronger effects on CER parameters than global ones. This conclusion has also been reached when different magnifications and noise filters have been used in the CER characterization process.

Uncertainty	CD (nm)	σ_{CER} (nm)	ξ (nm)
Local (image-scale) variations	2.05	0.26	1.74
Global (wafer-scale) variations	1.02	0.12	0.74
Image magnification effects (S=8nm)	1.52	0.24	1.56
Noise smoothing effects (HM images)	0.87	0.08	0.64

Table 3 Contributions to the uncertainties of CD, rms value σ_{CER} and correlation length ξ of process (local and global) and image effects

4. EUVL PROCESS AND MATERIAL EFFECTS ON CER AND CDU

The presence of roughness in the components of a device usually raises three interrelated issues. The first is its metrology and characterization and when focused on the sidewall roughness of contact holes and its measurement with SEM was the subject of the previous Chapter 3. There is an advanced measurement and characterization methodology of CER and CDU, which starts from the top-down SEM images of contact hole patterns and the detection of their edges and results in the estimation of local and global CDU measures (CD variances) and CER metrics such as RMS, correlation length, fractal exponent, power spectrum and HHCF was developed and presented. Using this methodology, the differences of CER with LER coming from their different topologies as well as the effects of image magnification and noise smoothing parameters was explored. The second issue is the identification of the origins of roughness formation during the fabrication of the features which can be done both by experimental and modeling/simulation studies. In this chapter we deal with some aspects of this issue analyzing experimental results. The fabrication of device features involves both process conditions and material properties. In lithography, the process conditions may be the illumination parameters, exposure dose, focus, baking temperatures and times, development time and

solvent etc. The material (resist) contributes through its structure and physicochemical properties and the nature and concentration of the additive ingredients such as PAG, quencher and sensitizers. Here, we will focus on the effects of dose, PAG, quencher and sensitizer concentration for fixed resist formulation. A generic and abstractive modeling approach of CDU/CER formation is presented and discussed in the next chapter 5. The third issue which actually weighs the motivation of roughness studies is the roughness effects on device performance and yield. We are not going to investigate this issue in this thesis, although some hints have been given in the section 2.4 of the previous chapter.

4.1. Previous works

Recent experimental studies have investigated the effects of illumination conditions, mask, exposure dose, resist tone, Post Exposure Bake, size of protective group, acid diffusion length, film thickness and post-litho treatments (rinse, solvent vaporization and hard mask etching) on CDU. The reported trends are summarized in Table 4 0[151][152][153]. Almost all dependencies are in harmony with the trade-off between CDU and sensitivity degradation making resist slower. Regarding CER, in a preliminary work, the impact of numerical aperture, bake temperature and mask CD on CER RMS was studied [144] and the results are also shown in Table 4. These trends are explained briefly as follows:

Illumination conditions: There are few illumination sources available out of which conventional and quasar illumination shapes are used in the fabrication of contact holes. Comparison of these two illumination source shapes have been done and found that quasar illumination condition gives less CDU than that in conventional illumination.

Focus: The aerial image quality steadily decreases with both positive and negative defocus. CD-SEM measurement indicates that CER and CDU values increase as the image moves out of focus 0.

Numerical Aperture (NA): It plays an important role in the Resolution and Depth of Focus. It has been measured that when there is an increase in NA then the CER decreases.

Mask: In 193nm lithography, the mask roughness is not a major contributor to resist LER since the high and medium frequency LER fluctuations are filtered out by the optical projection system. However, even in 193nm the effects of mask LER on Aerial Image Contrast (AIC) may be an issue and it has been studied in some papers.

In EUV lithography, in addition to mask roughness, the impact of mask multilayer surface should also be considered since defects in this multilayer surface will cause mismatch in the phase of the reflected illuminated beam. i.e., variation in the aerial image will lead to roughness in printed features. This variation in the aerial image will also cause variation in the size of the printed contact holes. Work has also been carried out to study the CD variation of the contact hole on the mask by area metrics [154]. The area metrics of the mask contact hole is the area of the contact in the mask. By finding the variation in the area, the mask contact hole variation is calculated. Work has also been carried out by changing the pitch and CD of the contact hole in mask. According to this works, when CD and pitch of the mask is increased the CD uniformity 0 and CER increases [144]. This might be due to the optical proximity effect.

Exposure Dose: In optical lithography, exposure dose is related to the number of photon impinging in the resist film per unit surface, and involves the notion of stochastic variation or shot-noise. Shot noise obeys Poisson statistics and therefore the dose fluctuation is proportional to $1/\sqrt{N}$, where N is the number of

photons incident upon a given resist area. Obviously, the importance of shot noise increases when N is small (highly sensitive resists, EUV lithography). Several experiments have shown that LER decreases with exposure dose. Similarly, recent experimental measurements show that increase in the exposure dose leads to drop down of LCDU whereas causes no changes (or slightly reduction) of CER [152].

Post Exposure bake (PEB): Increase in post exposure bake will lead to increase in acid diffusion length which leads to the increase in CER and CDU.

Post-process treatment: Usually, it is common to treat resist features after development (post-litho processing) to reduce LER/LWR. There are several methods to treat resist features after lithography, out of which 3 smoothening techniques have been implemented in the contact holes. These are Low Surface Tension (LST) rinse, Solvent Vaporization and Etch Treatment. All these techniques show a reduction in the CDU.

Resist tone: It is expected that using negative tone development (NTD) resists will result in better CDU than positive tone development (PTD).

Protective group: When compared to a standard resist, resist with a low activation energy (Ea) protective group will give good CDU of the contacts. i.e., increase in activation energy (Ea) protective group will increase in CDU of the contacts.

Film Thickness: Effects of Film Thickness also have been studied. Studies shows that decrease in thickness of the film will increase LCDU and this might be related to PAG segregation effects or changes in the glass transition temperature (Tg) of the resist film.

Acid diffusion length (ADL): PEB is the main process factor for varying acid diffusion length. To achieve the control of acid diffusion length, other factors include the size of catalytic acid molecules, glass transition temperature (Tg) of the matrix resin, and the residual solvent content. It is generally accepted and experimentally verified that for sufficiently large pitch, increase in acid diffusion length leads to the reduction in the LER/LWR reduction due to the smoothing of spatial dispersion of photochemical events caused by shot noise. However, similar to the PEB effects, it has been shown that for a very large diffusion length relative to the pitch, acid diffusion causes degraded chemical contrast and exposure latitude and consequently increased CDU. Lower PEB temperature decreased acid mobility and shortens the acid diffusion length leading to improved CDU.

However, to the best our knowledge, no study has been reported on the effects of the ingredients commonly used in EUV resist synthesis (PAG, sensitizer, quencher) which in LER/LWR have been shown to play an important role and several recent works were devoted to their investigation. In one of these, a similar resist to that used in this thesis was utilized and the effects of different exposure wavelengths (248nm, 193nm and EUV) and sensitizer loadings on acid kinetics, quantum yield and LWR were studied [155]. It was found that the increase in sensitizer loading in resist does not lead to quantum yield enhancement, which means that even for the lowest sensitizer concentration, secondary electrons are very efficient to activate PAG molecules and further increase in sensitizer does not result in higher acid yields. Nevertheless, the authors showed that increased sensitizer loadings cause higher acid diffusion length in a nonlinear fashion and used this increase to explain the reduction of sizing dose with sensitizer loading.

In this chapter, motivated by the recently rising demand for further understanding of CDU and CER dependencies on EUVL process conditions and resist components, we proceed to the experimental study of the effects of

exposure dose, PAG, sensitizer and quencher in an EUV resist and measure CDU and CER parameters using the methodology of the previous chapter 3. We are trying to explain the experimental results recalling the effects of photon shot noise (PSN) and PAG distribution statistics following similar argumentation in LER/LWR studies [155][156]. Furthermore, inspired by the PS analysis of contact edges, we discuss the implications of their circular topology (2D structure) in these dependencies and especially in CER.

		CDU	CER
Illumination conditions	Conventional/quasar	Quasar ↓	
	Numerical Aperture		↓
Mask	Critical Dimension	↓	↑
	Pitch	↓	
Process conditions	Dose	↓	↑
	PEB	↑	↑
	Post-litho treatments	↓	
Resist properties	Resist tone	Negative ↓	
	Protection group	↓	
	Film thickness	↓	
	Acid Diffusion Length	↑	

Table 4 Summary of the trends reported in recent literature about the effects of illumination, mask, process and resist on CDU (CD variation) and CER (RMS value).

The chapter is structured as follows: first, we give the details of the performed experiments and measurements in Section 4.2. The results of the experiments and their analysis and interpretation are presented in Sections 4.3 and 4.4 for CDU and CER dependencies, respectively. The chapter ends with a summary of the most important findings and the main points for their interpretation.

4.2. Experimental details

Experiments with two different EUV polymer bound PAG resists (A and B) have been performed. In the first resist A, we studied mainly the effects of exposure dose. Nevertheless, in the second resist B, six different combinations of PAG, sensitizer and quencher concentrations have been utilized to study the effect of

PAG, sensitizer and quencher loadings on CER and CDU for a range of exposure doses. These combinations in resist formulation are shown schematically in the Table 5 with ρ_{PAG}, $\rho_{sensitizer}$ and $\rho_{quencher}$ the reference PAG, sensitizer and quencher concentrations.

Resist	**PAG**	**Sensitizer**	**Quencher**
ST (Standard)	1 X ρ_{PAG}	1 X $\rho_{sensitizer}$	1X $\rho_{quencher}$
PAG-	0.5 X ρ_{PAG}	1 X $\rho_{sensitizer}$	1X $\rho_{quencher}$
PAG+	1.5 X ρ_{PAG}	1 X $\rho_{sensitizer}$	1X $\rho_{quencher}$
SEN-	1 X ρ_{PAG}	0.5 X $\rho_{sensitizer}$	1X $\rho_{quencher}$
SEN+	1 X ρ_{PAG}	1.5 X $\rho_{sensitizer}$	1X $\rho_{quencher}$
QNPAG+	1.5 X ρ_{PAG}	1 X $\rho_{sensitizer}$	1.5X $\rho_{quencher}$

Table 5 Different combinations of the concentrations of resist ingredients we use in the experiments

The exposures were executed on an ASML NXE:3100 EUV scanner at 0.25NA using conventional illumination. The obtained contact holes were imaged with top-down SEM pictures acquired by a Hitachi CG4000 CD-SEM. Each experimental point in the diagrams is actually an average over 5 or 6 top-down SEM images with 25 contact holes and size of 450X450 nm^2 per image. Examples of top-down CD-SEM images for all the combinations studied in this chapter for various doses are shown in the Figure 4.1. The presented results (CD, CD variation, RMS and correlation length ξ) are obtained from the in-house code CERDEMO which implements the methodology described in the previous Chapter 3.

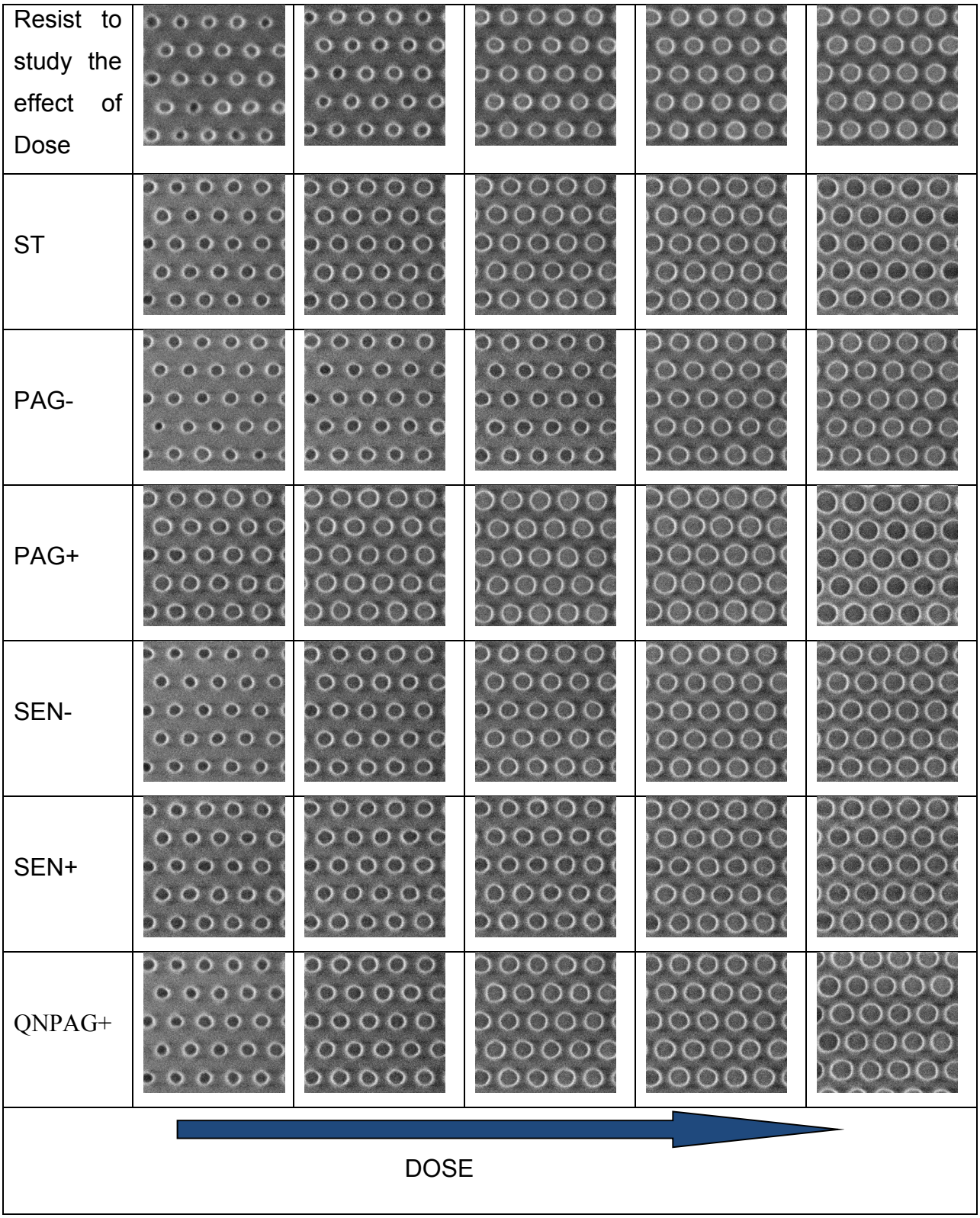

Figure 4.1 Representative top-down CD-SEM images of the contact patterns of the six formulations studied in this chapter versus dose.

4.3. Resist A: Effects of Exposure Dose on CD, CDU and CER

The advanced characterization methodology explained in the previous chapter has been applied to the evaluation of the CER and CD Variation (CDU) of contact holes fabricated in EUV resist that is exposed to different doses from 21.2mJ/cm^2 to 35.6mJ/cm^2. Figure 4.2 shows the collection of the results for the effects of dose on the dimensional and CER parameters and functions that are obtained from the in-house code CERDEMO [16] which implements the methodology described in the previous chapter. It reveals that when the exposure increases then: (a) contact CD increases almost linearly, (b) CD Variation decreases up to Jc~29 mJ/cm^2 and then almost saturates at a value slightly higher than 1nm, (c) RMS value increases almost linearly up to Jc and then saturates about ~1.15nm (3RMS~3.45nm) ,(d) correlation length ξ goes up constantly almost linearly, (e) roughness exponent α increases very slightly until Jc and then oscillates about ~0.69 and (f) PS shifts upwards especially for frequencies <1/ξ and furthermore the lowest limit of PS frequency range scales as ~1/CD and therefore it decreases with dose, since CD is proportional to dose. The first two results (increase of CD and reduction of CDV with dose) are expected and are in agreement with the similar behavior of LER. The result which is in striking difference to LER results is the decrease of RMS at low doses. In several experimental and theoretical works, it has been shown that due to photon and acid shot noise effects, the RMS of LER increases at low doses [157][158][159][160]. In fact, theoretical arguments have proposed the dependence RMS~(1/√dose) which has been verified by experimental measurements [161]. The possible origins of this opposite behavior of CER versus exposure-dose are discussed in below section 4.4 and chapter 5 along with some insights from modeling results.

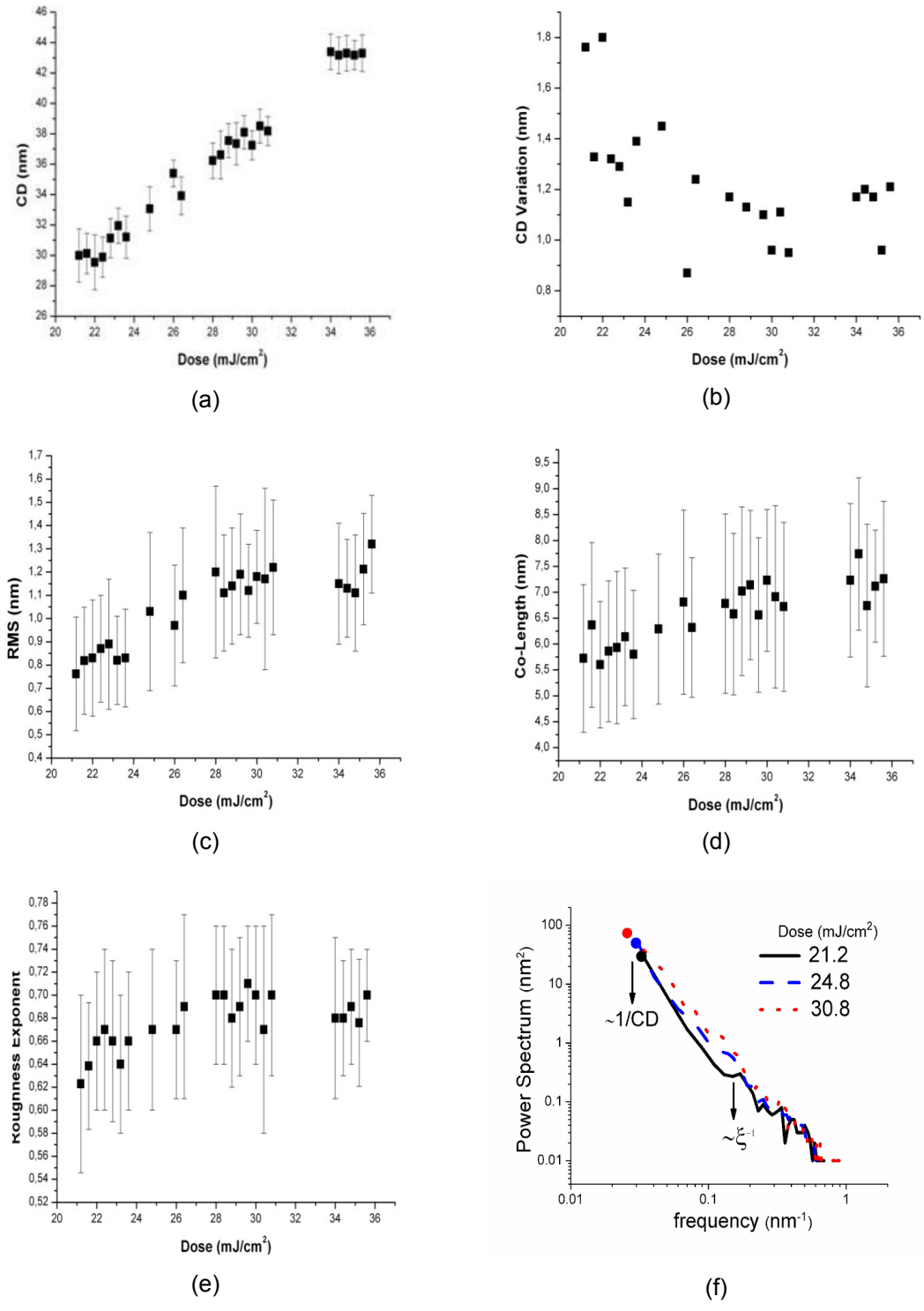

Figure 4.2 Effects of EUV dose on CD (a), CD Variation (uniformity) (b), RMS (c), correlation length (d), roughness exponent (e) and Power Spectrum (f).

4.4. Resist B: The role of dose, PAG, Sensitizer and Quencher

4.4.1. Effects on CD

Similarly to resist A behavior, Figure 4.3 shows that in all combinations of resist B the CD increases slightly sub-linearly with respect to exposure dose. The sub-linearity may be due to PAG depletion effects at high doses (i.e. quantum yield may decrease at high doses since less PAG molecules are available). At all doses, more PAG and sensitizer lead to wider holes (larger CD values) in a highly nonlinear fashion, which can be attributed to the nonlinear dependence of acid diffusion length on sensitizer loadings demonstrated in a similar system [155]. In QNPAG+ resist, when concentration of the quencher is increased from 1xρ quencher to1.5xρ quencher, it nullifies the effect of PAG and shows similar trend to the standard resist.

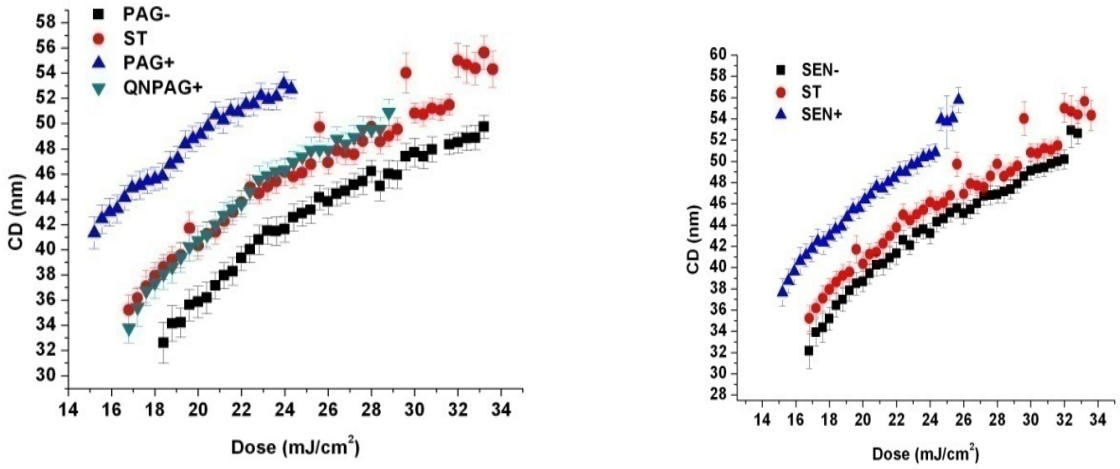

(a) (b)

Figure 4.3. (a) Effect of EUV dose on CD in EUV resist with three different PAG and quencher concentration and (b) Effect of EUV dose on CD in EUV resist with three different sensitizer concentration

4.4.2. Effects on CDU (CD Variation)

Regarding CD variation dependencies, the experimental data when plotted against dose are quite scattered with an overall decreasing trend up to dose

~22mJ/cm^2 and a saturation after that around ~0.9–1nm ($3\sigma_{CD}$~2.7–3.0nm) (see Figure 4.4 a and 4.4 c). This behavior seems to be in harmony with similar recent studies on contacts [152] and overall LER dependencies and can be attributed to the reduced shot noise effects when dose increases [157][159]. As shown by Gronheid et al. [155], acid generation and acid shot noise (ASN) are not affected by sensitizer loading and therefore at fixed doses no effect of sensitizer concentration on CDU is expected. Indeed, this is the result exhibited by the experimental data (see Figure 4.4 a). On the other hand, at fixed doses, a slightly reduced (increased) CD variation is observed at high concentrations of PAG (quencher) in agreement with LER behavior when no segregation effects take place [162][163][164] (Figure 4.4 c). Keeping the dose fixed means that the contribution of PSN to ASN remains unaltered and the latter is only affected by PAG and quencher concentration with more PAG (quencher) leading to higher (lower) acid generation and consequently less (more) ASN and smaller (higher) CDU.

If we plot the experimental data against the final CD value using the correspondence shown in Figure 4.3, a slight merging trend is observed although the points are still quite scattered. Figure 4.4 b and 4.4d shows that CD variation is reducing constantly until CD ~40–42nm and then oscillates randomly around ~0.9–1nm.

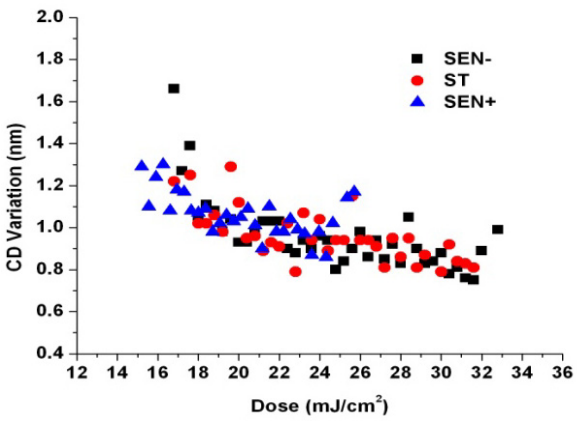

(a)

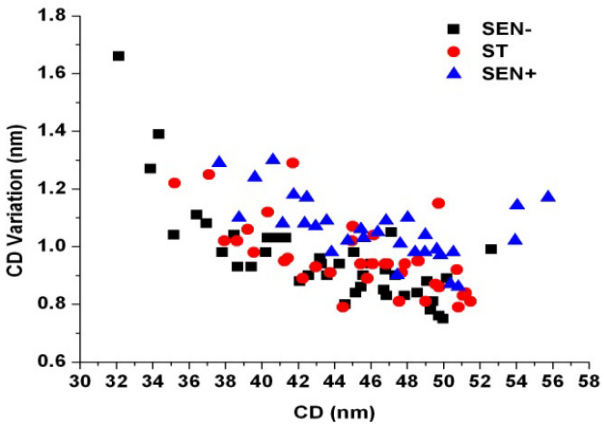

(b)

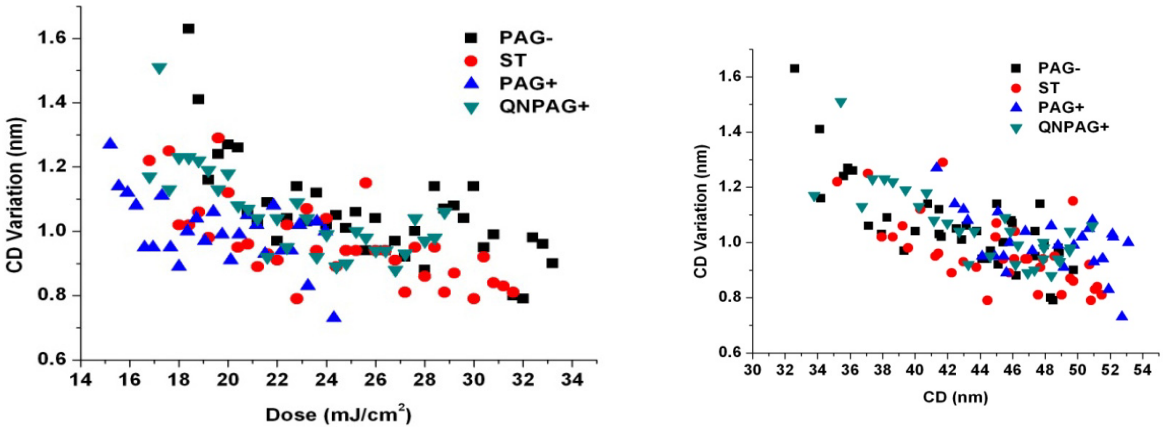

(c) (d)

Figure 4.4 CD variation versus dose (3a and 3c) and CD (3b and 3d) for all resist formulations with various PAG, quencher and sensitizer concentrations shown in Table 2.

In order to examine clearly the CDU dependencies on CD, we focus on a specific CD (~42nm) and plot in Figure 4.5a and 4.5b the effect of sensitizer, PAG and quencher on CD variation averaging over the experimental points with CD close to ~42nm. In the same diagram, we also show the required sizing doses to obtain this CD. From the bar diagram of Figure 4.5 a, it is evident that for fixed CD ~42nm, CD variation increases with ñ sensitizer, whereas dose decreases. Since no effect of sensitizer loading on ASN and CDU is expected, the increase in CDU can be directly linked to the drop of sizing dose and the subsequent rise of PSN. This link is clearly exhibited in Figure 4.5 c where a linear relationship between CD variation and 1/√dose and therefore the principal role of PSN in the dependence of CDU on sensitizer loading are demonstrated. A similar finding for LWR has also been reported by Gronheid et al [155]. Regarding PAG effects, it seems that CD variation takes the lower values for the standard PAG concentration ($1.0\times\rho_{PAG}$) contrary to the above mentioned trend at fixed doses. Given that the sizing dose is monotonically decreasing with PAG, one may argue that this behavior may be a result of the combined effect of the PSN which enhances with PAG and the contribution to ASN and CDU of the noise in the distribution of PAG molecules which is reducing with PAG concentration.

CD~42nm

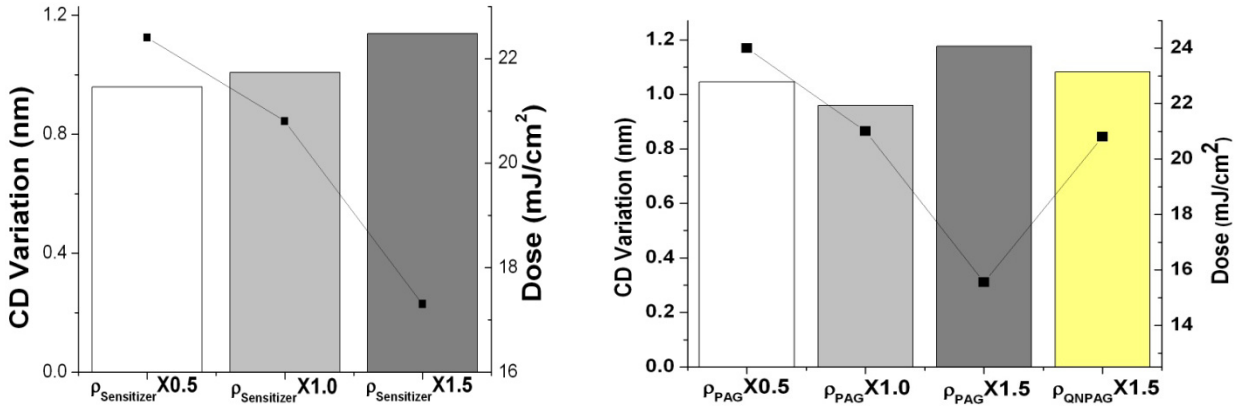

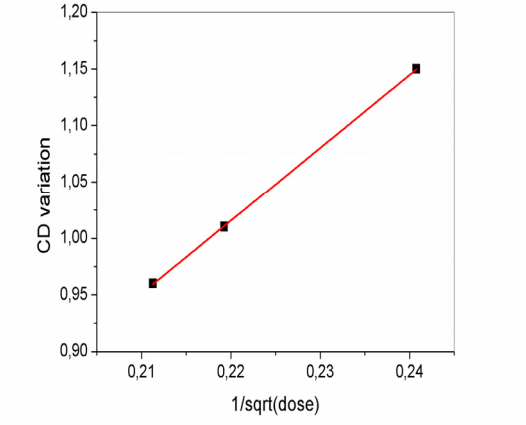

(c)

Figure 4.5 CD variations versus sensitizer (a) PAG and quencher (b) concentrations in the resist formulations used in the paper. The linear relationship of CD variation with 1/√dose for sensitizer dependencies is demonstrated in (c) revealing the dominance of PSN effects.

To obtain further understanding of this dependence, we can recall the argumentation by Anderson and Naulleau [156] about the LWR origins in EUV resists according to which there are two principal contributions to LWR: the PSN and the distribution statistics of PAG molecules. Which contribution dominates is determined by the ratio of the activated PAG molecules to their total number per pixel in resist bulk. If this ratio is small then LWR is mainly determined by PSN (scenario 1), whereas when almost all PAG molecules have been activated by the secondary electrons and the above ratio is close to 1, the PAG distribution

statistics plays the major role (scenario 2) (see Figure 4.6 for a schematic view of the tow scenario).

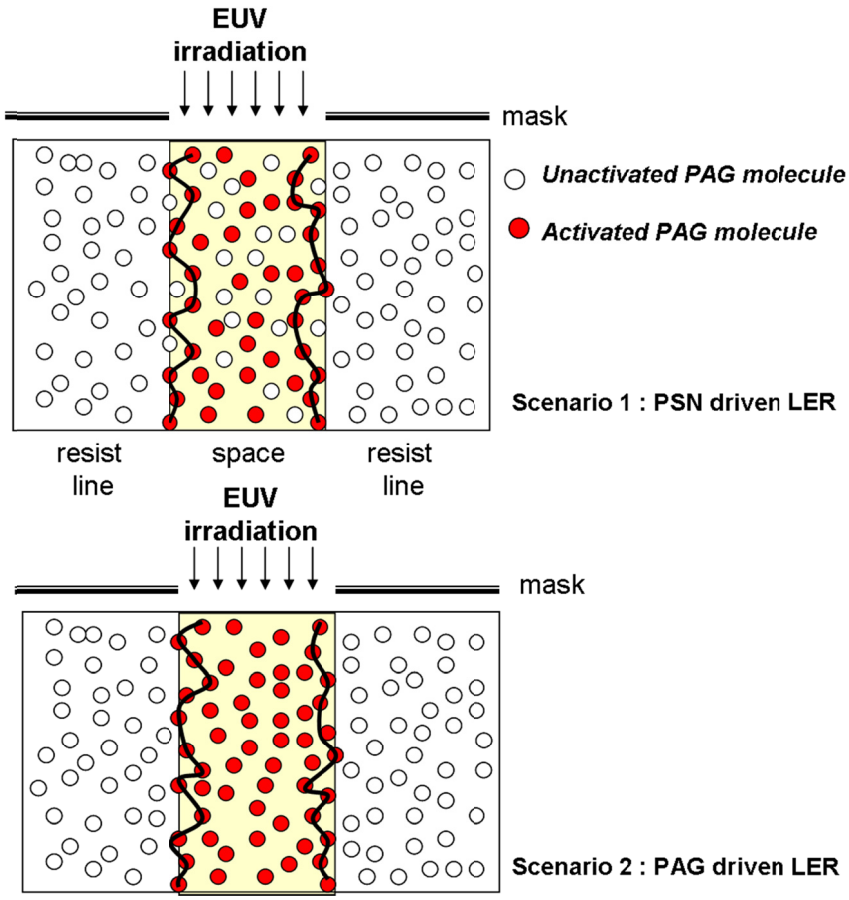

Figure 4.6 Schematic view of the two scenario proposed by Anderson and Naulleau [20] for the LER formation in EUV resists, where irradiated space area is shown with yellow background, inactivated PAG molecules with hollow circles and activated PAG molecules with red filled circles. Notice the role of PSN and PAG distribution statistics on LER formation.

As we referred in the end of Section 4.1, Gronheid et al [155] argued that in a similar system to the standard resist formulation (ST), all PAG molecules are activated by secondary electrons, which means that we are in the realm of scenario 2. For lower PAG concentrations (i.e. formulation PAG–), we still remain in scenario 2 and the CDU of contacts similar to LWR is determined by PAG statistics. This means that the observed increase of CDU at PAG– can be attributed to the enhanced noise of PAG distribution in resist associated to the reduced PAG concentration. On the other side, when the PAG loading goes to

1.5 times the standard one, it is reasonable to assume that the number of activated PAG molecules becomes smaller than their total number per pixel and therefore we move to scenario 1 where CDU is PSN determined. Therefore, given the reduction of required sizing dose at PAG+, the increase in CDU may be attributed to the enhanced PSN.

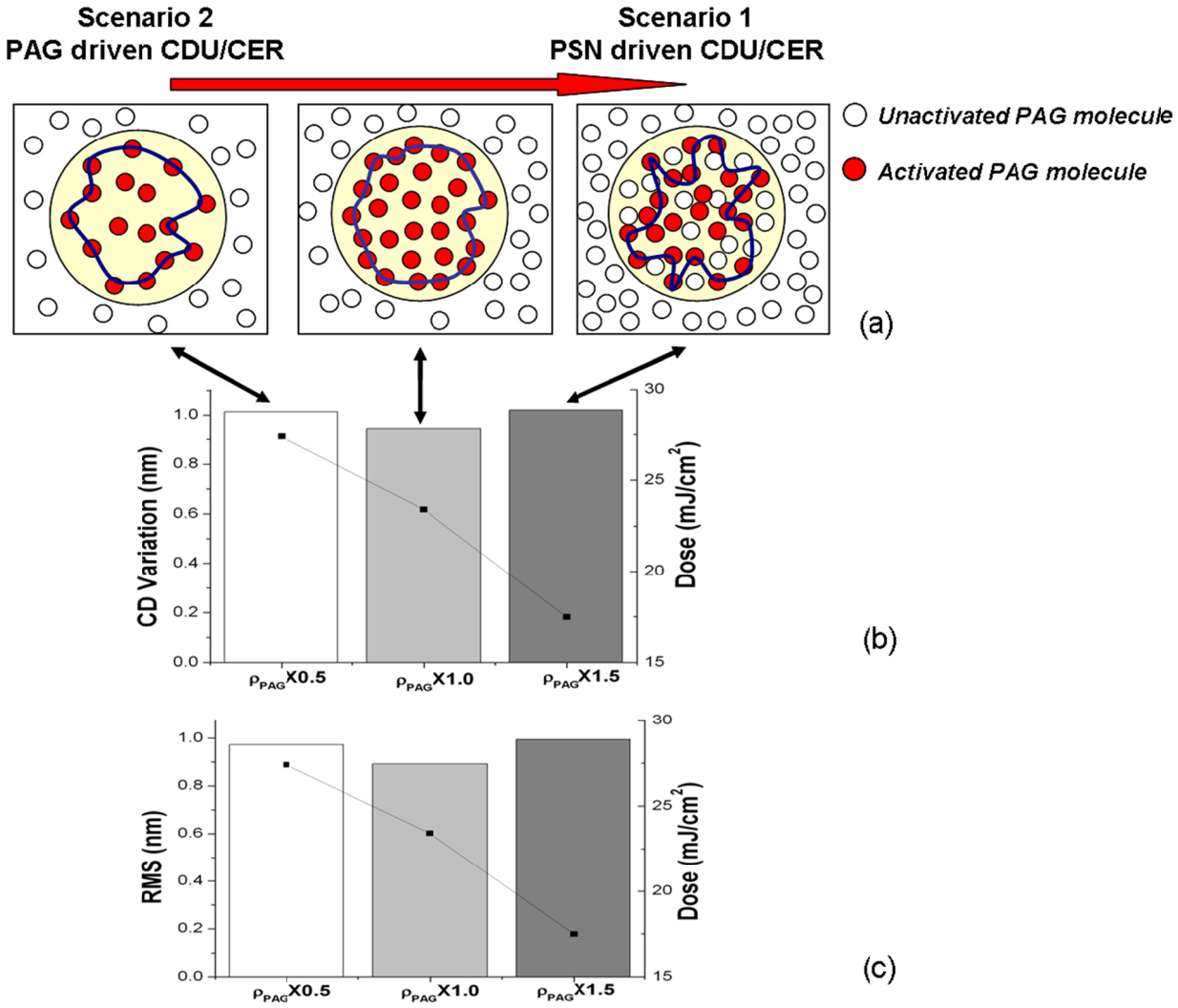

Figure 4.7 a) Schematic diagram of the transition from scenario 2 (PAG statistics driven CER/CDU) to scenario 1 (PSN driven CER/CDU), where the contact area is shown with yellow background, the inactivated PAG molecules with small hollow circles and the activated PAG molecules with red filled circles. Also, we show the bar diagrams for the CDU (b) and RMS (c) values at different PAG concentrations to facilitate the link to schematic diagram.

In other words, we can say that going .0from PAG– to PAG+ a transition from scenario 2 and CDU determined by PAG distribution to scenario 1 and PSN-dominated CDU behavior seems to be observed in our experimental results. Fig. 9 shows schematically this transition from scenario 2 to scenario 1 (Figure 4.7 a) along with the bar diagram for CDU at different PAG concentrations (Figure 4.7 b). Although RMS dependencies will be discussed in the next subsection, Figure 4.7 c shows also the effects of this transition to RMS value exhibiting a similar minimum at ST (Standard resist) formulation similarly to CDU behavior.

In the same spirit, the addition of quencher to PAG+ resist formulation (scenario 1) should be considered with PSN arguments. Consequently, the decrease of CDU in QNPAG+ can be explained by the increase of dose and the concomitant reduction of PSN effects.

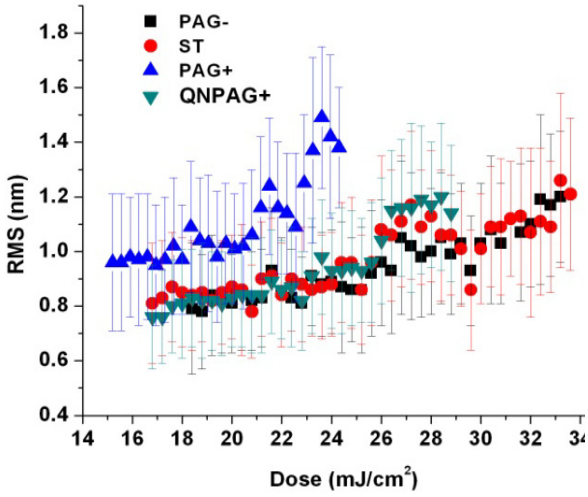

(a)

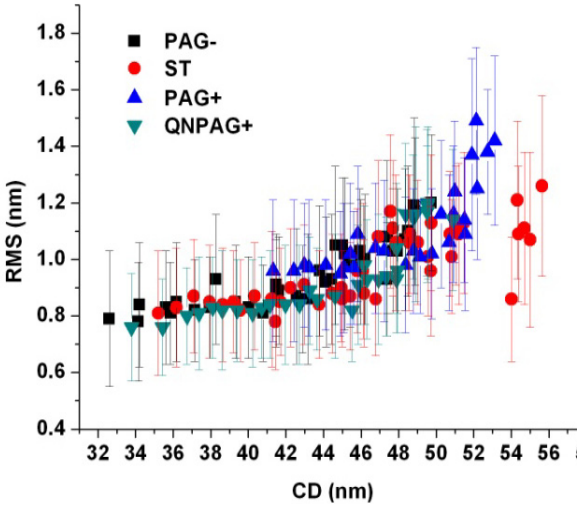

(b)

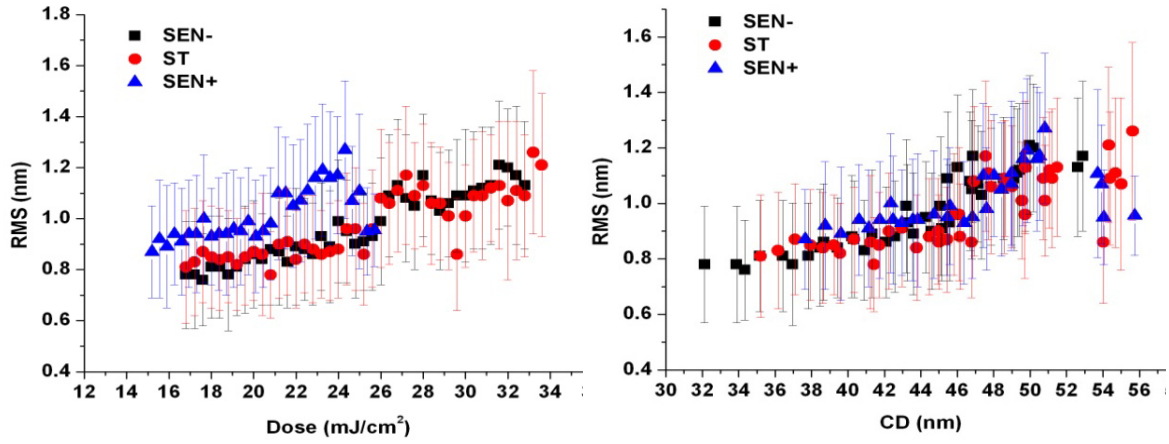

(c) (d)

Figure 4.8 RMS versus dose (4.8a and 4.8c) and CD (4.8b and 4.8d) for all resist formulations with various PAG, quencher and sensitizer concentrations shown in Table 5.

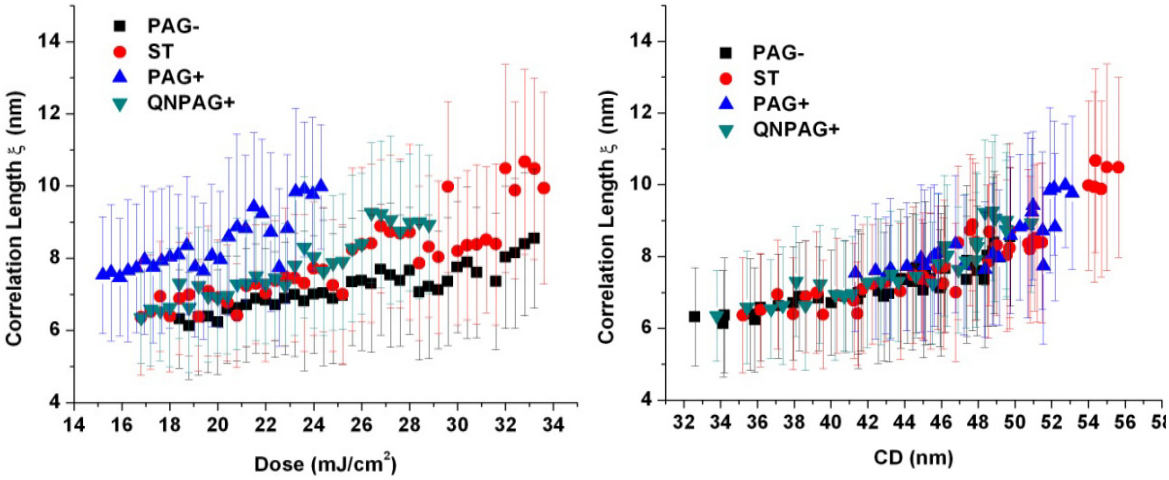

(a) (b)

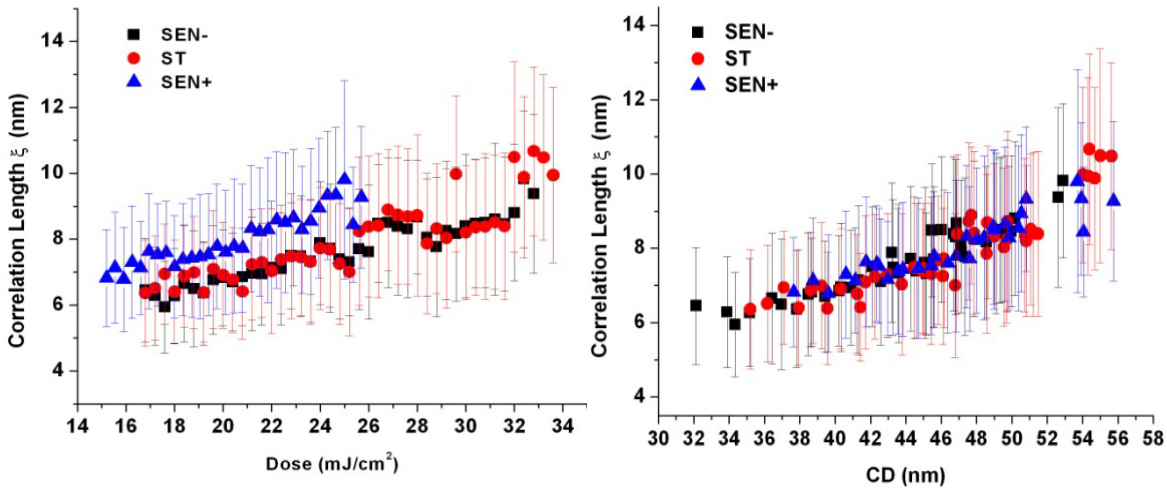

Figure 4.9 Correlation length ξ versus dose (4.9a and 4.9c) and CD (4.9b and 4.9d) for all resist formulations with various PAG, quencher and sensitizer concentrations shown in Table 5.

4.4.3. Effects on CER parameters

RMS and ξ values are less scattered than CD variation and exhibit an overall increasing trend with dose. Also, at all doses, high ρ_{PAG} and $\rho_{sensitizer}$ result in larger RMS and ξ (see Figures 4.9 a, b and 4.9 a, b) with more dramatic increase when we move from 1 to 1.5 ρ_{PAG} or $\rho_{sensitizer}$. In QNPAG+ resist, RMS and ξ decrease and retain similar trend as standard resist. Both experimental results (increase of RMS with dose and PAG concentration) are contrary to PSN and ASN argumentation according to which higher doses and PAG loadings should lead to smaller RMS values. Subsequently, the interpretation of these trends demands new effects involved in CER dependencies.

In order to bring to the surface these effects, we plot the experimental data versus the final CD value using the correspondence shown in Figure 4.3. We observe that they come together and are unified to a single trend (Figures 4.8 b and 4.8 d) revealing the critical role of CD in CER behavior. In all cases, RMS remains almost fixed (or very slightly increasing) until CD~42nm and then exhibits a more striking increase The correlation length in both cases shows an almost linear increasing behavior versus CD (Figures 4.9 b and 4.9 d), which

means that for all CDs the high frequency edge fluctuations are extended to an almost constant portion (~15-20%) of contact edges.

To obtain the full-spectrum information of CER dependence on CD, we plot the PS for various CD values in Figure 4.10. PS show that the increase in RMS at high CD comes mainly from the enhanced contribution of low frequency deformations of contact edge shape. In other words, it seems that the wider contacts favor the development of stronger low frequency fluctuations in CER which is responsible for the observed increase of RMS with CD.

Since this behavior is CER-specific and is not reported in LER, one may look for its origins to the main difference between contacts and lines: contacts have 2D circular topology whereas lines have 1D linear topology. This difference has two important consequences to CER and its CD dependence. First, the increase of CD in contacts causes enlargement of the contact edge length and subsequently, according to roughness theory, rise of RMS value which is shown in the Figure 4.12 (a). Second, the 2D topology of contacts in dense contact patterns leads to the enhanced proximity of contact edges along specific directions, which becomes stronger when CD increases and the pitch remains fixed (see Figure 4.11). This enhanced contact proximity along specific directions may result in preferential inter-contact communication in the terms of aerial image or acid kinetics and subsequently in the strengthening of low frequency undulations to contact edge morphologies (see Figure 4.11) and the RMS growth with CD. This is termed as the contact proximity effect and behavior of rms versus proximity of contact hole is shown in the Figure 4.12 b. Although, the first contact-edge effect should be present in the RMS dependence on CD changes in our experiments, modeling results show that the experimental CD increase is not enough to explain the amount and form (increasing rate) of the observed RMS growth as well as the enhancement of low frequency part of PS. On the contrary, the second effect of enhanced contact proximity along specific directions seems to fit better to the experimental

behavior and capture both RMS increase and strengthening of low frequency undulations with CD. Therefore, one can conclude that to understand and control CER dependencies one should take into account the geometrical consequences of the 2D circular topology of contacts which explain the observed critical role of CD.

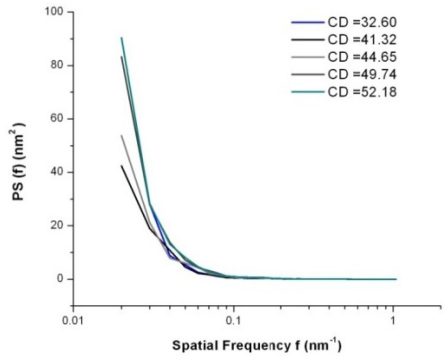

Figure 4.10 PS of the CER with CD ranging from 32.60nm to 52.18

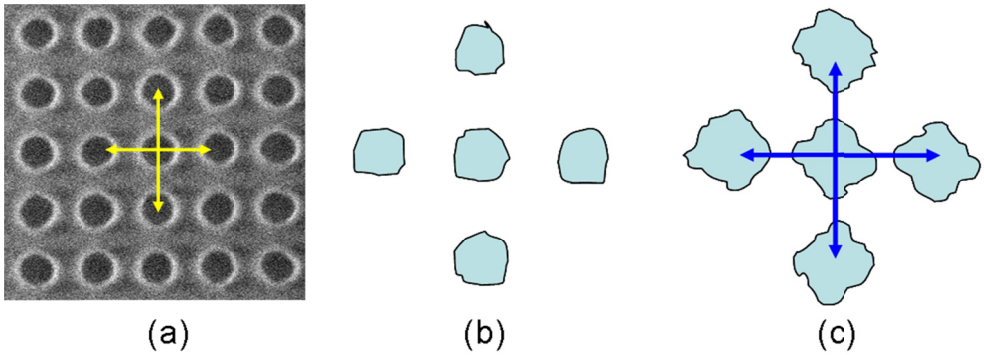

Figure 4.11 Schematic presentation of contact proximity effect. a) Directions in a real contact pattern of enhanced proximity of contacts, b) No effect of contact proximity on contact edge morphologies when they are distant and c) “stretching” of contact edges along the proximity directions causes low frequency undulations (“squareness”) in the contact shape and therefore increase of RMS value.

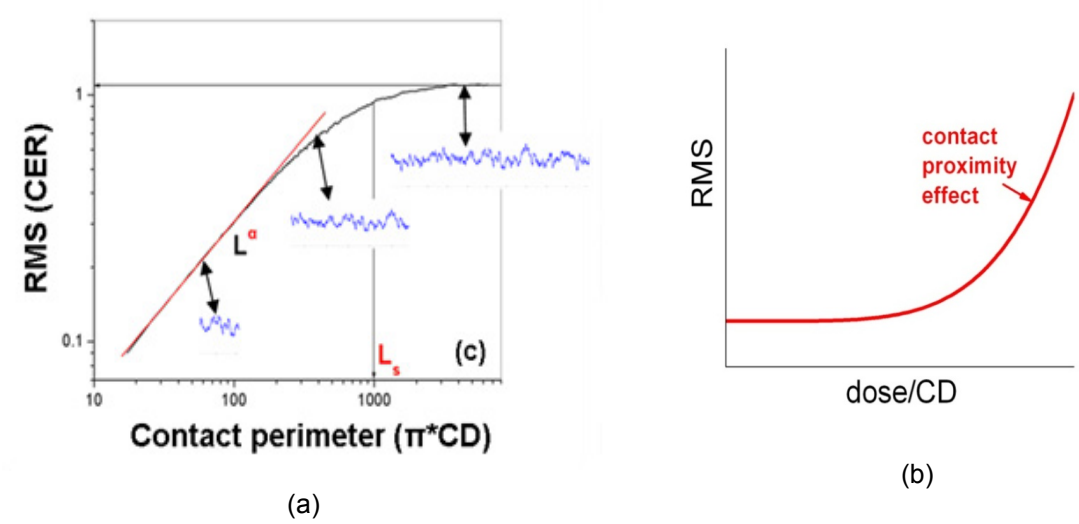

(a) (b)

Figure 4.12 (a) Contact edge length effect (b) Contact proximity efect

4.5. Summary

In EUV lithography, the mechanism of photon energy conversion to polymer deprotection is more complicated than those in 193 and 248nm lithography since it is mediated through the generation and action of secondary electrons which interact with PAG molecules and produce acids to deprotect polymers. This complexity results in a more integrated picture for the dependence of LWR: depending on the relative density of activated PAG molecules to the total PAG loading, LWR may be determined by PSN effects or PAG distribution statistics. Understanding the interplay between these two factors may be the key for explaining and controlling the effects of various process conditions and material properties on LWR in EUV resists.

In this thesis, motivated by the recent upsurge of interest in EUVL for uniform and smooth contact hole fabrication, we performed a systematic experimental study for the effects of sensitizer, PAG and quencher loadings in an EUV resist on CDU and CER parameters and applied the above LWR arguments in the interpretation of the experimental results. We found that the sensitizer and

quencher impact on CDU can be interpreted in the terms of PSN effects and lower sensitizer and higher quencher concentrations favor more uniform contacts. More interestingly, the PAG dependence of CDU can be described in the terms of a transition from PAG distribution to PSN determined effects and a minimum of CDU is obtained for the standard resist formulation.

On the other hand, the behavior of single contact roughness parameters (RMS and correlation length) is mainly dominated by the low frequency edge fluctuations as spectrum analysis reveals. We attributed these undulations to the interaction between the aerial image and/or acid kinetics of nearby contacts (inter-contact effect), which are enhanced along specific directions determined by the contact lattice structure on the wafer and give rise to the increased low frequency fluctuations of contact edges. This argumentation explains the experimentally observed RMS increase with dose, CD and PAG loading.

5. MODELING CER AND CDU FORMATION: PATTERN PARAMETERS VERSUS PHOTON SHOT NOISE AND ACID DIFFUSION

5.1. Introduction

In the previous Chapter 4, we presented experimental results which show that CER behavior differs dramatically than LER behavior when they are examined versus exposure dose. We attributed this CER peculiar behavior to the different circular (2D) topology of contact holes compared to the linear (1D) topology of lines in LER. In particular, we argued that the circular topology of contacts induces two new (with respect to LER) effects on sidewall roughness: a) the contact-edge-length effect which depends on the diameter of the contact (CD) and b) the contact-proximity effect which involves the distance between contacts, the so called pitch parameter. Both pattern parameters (CD and pitch) may affect CER but the frequency analysis of CER revealed the primary role of the contact-proximity effect.

Despite the qualitative success in the explanation of the experimental trends, the above argumentation needs further investigation since several questions

remain open. For example, it is not clear the relationship of these topology effects with the conventional process and material effects (photon shot noise, chemical gradient) which dominate LER/LWR. When and under which conditions do they dominate? Furthermore, another open issue is the impact of these effects on the CDU behavior. Does contact-edge-length or contact-proximity effect have an influence of CDU trends and values? Given the recent upsurge of interest in CDU dependencies in EUVL, the latter question is of great importance.

The above questions can be investigated by designing new experiments in which the critical parameters (pattern, process and material) will be appropriately varied in a controlled way and then analyzing their results. However, the experiments with EUVL are very expensive and time consuming since only a limited number of EUV scanners are available worldwide. Furthermore, due to the complexity of the EUVL process, it is not always possible in experiments to distinguish and evaluate separately the effects of different parameters. Therefore, we motivated to develop a modeling approach of the CER and CDU formation and apply it to investigate the effects of pattern parameters on CER and CDU with respect to those of photon shot noise and acid diffusion. Presumably, modeling is faster, cheaper and more efficient to advance further understanding. The aim of this chapter is to present our modeling approach, its assumptions and the results of its application concerning the above issues (section 5.3). Before it, we will give a brief account of the previous works on modeling sidewall roughness formation whose large majority is devoted to LER/LWR (section 5.2). The chapter closes with the summary of our modeling and findings and the remaining open questions which can motivate future work (section 5.4).

5.2. Previous works

5.2.1. LER/LWR

5.2.1.1 Analytical modelling

Gallatin made the first attempt to derive an analytic formula by incorporating the main dependencies of LER in 2005. The derivation was based on a model of LER formation which includes (a) random photon absorption and acid generation (photon shot noise), (b) acid diffusion during the PEB step, (c) development of the deprotected fraction of resist using the criteria that is inspired by the critical ionization model [165]. The model ignores in-homogeneities in material concentrations (resist, PAG, quencher) and dissolution rates as well as the details of the reaction-diffusion kinetics. Also it does not consider the molecular structure of the resist, and hence molecular weight or polymer structure effects cannot be taken into consideration. The model provides an analytical formula for the scaling dependencies of LER on shot noise (exposure dose E_{size}), acid diffusion length R and image log slope (ILS):

$$\sigma_{LER} \approx \text{constant} \times \left(\frac{1}{ILS}\right) \sqrt{\frac{1}{\rho_{PAG}\ \alpha\ Q\ v\ E_{size} R^3}}$$

where ρ_{PAG} is the density of PAG loading (molecules/volume), α is the resist absorptivity (1/μm), Q is the quantum yield (acid generated/photons absorbed) and v the photon-acid interaction volume.

As shown in this formula, model is able to predict the basic scaling dependencies of LER on ILS, dose and acid diffusion length (PEB temperature or time). Furthermore, the model can also reproduce the spatial characteristics of LER quantified in PSD curves with appropriate determination of the acid diffusion length [161].

Fukuda and others [166]000 implemented similar kind of models. The main objective of the modeling is the analytical understanding of the tradeoff among Resolution, Line Edge Roughness and Sensitivity (RLS trade off), which guided recent resist research especially in EUV lithography.

C. Mack did further extension of the analytical approach based on the assumption that LER is proportional to the standard deviation of the of the blocked (insoluble) polymer concentration (σ_{m^*}) divided by its gradient perpendicular to the line edge dm*/dx:

$$LER \propto \frac{\sigma_{m^*}}{dm^*/dx}$$

This formula can be used for qualitative prediction of the effects of process and material parameters on LER. For example, increase in exposure dose causes reduction of the numerator and increase of denominator leading to a total decreasing trend in harmony with experimental results. On the other hand, large acid diffusion lengths decrease both σ_{m^*} and dm*/dx leading to the conclusion that there should be an optimum acid diffusion length for getting the lowest LER. In order to extract quantitative predictions from this approach, Mack applied a stochastic model for exposure and reaction-diffusion kinetics of chemically amplified resist which was taking into consideration of the in-homogeneities in chemical concentration and utilizing the concept of von Smoluchowski trap for the polymer deprotection reaction 000. The output of this model is a complicated formula for LER dependencies which was able to predict the existence of an optimum acid diffusion length for LER reduction and relate it with the radius of the von Smoluchowski trap 0.

5.2.1.2 Numerical simulations

Although analytical modeling approaches illuminate the fundamental dependencies of LER and provide straightforward interpretations of some of the experimental trends, the microscopic details of the resist and the relevant physicochemical processes can be captured only in numerical models

simulating LER formation. This is especially true for the acid generation and kinetics during PEB, and the development process in which resist structure may play a significant role. Indeed, most proposed numerical models focus on the detailed simulation either of the acid reaction-diffusion kinetics or of the development of deprotected resist. All of these can be characterized as mesoscale, since microscopic models e.g. molecular dynamics are still limited to simulation scales of only a few nanometers with long computational times. Table 6 lists the majority of the published simulation approaches for LER formation, and gives information about the modeling of the main lithographic steps and the predictions for LER (the models are referred to by the first authors of the related papers). For the sake of completeness, we also include in Table 6 the analytical approaches reported above.

	Exposure	**Material**	**Acid generation and kinetics**	**Development**	**Predictions**	**Comments**
Gallatin (analytical) [161]	PSN* and ILS* included	Randomly distributed PAG* in a homogeneous continuous resist medium	Modelling of the acid diffusion around its generation point	Simplified version of CIM*	LER dependencies on dose, acid diffusion length, and ILS (RLS* trade off), PS of LER	Provided quantification of RLS trade off, successful comparison with experimental results for EUV
Mack (analytical) 000	PSN*	Inhomogeneous chemical concentrations	Detailed diffusion-reaction kinetics with Smoluchowski's model		LER vs. acid diffusion length	
Lawson [173][174]	Cosine aerial image	3D cell representation	Dill C equation for	Kinetic Monte Carlo	LER vs. Dose-to-	Applied mainly to

	intensity variation	of resist. No cell-to-cell chain connectivity is considered. PAG* and quencher loading and aggregation included.	the probability of acid generation, Kinetic Monte Carlo modelling of acid kinetics on resist lattice	approach based on a cell dissolution rate determined by the enclosed protecting groups	size, PAG and quencher base loading, ILS*, PAG* aggregate size. Good correlation of LER with polymer protection gradient for homogeneous PAG distributions	molecular resists, Small simulation volume
Saeki - Kozawa [175]00	Gaussian e-beam (radius=1nm) exposure: 3D electron trajectories in resist simulated with commercial software.	Continuous representation with acid generators and quenchers as spheres	Proton and counter anion distribution calculated through an ionization model for CAR* and Monte Carlo techniques	Mack's dissolution model [Mack 1987]	LER vs. exposure dose, development time, line width, quencher concentration. Full spectral analysis for the detection of low-frequency LER causes.	Applied to e-beam and EUV lithography, Small simulation volume
Morita 00[180]	Ideal aerial image	Coarse-gained representation of polymers with dissipative particle	A particle is converted to unblocked by the reaction contact with	Removal of unblocked particles	LER vs. polymer chain dynamics, developmen	

		dynamics method	PAG		t and rinse processes, number of block copolymers	
Biafore [181][182] 0	PSN* included	Lattice with atomic nuclei and a sea of electrons, random PAG* and quencher	Photoelectron scattering and Smoluchowski's model for reaction-diffusion of generated acids with PAGs and quenchers taken into account	No reference to development modelling	LER vs. dose, focus and pitch. Also PAG* concentration effects on Esize and LER trade off	
Schnattinger 00	Use of calibrated continuous models	3D cell representation of polymer, self-avoiding random polymers with chain structure and PAG* loading included	Dill C equation for the probability of acid generation, Kinetic Monte Carlo modelling of acid kinetics on resist lattice	CIM* with experimental calibration	LER (rms) vs. development time, average polymer chain length, type of polymer chains, AIC*, acid diffusion length, quencher concentration, exposure dose	

Patsis 00000000	Ideal aerial image or imported from commercial software	3D cell representation of polymer, self-avoiding random polymers with chain structure and PAG* loading included	Acid generation through a threshold of a uniform probability. This threshold corresponds to the exposure dose. Monte Carlo modelling of acid kinetics on resist lattice	CIM* in real time, or fast projection in time	LER vs. average polymer chain length, type of polymer chains, PAG concentration. Also included effects of acid diffusion range on the polymer chain length impact on LER/LWR, full spectral analysis and inclusion of secondary electron diffusion in EUV	Used to study effects of molecular weight, chemical in-homogeneities. Also involved in scaling analysis studies.
Philippou 0	Fixed AIC* from commercial s/w (c~0.8 with 9% flare)	3D cell representation of polymer structure obtained by MD* and self-avoiding random polymers	Stochastic modelling utilizing the cell resist description and specific reaction rates	Cell implementation of CIM* (no chain structure taken into account)	LER vs. polymer length, PAG* concentration, CD and diffusion coefficient. Also correlation length and roughness	Small simulation volume, overestimation of high frequency LER.

					exponent vs. polymer size	

Table 6 Analytical and numerical models of LER formation: Assumptions for the main lithography steps, predictions of experimental results and some comments.

5.2.2. CER

Despite the large amount of works on modeling and simulation of LER, there is only a couple of papers dedicated to a systematic study of CER formation and the contribution of process and material effects on it [196][197]. In these papers, the authors examine the predicted resist images for 50- and 80-nm contacts in the presence of three sources of fluctuations: those associated with dose statistics, those associated with random photon absorption sites, and those associated with resist chemistry. Photon absorption simulations were done using simple optics theory or Monte Carlo techniques. These absorption maps were converted into an initial map of photoacid concentration and an acid diffusion model was used to obtain the developable latent image. A new dissolution model was applied to estimate the final resist profile, and image analysis routines were used to extract the contact diameter fluctuations (CDU), and edge roughness statistics (CER). The simulations show that each source of fluctuation can be significant with the statistics of deprotection chemistry to dominate in some cases. Quite interestingly, they found that for CD=50nm contacts, the RMS of CER does not decrease with dose for the range of doses they studied in their simulations which may be indicative of a resist system that is reaching its resolution limit. On the contrary, in larger contact holes they obtained the expected decrease with of CER with dose.

5.3. Our modelling approach and results

Looking at the modeling and simulation approaches presented in the previous section, one can conclude that the analytical approach proposed and elaborated by Gallatin captures the fundamental dependencies of LER and predicts a reasonable Power Spectrum close to experimental findings using a simple modeling framework for the formation of LER. Thus, it seems logical to extend it to the study of CER formation and check its potential to the investigation of the role of the patterning parameters (CD, pitch). However, we prefer the numerical implementation of the model instead of its analytical solution since the latter is prevented by the incorporation of contact proximity (inter-contact) effects needed if we want to examine the effects of pattern parameters. Furthermore, the numerical implementation avoids the consequences of the further assumption made for the analytical treatment of the model.

Therefore, in this chapter we develop a model which is actually a numerical implementation of Gallatin's approach using Monte-Carlo techniques and apply it to model the formation of CER and CDU in pattern with many contact holes. By numerical modeling we avoid the assumptions by Gallatin to solve analytical the equations.

5.3.1. Assumptions and description

As referred above, we will follow Gallatin's modeling framework which includes (a) random photon absorption and acid generation (photon shot noise), (b) acid diffusion during the PEB step, and (c) a simplified version of the critical ionization model (CIM) for the development and formation of contact features.
Therefore the implied assumptions of our modeling are : a) the aerial image is ideal having a step-wise profile on resist surface, b) each EUV photon is absorbed and generates one acid with probability 1 (quantum yield=1), c) the acid diffusion and the subsequent polymer absorption is described by a

Gaussian probability function decaying around the position of acid generation, d) the polymer is dissolved during development when the deprotection probability exceeds a specific threshold (simplified CIM) and e) the resist is supposed to be a homogeneous material. The latter means that we ignore in-homogeneities coming from the distributions of PAG and other resist ingredients as well as resist molecular structure. In the previous Chapter 4, we saw that PAG distribution plays a significant role in CDU dependencies. However, when we study the dependence of CER on dose and CD a unique trend is observed for all PAG, sensitizer and quencher concentrations. Since we are interested in understanding and modeling the latter behavior, we can consider the strong assumption for homogeneous resist.

A schematic flow diagram describing the steps of the model is shown in Figure 5.1.

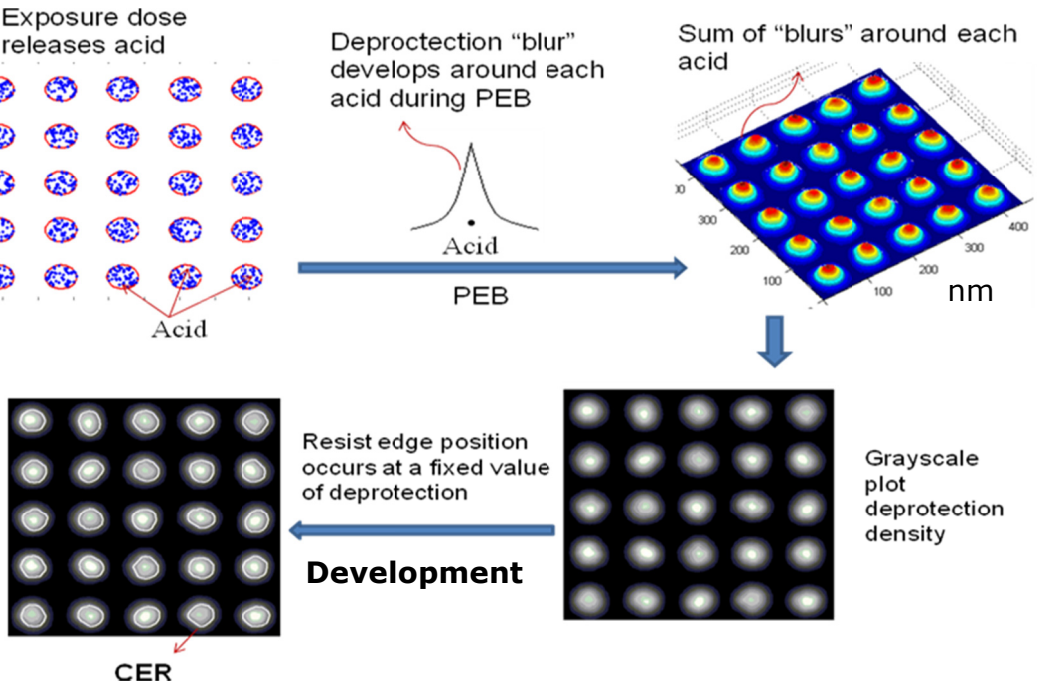

Figure 5.1: Schematic diagram of the flow for CER modeling.

First an exposure matrix is generated where the predefined mask openings are created with known CD and pitch. The photons of the EUV irradiation are randomly distributed inside contact areas in accordance with the exposure dose

modeling the shot noise effects. Each photon generates one acid. Now during the post exposure bake (PEB), a deprotection blur is formed around the released acid which is quantified with a probability density function whose width is determined by the acid diffusion length (ADL). The summation of all these blurs from the obtained acids will give the net deprotection probability function inside the contact area. Resist development is implemented using what can be viewed as a large scale equivalent to the critical ionization model [165] [195]; an appropriate threshold level is chosen and the contact areas which have deprotection greater than that of the threshold are removed. This way contacts with rough edges (CER) are formed.

At present, the model runs in 2D but its extension to 3D seems to be straightforward.

5.3.2. Validation with experimental behaviour

To validate the model described in the previous sub-section, we compare typical PS and HHCF of contact edges generated by the modeling with the corresponding experimental curves from contacts with similar CD (~37nm) (see Figure 5.2). Apparently, modeling predictions capture quite sufficiently the overall experimental behavior in both functions with worse agreement at low frequencies/large scales. From the PS and HHCF it is clear that the modeling RMS value is lesser than experimental value which is shown in Figure 5.2. This means that other factors not including in the model may contribute to these quantities. Despite these quantitative discrepancies between model and experimental behavior, it seems that this simplified model for CER formation can capture the frequency/scaling characteristics of the experimental CER.

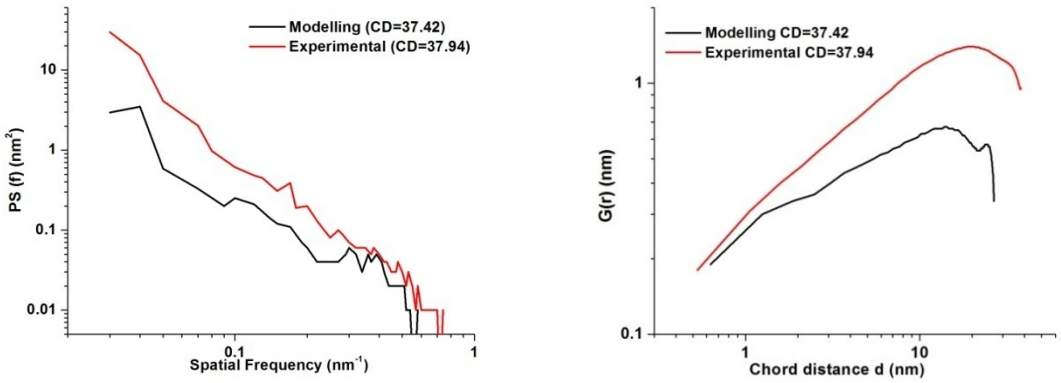

a) b)

Figure 5.2 a) PS of the CER of CD 37.94 and model CER of CD 37.42 and b) HHCF of the CER of CD 37.94 and model CER of CD 37.42

5.3.3. Results and discussion

The main assumption of the model is that the origin of CER is the shot noise of photon or acids combined with superposition of the resist deprotection blurs generated around each released acid during PEB.

To check out the model potential to capture the experimental CER behavior versus dose and CD, we apply it to generate a pattern of 5x5 contacts by tuning the model parameters so that the final contacts have CD close to the experimental values. By varying the dose (number of photons), we can scan a range of CD values including that of the experimental diagrams (see Section 4.4). Then the RMS and CD variation of the edges of the generated contact holes are calculated for two pitches 60 and 200 and CD in the range 15<CD<50nm. The first pitch is close to the experimental one, while the second is sufficiently large to minimize any contact proximity effect. Therefore, by comparing the results from the two different pitches, we could be able to pick up the effects of contact proximity and interaction on RMS of CER and CDU. The model results are shown in Figure 5.3.

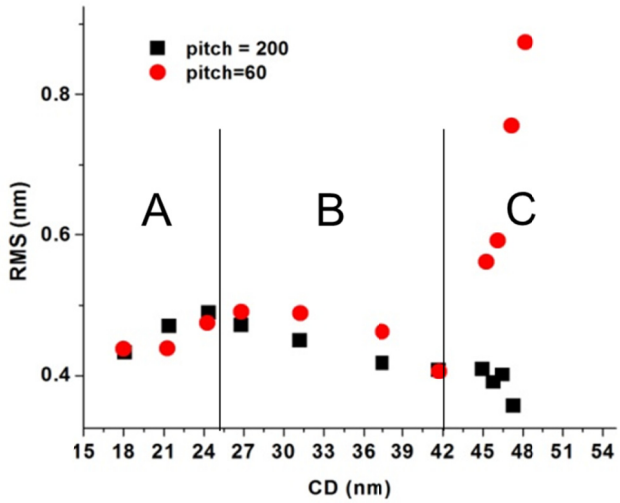

(a)

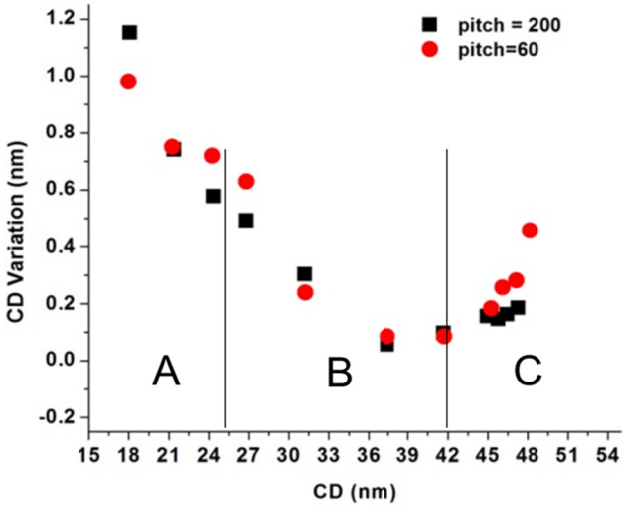

(b)

Figure 5.3 Modeling results for RMS (a) and CD variation (b) vs measured CD for Pitch = 60 (red full circles) and 200 (black full squares). Notice the three regimes of CD effects on RMS and CDU with B and C closely reproduce the corresponding experimental trends (cf. Figure 4.4b & 4.4d in chapter 4)

Figure 5.3a shows that for both pitches, one can distinguish three regimes in RMS dependence on CD. In the regime A (CD<25nm), RMS increases

gradually, while for CD>27nm it decreases very slightly till CD=42nm (regime B). No difference is observed between the two pitches in these two first regimes. For CD>42nm, there is a tremendous increase in the RMS for the pitch=60nm whereas for the pitch=200nm, RMS continues to decrease. This difference between two pitches may be attributed to the contact proximity effect. In the pitch 60nm, when the CD of the contact holes becomes 42nm, their edges come closer and induce interaction with each other through acid diffusion kinetics. The interaction of the neighboring contact holes causes a “squareness” of the contact shape leading to enhanced low frequency edge undulations and consequently an abrupt increase in the RMS at higher CD (see Figure 5.4). On the contrary, when the contacts are practically isolated and interactions between these can be considered negligible the RMS behavior is dominated by the photon shot noise effects which explains the continuous decrease with dose.

To interpret the pitch-independent RMS behavior in the regimes A and B, we should recall the other two players in CER dependence: the photon shot noise and the edge-length effect. The first leads to decrease of RMS with dose and can explain the RMS lowering vs. dose in B regime. However, when CD becomes very small, the edge-length effect seems to dominate causing the observed increase of RMS value when CD goes up to ~27nm.

Summarizing, the model predicts that in CER the RMS behavior vs. dose and CD, depends on both photon shot noise and topology (contact edge-length and contact proximity) effects. Each one of these effects seems to dominate at different CD scales: Edge-length effects dominate at small CD (regime A), contact proximity controls RMS increase at large CD (regime B) while in the between regime B photon shot noise stops RMS increase and causes saturation and possibly a slight decrease.

The transition predicted by model from regime B to C characterized by the abrupt increase of RMS seems to capture the experimental trend shown in

Figure 4.8 b and Figure 4.8 d according to which RMS starts to increase for CD>42nm after an almost saturation period. Therefore, one can conclude that the increase of RMS versus dose at large CD which differentiates CER from LER behavior is indeed due to the increased proximity of nearby contacts and the subsequent interaction through acid kinetics or aerial image interference effects. Furthermore, the model predicts that at sufficiently small CD, RMS will lower due to contact-edge effects contrary again to LER expectations. This prediction remains open to experimental examination.

The Figure 5.3b concerns the second issue posed in the Introduction of this chapter, regarding the role of contact proximity effects in CDU dependence on CD and pitch. According to the modeling findings shown in Figure 5.3b, for both pitches 60nm and 200nm, the CD variation decreases gradually in A and B regimes and then (regime C) slightly increases with respect to CD with the lower pitch to exhibit more increase. The decrease of CD variation for CD<40nm (A and B regimes) can be attributed to both PSN and edge-length effects and is in accordance with experimental results (see Figure 4.4 b and Figure 4.4 d in chapter 4). The saturation and slight increase predicted by modeling at large CD is the result of contact proximity effect although in experiments a very slight increase can be observed merely in some cases (see the data for SEN+ and PAG+ formulations in Figure 4.4 b and 4.4 d).

(a) (b)

Figure 5.4. Contact edges created by our modeling for pitch=60nm when CD=21nm (a) and CD=47NM (b). Notice the increased “squareness” of contact edges at CD=47nm coming from the enhanced contact proximity.

5.4. Summary – Open Issues

In this chapter, we presented a 2D modeling approach to the lithographic formation of contacts with CER and CDU. The model is actually the numerical implementation for CER of the model proposed by Gallatin for LER and mainly includes the photon shot noise effects and the deprotection blur caused by acid diffusion. Due to its simplicity it can be applied to patterns with many contacts giving us the opportunity to study the role of pattern parameters (CD and pitch) on CER and CDU along with their concomitant contact edge-length and contact proximity effects. The main goal of model implementation and application is to interpret the experimental findings presented in the previous chapter showing a different CER behavior versus dose with respect to LER expectations. The key issue is to illuminate the interplay of the above-mentioned CER-specific topology effects with the photon shot noise impact.

The results of the modeling showed that in contacts, the behavior of RMS versus dose is not determined alone by photon shot noise effects such as in LER. The increase of dose is accompanied with larger CD values and therefore with the involvement of more edge-length in roughness measurements and increased proximity between contacts if pitch is kept fixed. Both contact edge-length and contact proximity effects induce increase in RMS contrary to shot noise trends. According to modeling, the contact proximity effects at sufficiently large CD are stronger than photon shot noise effects and can explain the RMS increase which has been reported in the experiments (cf. section 4.4). Furthermore, modeling predicts a reduction of RMS at small CD values, while in the middle CDs and doses photon; shot noise effects cause saturation and slight decrease of RMS.

Concerning CDU dependence on dose and CD, it is well-known that increased PSN effects lead to enhanced CDU at small CD values while the same trend is also expected by contact edge-length effect. The impact of contact proximity on CDU was not clear although due to the involved stochasticity an increasing trend at large CD was expected. The question was if this trend can outweigh the decreasing trends of PSN and edge-length effects. Modeling study revealed that at small pitches and large CD this is indeed the case, since a small increase of CDU is detected in the regime C of large CD values. This increase is only partially observed in experiments and further studies (both modeling and experimental) are needed to shed light on this point. Also, it is not clear what causes the slight increase in the regime C predicted by modeling at large pitch=120nm.

Despite the significant assumptions of the modeling approach we implemented and applied in this chapter, it seems that it is able to capture the fundamental trends observed in the experiments reporting the effects of dose and CD on CER and CDU and to illuminate their origins. A closer inspection of the modeling results reveals its failure to reproduce quantitatively the experimental values. Model RMS values lie at about 50% of the experimental values while in CDU the predictions are much worse. However, this is not a surprise due to model assumptions. The most important of these for sidewall roughness predictions is the assumed chemical homogeneity of resist structure and ingredients (PAG, sensitizer, and quencher). According to both modeling and experimental results, the contribution of chemical in-homogeneities to LER and CER is expected to be large and sometimes to dominate other factors [197][150]. Nevertheless, the comparison of our modeling results with experiments shows that this contribution does not affect importantly the trends of the dependence of CER and CDU on dose and CD.

6. CONCLUSIONS

6.1. Description of the problem

The increased stochastic effects in the nanofabrication processes result in patterned features with deviations from the designed shape and size uniformity. In the top-down approach to nanotechnology (lithographic techniques), the stochasticity is manifested in the roughness of the feature surfaces and the variability of their size. The roughness and variability issues become more evident in Extreme Ultra Violet Lithography since it is the strongest candidate for circuit manufacturing at critical dimensions <20nm. The fabrication of nanofeatures with controlled sidewall roughness and variability using EUVL requires the development of advanced metrological and modeling tools since the capabilities of the present methods are limited. To this end, in this thesis we have developed metrology and modeling methodologies specialized in the measurement of the roughness and variability of contact holes and the modeling of their fabrication. Then we apply these in the analysis and interpretation of experimental results as well as in the investigation of some process and material effects on contact sidewall roughness (Contact Edge Roughness, CER) and variability (Critical Dimension Uniformity, CDU).

6.2. Our methodology

To cope with the metrological challenge in EUVL, we developed a methodology for the measurement and characterization of CER and CDU using as input top-down CD-SEM images, processing these with image analysis techniques and giving as output the CER and CDU parameters as well as the Power Spectrum and correlation function for frequency and scaling analysis. This methodology has been implemented in home-made software named CERDEMO.

We have also developed a modeling approach to contact hole formation to provide better understanding of the experimental results and the origins of their trends and behavior. The modeling takes into account the photon shot noise effects, the acid diffusion blur of deprotection polymer statistics and a simplified threshold-based model for the dissolution. Due to its simplicity and easy implementation it can be applied to several contact holes and therefore it can consider the impact of pattern parameters such as CD and pitch. The model has been realized in the CERSIM software.

6.3. Results

6.3.1. CER/CDU metrology:

The metrological CERDEMO software has been applied to several CD-SEM images of contact holes fabricated by EUVL with different magnification to investigate some metrological issues. The first is the relationship between CER and LER. The frequency and scaling analysis of CER revealed the dominant role of low frequency undulations with respect to LER. In addition, the different 2D circular topology of contacts induces two new effects with potential impact on CER and CDU: a) variations of CD cause changes in the contact edge-length

included in the measurement of CER/CDU and therefore may affect their values according to roughness theory (*contact edge-length effect*), b) in dense contact patterns, increase of CD for fixed pitch brings contact edges closer enhancing contact proximity and interaction (*contact proximity effect*).

Also, we studied the effects of image magnification and noise smoothing filter on the CER and CDU values obtained with CERDEMO. It was found that high magnification increases both RMS and CDU, whereas reduces the measured correlation length. The noise smoothing filter gradually decreases RMS and CDU but increases ξ. Finally, we compared the inside image CDU (local CDU) with the CD variability among images (global CDU) and we found that the most significant contribution to CDU is the local CDU.

6.3.2. Origins and dependencies of CER/CDU

We analyzed several CD-SEM images of contact patterns fabricated with EUVL using two resists. In the second resist, six formulations have been examined with different concentrations of PAG, sensitizer and quencher. The aim is to examine the impact of exposure dose and resist ingredient concentrations on CER parameters and CDU.

In all cases, CDU goes up at small CDs while it saturates and in some cases increases slightly at large CD. RMS of CER presents totally different behavior with respect to dose than LER. Instead of going down with dose, it increases initially very slowly and then more abruptly. When data points for RMS from all experiments are plotted versus final resist CD, they coalesce indicating critical role of contact CD in CER dependencies on resist ingredients. Both contact edge-length and contact proximity effects are controlled by CD and fixed pitch lead to increased RMS with CD. Frequency analysis of CER revealed the possible domination of the contact proximity effects and its principal role in the abrupt increase at large CD.

In the same set of experiments but for fixed CD, the study of the impact of PAG loading on CER/CDU revealed a minimum at the middle PAG concentration. This has been associated with a transition from a regime where CDU/CER is dominated by PAG statistics to a regime driven by photon shot noise (PSN) effects. Sensitizer and quencher effects are in accordance with LER expectations and can be explained based only on PSN effects.

Application of the developed modeling approach confirmed the role of contact proximity effects on CER abrupt increase in large CD values and predicted the manifestation of contact edge-length effects on CER in small CDs. Finally, model showed that CDU is slightly affected by contact proximity effects especially at large CD values. PSN effects are manifested mostly in the middle CD values. Therefore, contrary to LER, dose dependence of CER and CDU is more complicated since it involves besides PSN the effects of the 2D circular topology of contacts (contact edge-length and contact proximity effects).The quantitative differences between model predictions and experimental results may be attributed to the overlooking of the effects of chemical resist in-homogeneities in our model.

REFERENCES

[1] G. E. Moore, “Cramming more components onto integrated circuits,” Electronics 38, April 19 1965.

[2] J. H. Bruning, “Optical lithography: Thirty years and three orders of magnitude,” in Advances in Resist Technology and Processing XIV, R. G. Tarascon-Auriol, ed., Proc. SPIE 3049, pp. 14–27, 1997.

[3] G. E. Moore, “Lithography and the future of Moore’s law,” in Optical/Laser Microlithography VIII, T. A. Brunner, ed., Proc. SPIE 2440, pp. 2–17, 1995.

[4] A. J. den Dekker and A. van den Bos, “Resolution: A survey,” J. Opt. Soc. Am. A 14, pp. 547-557, March 1997.

[5] J. R. Sheats and B. W. Smith, eds., Microlithography: Science and Technology, Marcel Dekker, Inc., New York, 1998.

[6] B. W. Smith, “Optics for photolithography,” pp. 171–270 in Ref [5].

[7] A. K.-K. Wong, Resolution Enhancement Techniques in Optical Lithography, SPIE Press, Bellingham, WA, 1990.

[8] H. J. Levinson, Principles of Lithography, SPIE Press, Bellingham, WA, 2001.

[9] J. E. Bjorkholm, “EUV lithography–the successor to optical lithography?,” Intel Technology Journal , 3rd quarter 1998.

[10] V. Banine and R. Moors, “Extreme ultraviolet sources for lithography applications,” in Emerging Lithographic Technologies V, E. A. Dobisz, ed., Proc. SPIE 4343, pp. 203–214, 2001.

[11] G. D. Kubiak, L. J. Bernardez, and K. Krenz, “High-power extreme ultraviolet source based on gas jets,” in Emerging Lithographic Technologies II, Proc. SPIE 3331 Vladimirsky,ed., pp. 81–89, 1998.

[12] G. D. Kubiak, L. J. Bernardez, K. Krenz, and W. C. Sweatt, “Scale-up of a cluster jet laser plasma source for extreme ultraviolet lithography,” in Emerging Lithographic Technologies III, Proc. SPIE 3676,Vladimirsky ed., pp. 669-678, 1999.

[13] L. Rymell, M. Berglund, B. A. M. Hansson, and H. M. Hertz, “X-ray and EUV laser plasma sources based on cryogenic liquid-jet target,” in Emerging Lithographic Technologies III, Proc. SPIE 3676, Vladimirsky, ed., pp. 421–424, 1999.

[14] D. Attwood, Soft X-Rays and Extreme Ultraviolet Radiation, Cambridge University Press, Cambridge, 1999.

[15] T. W. Barbee, Jr., S. Mrowka, and M. C. Hettrick, “Molybdenum-silicon multilayer mirrors for the extreme ultraviolet,” Applied Optics 24, pp. 883–886, Mar. 15 1985

[16] P. yang Yan, G. Zhang, P. Kofron, J. Chow, A. Stivers, E. Tejnil, G. Cardinale, and P. Kearney, “EUV mask patterning approaches,” in Emerging Lithographic Technologies III, Y.Vladimirsky, ed., Proc. SPIE 3676, pp. 309–313, 1999.

[17] P. yang Yan, C. wei Lai, and G. Cardinale, “EUV mask contact layer defect printability and requirement,” in Emerging Lithographic Technologies IV, E. A. Dobisz, ed., Proc. SPIE 3997, pp. 508–514, 2000.

[18] D.Van Steenwinckel, J. H. Lammers, L. H. Leunissen, and J. A. J. M. Kwinten, “Lithographic importance of acid diffusion in chemically amplified resists,” Proc. SPIE, vol. 5753,pp. 269–280 (2005)

[19] T. Kozawa, S. Tagawa, J. J. Santillan and T. Itani, “Impact of Nonconstant Diffusion Coefficient on Latent Image Quality in 22 nm Fabrication using Extreme Ultraviolet Lithography,” J. Photopolym. Sci. Technol., vol. 21, pp. 421 (2008)

[20] A. Telecky, P. Xie, J. K. Stowers, A. Grenville, B. Smith, and D. A. Keszler, “Photopatternable Inorganic Hardmask,” J. Vac. Sci. Tech., vol. 28, issue 6, pp. C6S19 (2010).

[21] M. Trikeriotis, M. Krysak,Y. S. Chung, C. Ouyang, B. Cardineau, R. Brainard, C. K. Ober, E. P. Giannelis, K. Cho, “A new inorganic EUV resist with high-etch resistance”, Proc. SPIE, vol. 8322, pp. 83220U (2012)

[22] B. Cardineau, M. Krysak, M. Trikeriotis, E. Giannelis, C. K. Ober, K. Cho, R. Brainard,“ Tightly bound ligands for hafnium nanoparticle EUV resists”, Proc. SPIE, vol. 8322, pp. 83220V (2012)

[23] H. Oizumi, T. Kumise, T, Itani, “Development of New Negative-tone Molecular Resists Based on Calixarene for EUV Lithography”, J. Photopolym. Sci. Technol, vol. 21, no. 3, pp. 443 (2008)

[24] R. Gronheid, G. Winroth, A. Vaglio Pret, T. R. Younkin, “Quantification of shot noise contributions to contact hole local CD non-uniformity”, Proc SPIE, in publication (2012)

[25] R. Gronheid, B. Rathsack, S. Bernard, A. Vaglio Pret, K. Nafus, S. Hatakeyama, “Effect of PAG distribution on ArF and EUV resist performance”, Journal of Photopolymer Science and Technology, vol. 22, issue 1, pp. 97-104 (2009)

[26] J. W. Thackeray, “Materials challenges for sub-20-nm lithography”, JM3, vol. 10, issue 3, pp. 033009 (2011)

[27] Y. J. Kwark, J. P. Bravo-Vasquez, M. Chandhok, H. Cao, H. Deng, E. Gullikson, C. K. Ober, “Absorbance measurement of polymers at extreme ultraviolet wavelength: Correlation between experimental and theoretical calculations”, J. Vac. Sci. Technol. B, vol. 24, issue 4, pp. 1822 (2006)

[28] T. Kozawa, S. Tagawa, “Radiation Chemistry in Chemically Amplified Resists”, JJAP, vol. 49, issue 3, pp. 030001 (2010)

[29] J. J. Biafore, M. D, Smith, “Application of Stochastic Modeling to Resist Optimization Problems”, Proc. SPIE, in publication (2012)

[30] C. D. Higgins, C. R. Szmanda, A. Antohe, G. Denbeaux, J. Georger, R. Brainhard, “RLS Tradeoff and Quantum Yield of High Photo Acid Generator Resists for Extreme Ultraviolet Lithography”, Proc. SPIE, vol. 7271, pp. 727147 (2009)

[31] G. Han, F. Cerrina, “Energy transfer between electrons and photoresist: Its relation to resolution”, J. Vac. Sci. Technology. B, vol. 18, issue 6, pp. 3297 (2000)

[32] C. A. Mack, “Fundamental principles of optical lithography”, chap. 5-7, J. Wiley & Sons, London (2007)

[33] D. ben-Avraham, S. Havlin “Diffusion and Reactions in Fractals and Disordered Systems”, chap. 12,13, Cambridge University Press, Cambridge (2000)

[34] J. J. Biafore, M. D. Smith, D. Blankenship, S. A. Robertson, E. van Setten, T. Wallow, Y. Deng, P.P. Naulleau, “Resist pattern prediction at EUV”, Proc. SPIE, vol. 7636, pp. 76360R (2010)

[35] T. Kozawa, S. Tagawa, H. B. Cao, H. Deng, and M. J. Leeson, “Acid distribution in chemically amplified extreme ultraviolet resist,” J. Vac. Sci. Technol. B, vol. 25, issue 6, pp. 2481 (2007).

[36] A. Vaglio Pret, K. Garidis, R. Gronheid, J. Biafore “Stochastic Limitations for EUV Resist Kinetics Towards the 16nm Node”, International EUVL Symposium (2011), http://dc426.4shared.com/doc/1AdCy883/preview.html

[37] S. D. Hector, “EUVL masks: Requirements and potential solutions,” in Emerging Lithographic Technologies VI, R. L. Engelstad, ed., Proc. SPIE 4688, pp. 134–149,2002.

[38] T. Liang and A. Stivers, “Damage-free mask repair using electron beam induced chemical reactions,” in Emerging Lithographic Technologies VI, R. L. Engelstad, ed., Proc. SPIE 4688, pp. 375–384,2002.

[39] S. Burkhart, C. Cerjan, P. Kearney, P. Mirkarimi, and C. Walton, “Low-defect reflective mask blanks for extreme ultraviolet lithography,” in Emerging Lithographic Technologies III, Y.Vladimirsky, ed., Proc. SPIE 3676, pp. 570–577, 1999.

[40] B. M. McClinton, P. P. Naulleau, “Mask-roughness-induced line-edge roughness: rule of thumb”, JM3, vol. 9, issue 4, 2010.

[41] B. M. McClinton, P. P. Naulleau, “Mask roughness induced LER: geometric model at long correlation lengths”, Proc. SPIE, vol. 7969, pp. 79691Y, 2011.

[42] S. A. George, P. P. Naulleau, I. Mochi, F. Salmassi, E. M. Gullikson, K. A. Goldberg, E. H.Anderson, “Extreme ultraviolet mask substrate surface

roughness effects on lithographic patterning", J. Vac. Sci. Technol. B, vol. 28, issue 6, 2010.

[43] E. Gullikson, C. Walton, and T. Taylor, "Proposed Specification of EUVL Mask Substrate Roughness", 2nd International Symposium on EUVL, 2003, https://e-reportsext.llnl.gov/pdf/243906.pdf

[44] M. Schøler, R. J. Blaikie, "Resonant surface roughness interactions in planar superlenses", Microelectron. Eng., vol. 87, issue 5-8, pp. 887–889, 2010.

[45] S. A. George, P. P. Naulleau, E. M. Gullikson, I. Mochi, F. Salmassi, K. A. Goldberg, E. H. Anderson, "Replicated mask surface roughness effects on EUV lithographic patterning and line edge roughness", Proc. SPIE, vol. 7969, pp. 79690E, 2011.

[46] A. Vaglio Pret, R. Gronheid, T. R. Younkin, M. J. Leeson, P. Y. Yan "Impact of EUV mask surface and absorber roughness on LWR", Proc SPIE, vol. 7969, pp. 79691T-7, 2011.

[47] J. W. Goodman, "Statistical optics", chap. 7, Wiley-Interscience 1985.

[48] J. W. Goodman, "Introduction to Fourier Optics", chap. 6, Roberts and Company Publishers 2004.

[49] O. Svelto, "Principles of Lasers", chap. 11, Springer, 2009.

[50] J. W. Goodman, "Speckle phenomena in Optics", chap. 1-3, 6, 8, Roberts and Company Publishers, 2010.

[51] K. Jain, C. G. Willson, B. J. Lin, "Fine-Line High-Speed Excimer Laser Lithography", Symposium on VLSI Technology, Digest of Technical Papers, pp. 92, 1982.

[52] G. M. Gallatin, N. Kita, T. Ujike, B. Partlo, "Residual speckle in a lithographic illumination system", JM3, vol. 8, issue 4, pp. 043003, 2009.

[53] O. Noordman, A. Tychkov, J. Baselmans, J. Tsacoyeanes, G. Politi, M. Patra, V. Blahnik, M. Maul, "Speckle in optical lithography and the influence on line width roughness," JM3, vol. 8, issue 4, pp. 043002, 2009.

[54] A. Vaglio Pret, R. Gronheid, T. R. Younkin, M. J. Leeson, P. Y. Yan, J. Engelen "Evidence of speckle in extreme UV lithography", Nature Photonics, submitted 2012.

[55] C. Rydberg, j. Bengtsson, t. Sandström, “Dynamic laser speckle as a detrimental phenomenon in optical projection lithography”, JM3, vol. 5, issue 3, 033004, 2006.

[56] N. A. Beaudry and T. D. Milster, “Effects of mask roughness and condenser scattering in EUVL systems,” in Emerging Lithographic Technologies III, Y. Vladimirsky, ed., Proc. SPIE 3676, pp. 653–662, 1999.

[57] T. Pistor and A. R. Neureuther, “Calculating aerial images from EUV masks,” in Emerging Lithographic Technologies III, Y. Vladimirsky, ed., Proc. SPIE 3676, pp. 679–696, 1999.

[58] P. P. Naulleau and G. M. Gallatin, “Line-edge roughness transfer function and its application to determining mask effects in EUV resist characterization,” Appl. Opt., vol. 42, issue 17, pp. 3390–3397, 2003.

[59] H. Tanabe, G. Yoshizawa, Y. Liu, V. L. Tolani, K. Kojima, N. Hayashi, “LER transfer from a mask to wafers,” Proc. SPIE, vol. 6607, pp. 66071H, 2007.

[60] A. Vaglio Pret, R. Gronheid, T. Graves, M. D. Smith, J. Biafore, “Mask absorber roughness impact in extreme ultraviolet lithography”, JM3, vol. 10, issue 2, pp. 023012, 2011.

[61] A. Vaglio Pret, R. Gronheid, “Mask line roughness contribution in EUV lithography,” Microelectron. Eng., vol. 88, issue 8, pp. 2167–2170, 2011.

[62] T. Kamo, H. Aoyama, Y. Arisawa, M. Kijima, T. Tanaka, O. Suga, “Impact of EUV mask absorber defect with pattern-roughness on lithographic images,” Proc. SPIE, vol. 7636, pp. 76360L, 2010.

[63] B. M. McClinton, P. P. Naulleau, T. Wallow, “Absorber height effects on SWA restrictions and ‘shadow’ LER”, Proc. of SPIE, vol. 7969, 796920, 2011.

[64] B. M. McClinton, P. P. Naulleau, “Mask roughness induced LER control and mitigation: aberrations sensitivity study and alternate illumination scheme”, Proc. SPIE 7969, 79691Z, 2011.

[65] Patrick P. Naulleau, “Correlation method for the measure of mask-induced line-edge roughness in extreme ultraviolet lithography”, Appl. Opt., vol. 48, no. 18, 2009.

[66] Patrick P. Naulleau, “Effect of mask-roughness on printed contact-size variation in extreme-ultraviolet lithography”, Appl. Opt., vol. 44, no. 2, 2005

[67] Chris A. Mack, “Impact of Mask Roughness on Wafer Line-Edge Roughness”, Proc. SPIE, vol. 7488, pp. 748828, 2009.

[68] G. M. Gallatin, Patrick P. Naulleau, “Modeling the transfer of line edge roughness from an EUV mask to the wafer”, Proc. SPIE, vol. 7969, pp. 796903, 2011.

[69] K. Garidis, A. Vaglio Pret, R. Gronheid, “Mask roughness impact on EUV and 193 nm immersion lithography”, Microelectron. Eng., in revision, 2012.

[70] P. P. Naulleau, G. M. Gallatin, “The effect of resist on the transfer of line-edge roughness spatial metrics from mask to wafer”, J. Vac. Sci. Technol. B, vol. 28, issue 6, pp. 1259, 2010.

[71] P. P. Naulleau, G. M. Gallatin, “Spatial scaling metrics of mask induced line-edge roughness,” J. Vacuum Sci. Technol. B: Microelectron. Nanometer Struct., vol. 26, issue 6, pp. 1903–1910, 2008.

[72] P. P. Naulleau, D. Niakoula, G. Zhang, “System-level line-edge roughness limits in extreme ultraviolet lithography”, J. Vac. Sci. Technol. B, vol. 26, issue 4, pp.1289, 2008.

[73] D. Kawamura, K. Kaneyama, S. Kobayashi, H. Oizumi, T. Itani, “Current benchmarking results of EUV resist at Selete”, Proc. SPIE, vol. 7140, pp. 714008-2 (2008)

[74] I. Pollentier, I. Neira, R. Gronheid, “Assessment of resist outgassing related EUV optics contamination for CAR and non-CAR material chemistries”, Proc. SPIE, vol. vol. 7972, pp. 797208 (2011)

[75] G. F. Lorusso, E. Hendrickx, N. Davydova, Y. Peng, M. Eurlings, K. Feenstra, and J. Jiang, “Metrology development for extreme ultraviolet lithography: Flare and out-of-band qualification”, J. Vac. Sci. Technol. B, vol. 29, issue 6, pp. 06F505 (2011)

[76] D. L. Goldfarb, R. L. Bruce, J. J. Bucchignano, D. P. Klaus, M. A. Guillorn, C. J. Wu, “Pattern collapse mitigation strategies for EUV lithography”, Proc. SPIE, vol. 8322, pp. 832205 (2012)

[77] R. Sakamoto, B. C. Ho, N. Fujitani, T. Endo, R. Ohnishi, “Development of under layer material for EUV lithography”, Proc SPIE, vol. 7969, pp. 79692F (2011).

[78] O. Montal, I. Dolev, M. Rosenzweig, K. Dotan, D. Meshulach, O. Adan, S. Levi, M. P. Cai, C. Bencher, C. S. Ngai, C. Jehoul, D. Van Den Heuvel, E. Hendrickx, “Characterization of EUV resists for defectivity at 32nm”, Proc. SPIE, vol. 7971, 79710G (2011)

[79] B. S. Kwon, J. S. Kim, N. E. Lee, S. K. Lee, S. W. Park, “Comparative Study on the Etching Characteristics of ArF and EUV Resists in Dual-frequency Superimposed Capacitively-coupled CF4/O2/Ar and CF4/CHF3/O2/Ar Plasmas”, JKPS, vol. 55, no. 4, pp. 1465 (2009)

[80] E. A. Sanchez, A. Vaglio Pret, R. Gronheid, W. Boullart, “Dry etching challenges for patterning smooth lines: LWR reduction of extreme ultraviolet photoresist”, Proc. SPIE, in publication (2012)

[81] X Jiang, P.J Scott, D.J Whitehouse and L Blunt “Paradigm shifts in surface metrology. Part II. The current shift”, Proc. R. Soc. A 463, 2071-2099 (2007).

[82] D. Whitehouse, Surface measurement (2003)

[83] Alain C. Diebold, Handbook of Silicon Semiconductor Metrology (2001)

[84] V. Constantoudis, G. P. Patsis, A. Tserepi, and E. Gogolides “Quantification of line-edge roughness of photoresists. II. Scaling and fractal analysis and the best roughness descriptors” J. Vac. Sci. Technol. B 1071, 1023O(2003)

[85] V. Constantoudis, G. P. Patsis, L. H. A. Leunissen, E. Gogolides “ Line edge roughness and critical dimension variation: Fractal characterization and comparison using model functions” J. Vac. Sci. Technol. B 22(4), 1071-1023 (2004)

[86] G. P. Patsis, V. Constantoudis, A. Tserepi, and E. Gogolides, G. Grozevb “Quantification of line-edge roughness of photoresists. I. A comparison between off-line and on-line analysis of top-down scanning electron microscopy images” J. Vac. Sci. Technol. B 21(3), 1071-1023 (2003)

[87] S.-B. Wang, W.-Y. Lee, Y. H. Chiu, H. J. Tao, Y. J. Mii “SEM Metrology Damage in Polysilicon Line and Its Impact on LWR Evaluation” Proc. of SPIE Vol. 7272 72720N, (2009).

[88] A. Yamaguchi, J. Yamamoto “Influence of image processing on line edge roughness in CDSEM measurement ” Proc. of SPIE Vol. 6922, 692221, (2008).

[89] Benjamin D. Bunday, Michael Bishop, and Donald McCormack “Determination of optimal Parameters for CD-SEM Measurement of Line Edge Roughness” – Proc. of SPIE Vol. 5375, 515-533 (2004)

[90] Bunday, B., Montgomery, C., Montgomery, W., Cordes, A. “Static and dynamic photoresist shrinkage effects in EUV photoresists” Proc. of SPIE Vol. 8324, 83241E (2012)

[91] J. S. Villarrubia “Issues in Line Edge and Line width Roughness Metrology” AIP Conf. Proc. 788, pp. 386-393(2005)

[92] R. Katz, C.D Chase, R. Kris, R. Peltinov, J.Villarrubia, and B. Bunday “ Bias reduction in roughness measurement through SEM noise removal” Proc. of SPIE Vol. 6152, 6154L, (2006)

[93] Atsuko Yamaguchi, Robert Steffen, Hiroki Kawada and Takashi Iizumi “Bias-Free Measurement of LER/LWR with Low Damage by CD-SEM” – Proc. of SPIE Vol. 6152, 61522D (2006)

[94] Patrick P. Naulleau, Christopher N. Anderson, Kim Dean, Paul Denham, Kenneth A. Goldberg, Brian Hoef, Bruno La Fontaine, and Tom Wallow “Recent results from the Berkeley 0.3-NA EUV microfield exposure tool” Proc. of SPIE Vol. 6517, 65170V, (2007)

[95] Vassilios Constantoudis, Evangelos Gogolides “Noise-free estimation of spatial Line Edge/Width Roughness parameters” Proc. of SPIE Vol. 7272, 72724B (2009)

[96] Atsushi Hiraiwa and Akio Nishida “Statistically accurate analysis of line width roughness based on discrete power spectrum” - Proc. of SPIE Vol. 7638, 76380N (2010).

[97] L. Azarnouche, E. Pargon, K. Menguelti, M. Fouchier, D. Fuard, P. Gouraud, C. Verove, O. Joubert, “Unbiased line width roughness measurements with critical dimension scanning electron microscopy and critical dimension atomic force microscopy” J. Appl. Phys. 111, 084318 (2012).

[98] Atsushi Hiraiwa and Akio Nishida “Scanning-electron-microscope image processing for accurate analysis of line-edge and line-width roughness” Proc. of SPIE Vol. 8324 83241D, (2012).

[99] Y. Martin and H. Kumar Wickramasinghe “Method for imaging sidewalls by atomic force microscopy” Appl. Phys. Lett. 64(19) (1994).

[100] N. G. Orji, T. V. Vorburger, J. Fu, R. G. Dixson, C. V. Nguyen, and J. Raja, “Line edge roughness metrology using atomic force microscopes” Measurement Science and Technology 16 (11) , pp. 2147-2154 (2005)

[101] J.Foucher, A.L. Fabre, P. Gautier “CD-AFM vs. CD-SEM for resist LER and LWR measurement” Proc. of SPIE Vol. 6152. 61520V,(2006)

[102] J. Foucher, A. Pikon, C. Andes, J. Thackeray “Impact of acid diffusion length on resist ler and lwr measured by CD-AFM and CD SEM” Proc. of SPIE Vol. 6518, 61181Q (2007)

[103] E. Pargon, M. Martin, J. Thiault, O. Joubert, J. Foucher, and T. Lill, “Linewidth roughness transfer measured by critical dimension atomic force microscopy during plasma patterning of polysilicon gate transistors” J. Vac. Sci. Technol. B 26 (3) , pp. 1011-1020 (2008)

[104] C. Nelson, S. C. Palmateer, A. R. Forte and T. M. Lyszczarz “Comparison of metrology methods for quantifying the line edge roughness of patterned features” J. Vac. Sci. Technol. B 17 2488-98 (1999)

[105] Reynolds, G.W., Taylor, J.W. “Correlation of atomic force microscopy sidewall roughness measurements with scanning electron microscopy line-edge roughness measurements on chemically amplified resists exposed by x-ray lithography” J. Vac. Sci. Technol. B 17 (6) , pp. 2723-2729

[106] N G Orji and R G Dixson “Higher order tip effects in traceable CD-AFM-based linewidth measurements” Meas. Sci. Technol. 18, 448–455, (2007)

[107] N. G. Orji, R. G. Dixson, B. D. Bunday and J. A. Allgair “Accuracy considerations for critical dimension semiconductor metrology” Proc. of SPIE Vol. 7042, 70420A, (2008).

[108] J. Foucher ; E. Pargon ; M. Martin ; S. Reyne ; C. Dupré “Paving the way for multiple applications for the 3D-AFM technique in the semiconductor industry” Proc. of SPIE Vol. 6922, 69220F, (2008)

[109] Gregory A. Dahlen, Lars Mininni, Marc Osborn, Hao-Chin Liu, Jason R.Osborne “TEM validation of CD AFM image reconstruction” Proc. of SPIE Vol. 6518, 651818, (2007)

[110] A-L.Foucher, J.Foucher, L.Dourthe “3D-AFM tip to tip variations and impact on measurement Performances” Proc. of SPIE Vol. 7638, 76381Z (2010)

[111] Ronald L. Jones; Wen-li Wu; Cheng-qing Wang; Eric K. Lin; Kwang-Woo Choi; Bryan J. Rice; George M. Thompson; Steven J. Weigand; Denis T. Keane “Characterization of line edge roughness using CD SAXS” Proc. of SPIE Vol. 6152, 61520N,(2006)

[112] Chengqing Wang ; Ronald L. Jones ; Eric K. Lin ; Wen-li Wu ; John S. Villarrubia ; Kwang-Woo Choi ; James S. Clarke ; Bryan J. Rice ; Michael J. Leeson ; Jeanette Roberts ; Robert Bristol ; Benjamin Bunday “Line edge roughness characterization of sub-50nm structures using CD-SAXS: Round-robin benchmark results” Proc. of SPIE Vol. 6518, 65181O, (2007)

[113] Chengqing Wang, Ronald L. Jones, Eric K. Lin, Wen-Li Wu, Bryan J. Rice, Kwang-Woo Choi, George Thompson, Steven J. Weigand, and Denis T. Keane “characterization of correlated line edge roughness of nanoscale line grating using small angle x-ray scattering” J. Appl. Phys. 102, 024901 (2007)

[114] Boaz Brill; Shahar Gov; Dani Hak; Valery Sorin; Tal Marcu; Benjamin Bunday “LER detection using dark field spectroscopic reflectometry” Proc. of SPIE Vol. 7638, 76380P (2010)

[115] Martin Foldyna, Thomas A. Germer, Brent C. Bergner “Mueller matrix ellipsometry of artificial non-periodic line edge roughness in presence of finite numerical aperture” Proc. of SPIE Vol. 7971, 79710N (2011).

[116] Deh-Ming Shyu ; Yi-Sha Ku and Nigel Smith "Angular scatterometry for line-width roughness measurement", Proc. of SPIE Vol. 6518, 65184G (2007)

[117] Frank Scholze; Akiko Kato; Jan Wernecke; Michael Krumrey “EUV and x-ray scattering methods for CD and roughness measurement” Proc. of SPIE Vol. 8166, 81661P, (2011)

[118] Thomas Schuster, Stephan Rafler, Karsten Frenner, Wolfgang Osten “Influence of line edge roughness (LER) on angular resolved and on spectroscopic scatterometry” Proc. of SPIE Vol. 7155, 71550W, (2008)

[119] Atsuko Yamaguchi and Osamu Komuro “Characterization of Line Edge Roughness in Resist Patterns by Using Fourier Analysis and Auto-Correlation Function” Proc. of SPIE Vol. 42, Issue 6B, pp. 3763 (2003)

[120] V. Constantoudis, G. P. Patsis, E. Gogolides “Photoresist line-edge roughness analysis using scaling concepts” Journal of Microlithography, Microfabrication and Microsystems 3 (3) , pp. 429-435 (2004)

[121] Bunday, B.D., Bishop, M., Villarrubia, J.S., Vladár, A.E. “CD-SEM Measurement of Line Edge Roughness Test Patterns for 193 nm Lithography” Proc. of SPIE Vol. 5041 , pp. 127-141 (2003)

[122] Leunissen, L.H.A., Lorusso, G.F., Ercken, M., Croon, J.A., Yang, H., Azordegan, A., DiBiase, T. “Full spectral analysis of line width roughness” Proc. of SPIE Vol. 5752 (I) , 49 , pp. 499-509 (2005)

[123] Leunissen, L.H.A., Gronheid, R., Gao, W. “Iso-sciatic point: Novel approach to distinguish 3-D mask effects from scanner aberrations in extreme ultraviolet lithography” Proc. of SPIE Vol. 6281, 628106 (2006)

[124] W. G. Lawrence, “Spatial frequency analysis of line edge roughness in nine chemically related photoresists” Proc. of SPIE Vol, 5039 II , pp. 713-724 (2004)

[125] Atsuko Yamaguchi and Osamu Komuro, “Characterization of line edge roughness in resist patterns by using Fourier analysis and auto-correlation function” Japanese Journal of Applied Physics, Volume 42, Issue 6B, pp. 3763 (2003).

[126] Gian F. Lorusso; Leonardus H. A. Leunissen; Monique Ercken; Christie Delvaux; Frieda Van Roey; Nadia Vandenbroeck; H. Yang; Amir R. Azordegan; Tony DiBiase “Spectral analysis of line width roughness and its application to immersion lithography” Journal of Micro/Nanolithography, MEMS, and MOEMS 05(03), 033003(2006).

[127] http://www.itrs.net/Links/2011ITRS/Home2011.htm

[128] K. Patel, T. Wallow, H. Levinson, C. Spanos “Comparative Study of Line Width Roughness (LWR) in Next-Generation Lithography (NGL) Processes” - Proc. SPIE Vol. 7640, 76400T (2010).

[129] C. A. Mack, “Fundamental principles of optical lithography”, chap. 8, J. Wiley & Sons, London (2007)

[130] Ban, Y., Ma, Y., Levinson, H., J., Kye, J. and Pan, D., Z., “Modeling and Characterization of Contact-Edge Roughness for Minimizing Design

and Manufacturing Variations in 32-nm Node Standard Cell," Proc. SPIE 7641, 76410D1- 76410D12 (2010).

[131] Eiji Morifuji, Hisashi Aikawa, Hisao Yoshimura, Akio Sakata, Masako Ohta, Masaaki Iwai, and Fumitomo Matsuko, "Layout Dependence Modeling for 45-nm CMOS With Stress-Enhanced Technique" IEEE Trans. On Electron Devices, 56(9): 1991-1998, (2009).

[132] Momonoi, Y., Osabe, T., Yamaguchi, A., McLellen Martin, E., Koyanagi, H., Colburn, M., E. and Torii, K., "CD-SEM metrology of spike detection on sub-40 nm contact hole," Proc. SPIE 7638, 76380Q1-76380Q11 (2010).

[133] A. Vaglio Pret, K. Garidis, R. Gronheid, J. Biafore "Stochastic Limitations for EUV

[134] Resist Kinetics towards the 16nm Node," 2011 International EUVL Symposium, Miami, FL, 2011.

[135] A. Habermas, O. Lu, D. Chase-Colin, M. Har-Zvi, A. Tam and O. Sagi, "Contact hole edge roughness: circles vs. stars," Proc. SPIE vol. 5375, 337-345, 2004.

[136] S. Babin, S. Borisov, G. Kwon, C. H. Lee, J. H. Oh, D. Y. Mun, and H. W. Yoo, "CD-SEM and E-beam Defect Inspection of High Aspect Ration Contact Holes: Measurement and Simulation of Pre-charge," Proc. SPIE vol. 8324, 8324281-8324281, 2012.

[137] M. T. Postek, R. D. Larrabee. And W. J. Keery "Speciman biasing to enhance or suppress secondary electron emission from charging specimens at low accelerating voltage. SCANNING 11, 111-121, 1989.

[138] F. Mizuno, S. Yamada, A. Miura, and H. Todokoro " Observation of deep holes using new technique" Proc. SPIE vol. 1926, 3471-356, 1993.

[139] K. M. Monahan, G. Toro-Lira, and M. P. Davidson "A new low-voltage SEM technology for imaging and metrology of submicrometer contact holes and other high-aspect-ration structures," Proc. SPIE vol. 1926. 33-346, 1993.

[140] V.-K Murugesan-Kuppuswamy, V. Constantoudis, E. Gogolides, Alessandro Vaglio Pretand R. Gronheid, "Contact edge roughness

metrology in nanostructures: Frequency in nanostructures: Frequency analysis and variations," Microelectron. Eng. 90, 126-130, 2012.

[141] V. –K. Murugesan-Kuppuswamy, V. Constantoudis and E. Gogolides, "Contact Edge Roughness: Characterization and modeling". Microelectron. Eng. 88, 2492 (2011).

[142] T. Y. Lee, D. Ihm, H. Cheon Kang, J. B. Lee, B. H. Lee, S. B. Chin, D. H. Cho, and C. Lyong Song. "Experimental study of contact edge roughness on sub- 100 nm various circular shapes," Proc. SPIE 5752, 516-526, 2011.

[143] T. Vandeweyer, M. Maenhoudt, J-F. de Marneffe, and P. Dirksen, " The measurement of Contact Edge Roughness in 193nm patterning," Proc. Interface, 2003.

[144] S. Jun, J. Kim, E. Jeong, Y. Yun, J. Kim, and K. Kim, "Optimization of Lithography Process to Improve Image Deformation of Contact Hole Sub-90 nm Technology Node," Proc. SPIE 6518,65183T1-65183T9, 2007.

[145] N. Otsu, "A threshold selection method from gray-level histogram," IEEE Trans. Sys., Man., Cyber. 9. 62-66. 1979.

[146] M. Sezgin and B. Sankur, " A survey over Image Thresholding Techniques and Quantitative Performance Evaluation," Journal of Electronic Imaging 13, 146-165 (2003).

[147] T. J. Deeming, "Fourier analysis with unequally spaced data," Astrophysics and Space Science 36, 137-158, 1975.

[148] R. A. Edelson and J. H. Krolik, "The discrete correlation function- a new method for analyzingunevenly sampled variability data, "The Asrophysical J., 333, 646-659, 1988.

[149] V. Constantoudis, E. Gogolides, G. P. Patsis, M. Wagner, J. DeYoung, C. Harbison. " Linewidth roughness analysis of EUV resist after development in homogenous CO2 solutions using CO2 compatiable salts (CCS) by three parameter model," Proc. SPIE 6153 II, 61533W, 2006.

[150] T. Wallow, D. Civay, S. Wang, H. Hoefnagels, C. Verspaget, G. Tanriseven, A. Fumar-Pici, S. Hansen, J. Schefske, M. Singh, R. Maas, Y. van Dommelen, J. Mallman, "EUV resist performance: current assessment for sub-22 nm half-pitch patterning on NXE:3300" Proc. SPIE 8322, 83221J (2012).

[151] K. Cho, H. Nakagawa, K. Maruyama, M. Shimizu, T. Kimura, Y. Hishiro, "Key Parameters of EUV Resists for Contact Hole Applications"Proc. SPIE 8322, 8322B (2012).

[152] K.Ban, J.Heo, H. Shim, M. Park, K. Lee, S. Koo, J. Kim, C. Bok, M. S. Kim, and H. Kang, "Comparison Study for 3x nm Contact Hole CD Uniformity between EUV Lithography and ArF Immersion Double Patterning" Proc. SPIE 8322, 8322A (2012).

[153] R. Gronheid, G. Winroth, A. Vaglio Pret, M. V. Dusa, T. R. Younkin, "Quantification of shot noise contributions to contact hole local CD non-uniformity" Proc. SPIE 8322, 8322M (2012).

[154] M. Higuchi, E. Gallagher, D. Ceperley, T. Brunnet, A. McGuire "Revisiting mask contact hole measurements" Proc. SPIE 6349, 634947 (2006).

[155] R. Gronheid, A. Vaglio Pret, B. Rathsack, J. Hooge, S. Scheer, K. Nafus, H. Shite, J. Kitano "Resolution–line width roughness–sensitivity performance tradeoffs for an extreme ultraviolet polymer bound photo-acid generator resist" J. Micro/Nanolith. MEMS MOEMS 10(1), 013017 (2011).

[156] C. N. Anderson, and P. P. Naulleau "Deprotection blur in extreme ultraviolet photoresists: Influence of base loading and post-exposure bake temperature" J. Vac. Sci. Technol. B 27, 665 (2009).

[157] Steenwinckel, D., Lammers, J., Koehler, T., Brainard, R. and Trefonas, P., "Resist effects at small pitches," J. Vac.Sci. Technol. B 24, 316-322 (2006).

[158] Dentinger, P., M., Hunter, L., L., O'Connell, D., J., Gunn, S., Goods, D., Fedynyshyn, T., H., Goodman, R., B. and Astolfi, D., K., "Photospeed considerations for extreme ultraviolet lithography resists," J. Vac. Sci. Technol. B 20, 2962-2967 (2002).

[159] Brainard, R., Trefonas, P., Lammers, J., Cutler, C., Mackevich, J., Trefonas, A. and Robertson, S., "Shot noise, LER and quantum efficiency of EUV photoresists," Proc. SPIE 5374, 74-86 (2004).

[160] Cutler, C.A., Mackevich, J.F., Li, J., O'Connell, D.J., Cardinale, G., Brainard, R.L., "Effect of polymer molecular weight on AFM polymer aggregate size and LER of EUV resists," Proc. SPIE 5037, 406-416 (2003).

[161] Gallatin, G.,M., "Resist blur and line edge roughness," Proc. SPIE 5754, 38-49 (2005).

[162] A. R. Pawloski and P. F. Nealey, “Effect of photoacid generator concentration on sensitivity, photoacid generation, and deprotection of chemically amplified resists” J Vac Sci Technol B 20, 2413 (2002).

[163] T. H. Fedynyshyn, D. K. Astolfi, A. Cabral, S. Cann, I. Pottebaum and J. M. Roberts, “PAG Segregation During Exposure Affecting Innate Material Roughness” Proc SPIe 7273, 727349 (2009)

[164] R. Gronheid, B. Rathsack, S. Bernard, A. Vaglio Pret, K. Nafus, and S. Hatakeyama,”Effect of PAG distribution on ArF and EUV resist performance” J. Photopol. Sci. Technol. 22, 97 (2008).

[165] Tsiartas, P.C., Flanagin, L.W., Henderson, C.L., Hinsberg, W.D., Sanchez, I.C., Bonnecaze, R.T., Willson, C.G. “The mechanism of phenolic polymer dissolution: A new perspective” Macromolecules 30 (16) , 4656-4664 (1997)

[166] Fukuda, H. “Analysis of line edge roughness using probability process model for chemically amplified resists” Japanese Journal of Applied Physics, Part 1, 42 (6 B) , 3748-3754 (2003)

[167] Cutler, C.A., Mackevich, J.F., Li, J., O'Connell, D.J., Cardinale, G., Brainard, R.L. “Effect of polymer molecular weight on AFM polymer aggregate size and LER of EUV resists” Proc. of SPIE Vol. 5037 I , 406-417 (2003)

[168] Brainard, R.L., Trefonas, P., Lammers, J.H., Cutler, C.A., Mackevich, J.F., Trefonas, A., Robertson, S.A. “ Shot noise, LER and quantum efficiency of EUV photoresists” Proc. of SPIE Vol. 5374, 74-85 (2004)

[169] Schmid, G.M., Burns, S.D., Stewart, M.D., Willson, C.G. “Mesoscale simulation of positive tone chemically amplified photoresists” Proc. of SPIE Vol. 4690 I , 381-390 (2002)

[170] Mack, C.A. “Stochastic modeling in lithography: Use of dynamical scaling in photoresist development” Journal of Micro/ Nanolithography, MEMS, and MOEMS 8 (3), 033001 (2009)

[171] Mack, C.A. “Stochastic modeling of photoresist development in 2D and 3D” Proc. of SPIE Vol. 7639, 76392L (2010)

[172] Mack, C.A., Biafore, J.J., Smith, M.D. “Stochastic acid-base quenching in chemically amplified photoresists: A simulation study” Proc. of SPIE Vol. 7972, 79720V (2011)

[173] Lawson, R.A., Henderson, C.L. “Mesoscale kinetic monte carlo simulations of molecular resists: The effect on PAG homogeneity on resolution, LER, and sensitivity” Proc. of SPIE Vol. 7273, 727341 (2009)

[174] Lawson, R.A., Henderson, C.L. “ Understanding the relationship between true and measured resist feature critical dimension and line edge roughness using a detailed scanning electron microscopy simulator” Journal of Vacuum Science and Technology B: Microelectronics and Nanometer Structures 28 (6) , C6H34-C6H39 (2010)

[175] Saeki, A., Kozawa, T., Tagawa, S., Cao, H.B. “Correlation between proton dynamics and line edge roughness in chemically amplified resist for post-optical lithography” Journal of Vacuum Science and Technology B: Microelectronics and Nanometer Structures 24 (6) , 3066-3072 (2006)

[176] Saeki, A., Kozawa, T., Tagawa, S., Cao, H.B., Deng, H., Leeson, M.J. “Exposure dose dependence on line edge roughness of a latent image in electron beam/extreme ultraviolet lithographies studied by Monte Carlo technique” Journal of Micro/ Nanolithography, MEMS, and MOEMS 6 (4), 043004 (2007)

[177] Saeki, A., Kozawa, T., Tagawa, S. “Origin of frequency-dependent line edge roughness: Monte Carlo and fast Fourier-transform studies” Applied Physics Letters 95 (10), 103106 (2009)

[178] Hiroshi Morita, Masao Doib “Meso-scale simulation of the polymer dynamics in the formation process of line-edge roughness” Proc. of SPIE Vol. 7273, 727337 (2009)

[179] Hiroshi Morita, Masao Doib “Meso-scale simulation of the line-edge structure based on polymer chains in the developing and rinse process” Proc. of SPIE Vol. 7639, 763932 (2010)

[180] Hiroshi Morita “Meso-scale simulation of the line-edge structure based on resist polymer molecules by negative-tone process” Proc. of SPIE Vol. 7972, 79720W (2011)

[181] John J. Biafore, Mark D. Smith, Chris A. Mack, James W. Thackeray, Roel Gronheid, Stewart A. Robertson, Trey Graves, David Blankenship “Statistical simulation of resist at EUV and ArF” Proc. of SPIE Vol. 7273, 727343 (2009)

[182] John J. Biafore, Mark D. Smith, Eelco van Setten, Tom Wallow, Patrick Naulleau, David Blankenship, Stewart A. Robertson, Yunfei Deng “Resist pattern prediction at EUV” Proc. of SPIE Vol. 7636, 76360R (2010)

[183] Mark D. Smith, Trey Graves, John Biafore, Stewart Robertson, Cheolkyun Kim, James Moon, Jaeheon Kim, Cheolkyu Bok, Donggyu Yim “Comprehensive EUV Lithography Model” Proc. of SPIE Vol. 7969, 796906 (2011)

[184] Schnattinger, T., Bär, E., Erdmann, A. “Three-dimensional resist development simulation with discrete models” Journal of Vacuum Science and Technology B: Microelectronics and Nanometer Structures 24 (6) , 3040-3043 (2006)

[185] Thomas Schnattinger and Andreas Erdmann “A comprehensive resist model for the prediction of line-edge roughness material and process dependencies in optical lithography” Proc. of SPIE Vol. 6923, 69230R, (2008)

[186] Patsis, G.P., Gogolides, E. “Simulation of surface and line-edge roughness formation in resists” Microelectronic Engineering 57-58 , 563-569 (2001)

[187] Patsis, G.P., Constantoudis, V., Gogolides, E. “Material origins of line-edge roughness: Monte-Carlo simulations and scaling analysis” Proceedings of SPIE - The International Society for Optical Engineering 5376 (PART 2) , pp. 773-781, (2004).

[188] Patsis, G.P., Drygiannakis, D., Constantoudis, V., Raptis, I., Gogolides, E. “Stochastic modeling and simulation of photoresist surface and line-edge roughness evolution” European Polymer Journal 46 (10) , 1988-1999 (2010)

[189] Patsis, G.P., Gogolides, E., Van Werden, K. “Effects of photoresist polymer molecular weight and acid-diffusion on line-edge roughness” Japanese Journal of Applied Physics, Part 1: Regular Papers and Short Notes and Review Papers 44 (8) , 6341-6348 (2005)

[190] Patsis, G.P., Gogolides, E. “Material and process effects on line-edge-roughness of photoresists probed with a fast stochastic lithography simulator” Journal of Vacuum Science and Technology B: Microelectronics and Nanometer Structures 23 (4) , 1371-1375 (2005)

[191] Patsis, G.P., Gogolides, E. “Effects of model polymer chain architectures and molecular weight of conventional and chemically

amplified photoresists on line-edge roughness. Stochastic simulations" Microelectronic Engineering 83 (4-9) , 1078-1081 (2006)

[192] Drygiannakis, D., Patsis, G.P., Raptis, I., Niakoula, D., Vidali, V., Couladouros, E., Argitis, P., Gogolides, E. "Stochastic simulation studies of molecular resists" Microelectronic Engineering 84 (5-8) , pp. 1062-1065 (2007)

[193] Constantoudis, V., Kokkoris, G., Xydi, P., Gogolides, E., Pargon, E., Martin, M. "Line-edge-roughness transfer during plasma etching: Modeling approaches and comparison with experimental results" Journal of Micro/ Nanolithography, MEMS, and MOEMS 8 (4), 043004 (2009)

[194] Philippou, A., Mülders, T., Schöll, E. "Impact of photoresist composition and polymer chain length on line edge roughness probed with a stochastic simulator" Journal of Micro/ Nanolithography, MEMS, and MOEMS 6 (4), 043005 (2007)

[195] Flanagin, L. W., Singh, V. K., and Willson, C. G., "Molecular model of phenolic polymer dissolution in photolithography" J. Polym. Sci., Part B: Polym. Phys. 37, 2103 (1999).

[196] G. M. Gallatin, F. A. Houle and J. L. Cobb., "Statistical limitations of Printing 50 and 80 nm contact holes by EUV lithography" J. Vac. Sci. Technol. B 21(6), (2003).

[197] J. Cobb, F. Houle, and G. Gallatin., "The estimated impact of shot noise in extreme ultraviolet lithography" Proc. of SPIE Vol. 5057 (2003).